R

Radiotracer Methods

György Inzelt
Department of Physical Chemistry, Eötvös Loránd University, Budapest, Hungary

Introduction

The application of radiotracer methods in electrochemistry dates back to the pioneering works by György Hevesy in 1914. The aim of these studies was to demonstrate that isotopic elements can replace each other in both electrodeposition and equilibrium processes (Nernst law). Nevertheless, Joliot's fundamental work in 1930 is considered by electrochemists as a landmark in the application of radiochemical (nuclear) methods in electrochemistry.

Radiochemical methods, such as tracer methods [1–3], Mössbauer spectroscopy [4], neutron activation [5], thin layer activation (TLA) [5], ultrathin layer activation (UTLA) [5], and positron lifetime spectroscopy [6], are applied for the study of a wide range of electrochemical surface processes. The most important areas are as follows: adsorption and electrosorption occurring on the surface of electrodes; the role of electrosorption in electrocatalysis; deposition and dissolution of metals; corrosion processes; the formation of surface layers, films on electrodes (e.g., polymer films), and investigation of migration processes in these films; study of the dynamics of electrosorption and electrode processes under steady-state and equilibrium conditions (exchange and mobility of surface species); and electroanalytical methods (e.g., radiopolarography).

Application of Radiotracers in Electrochemistry

The main advantages of using radiotracers are as follows:

- The radiation emitted by radiotracers is generally easy to detect and measure with high precision.
- The radiation emitted is independent of pressure, temperature, and chemical and physical state.
- Radiotracers do not affect the system and can be used in nondestructive techniques.
- The radiation intensities measured furnish direct information concerning the amount of the labeled species, and no special models are required to draw quantitative conclusions.

Metal Dissolution

In the case of metal dissolution studies the principle of the methods used is based on the labeling of a component of the metal phase by one of its radioactive isotopes and calculating the dissolution rate of the metal specimen by measuring either the increase in radiation coming from the solution phase or the decrease in radiation coming from the solid phase.

G. Kreysa et al. (eds.), *Encyclopedia of Applied Electrochemistry*, DOI 10.1007/978-1-4419-6996-5,

The main steps here are as follows:

- Introduction of the radioisotope into the specimen. The task can be achieved at least by three methods: (a) through melting, (b) by electrolytic deposition of the radioactive metal, and (c) by subjecting the metal specimen to neutron irradiation in a nuclear reactor.
- Measurement of the changes in radiation intensity caused by the dissolution process.
- A variation is the application of backscattering for the study of the electrochemical formation and dissolution of thin metal layers.

Electrosorption

Various methods have been developed for in situ radiotracer adsorption studies depending on the requirements of the problems to be studied. In case of in situ studies, the central problem is how to separate the signal (radiation) to be measured from the background radiation and how to attain the optimal ratio of these quantities.

From this point of view methods can be divided into two main groups:

- Radiation of the solution background is governed and minimized by self-absorption of the radiation, i.e., by the attenuation of the radiation intensity by the radioactive medium itself (thin-foil method).
- Background radiation intensity is minimized by mechanical means (thin-gap method, electrode lowering technique).

As to the role of the labeled species in the radiotracer study of adsorption phenomena, two different versions of the method may be distinguished. In the first, the direct method, the species to be studied is labeled and the radiation measured gives direct information on the adsorption of this species. However, this method cannot be used in several cases owing to technical restrictions related to the very nature of the radiotracer method (the available concentration range is limited; no distinction can be made between the adsorption of the labeled compound studied and that of a product formed from it; the number of commercially available labeled compounds is restricted).

In the case of indirect radiotracer methods, instead of labeling the species to be studied another adequately chosen labeled species (the indicator species) is added to the system, and the adsorption of this component is followed by the usual radiotracer measuring technique. The adsorption of the indicator species should be related to that of the species studied. The nature of this link could be different in different systems.

Radiotracer technique offers a unique possibility of demonstrating the occurrence of specific adsorption of an ion by labeling it and studying its adsorption in the presence of a great excess of other ions, electrolytes (supporting electrolyte). For these studies at least a difference of one to two orders of magnitude in concentrations should be considered. Under such conditions with nonspecific adsorption, determined by coulombic interactions, no significant adsorption of the labeled species, present in low concentration, could be observed. In contrast to this, the observation of a measurable adsorption can be considered as a proof of the occurrence of the specific adsorption. Using isotopes emitting soft β^--radiation, (e.g., ^{14}C, ^{35}S, ^{36}Cl), the self-absorption of the radiation in the solution phase is so high that the thickness of the solution layer effective in the measured solution background radiation is very low. In this case the surface concentration, Γ, can be easily calculated from the radiation intensity measured (I_T):

$$\Gamma = \frac{I_a}{I_s} \cdot \frac{c}{\mu\rho\gamma} = \frac{I_T - I_s}{I_s} \frac{c}{\mu\rho\gamma} = \left(\frac{I_T}{I_s} - 1\right) \frac{c}{\mu\rho\gamma} \quad (1)$$

where I_s and I_a are the intensities of the radiation coming from the solution phase and from the adsorbed layer, respectively, c is the concentration of the labeled species present in the solution phase, μ is the mass absorption coefficient of the radiation, γ is the roughness factor of the electrode, and ρ is the density of the solution (Fig. 1).

Various versions of tracer methods were applied for studies of electrodes with polycrystalline smooth or rough surfaces and well-defined surfaces [3].

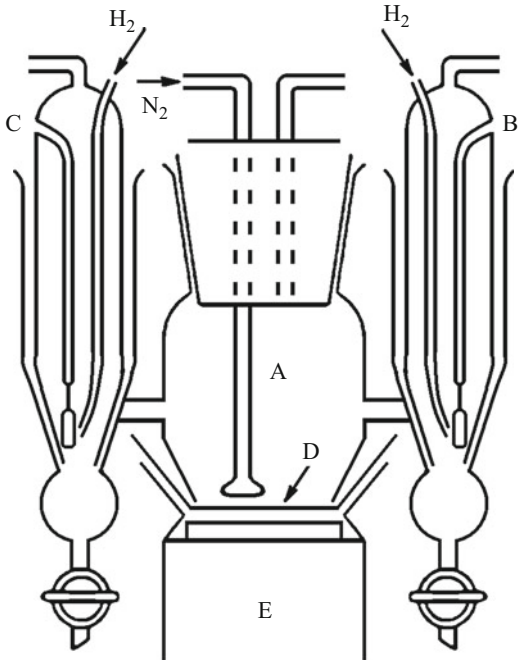

Radiotracer Methods, Fig. 1 Three-electrode cell used for the radiotracer studies. (*A*) Is the main compartment that contains the electrolyte and the labeled compound (ions). (*B* and *C*) Are the compartments of the reference and counter electrodes, respectively. (*D*) Is the working electrode, usually a gold-covered plastic foil (on the gold other metals and/or films can be deposited in advance). (*E*) Is the scintillation detector

Future Directions

It is a well-established in situ technique in electrochemistry. As described the novel radiochemical methods are continuously built in its arsenal widening the opportunities of the application of radiotracer methods.

References

1. Horányi G (1999) Radiotracer studies of adsorption/sorption phenomena at electrode surfaces. In: Wieckowski A (ed) Interfacial electrochemistry, theory, experiment, and applications. Marcel Dekker, New York, pp 477–491
2. Horányi G (ed) (2004) Radiotracer studies of interfaces. In: Interface science and technology, vol 3. Elsevier, Amsterdam
3. Krauskopf EK, Chan K, Wieckowski A (1987) In situ radiochemical characterization of adsorbates at smooth electrode surfaces. J Phys Chem 91:2327–2332
4. Kálmán E, Lakatos M, Kármán FH, Nagy F, Klencsár Z, Vértes A (2005) Mössbauer spectroscopy for characterization of corrosion products and electrochemically formed layers. In: Freund HE, Zewi I (eds) Corrosion reviews. Freund Publishing House, Tel Aviv, pp 1–106
5. Horányi G, Kálmán E (2005) Recent developments in the application of radiotracer methods in corrosion studies. In: Marcus PH, Mansfeld F (eds) Analytical methods in corrosion science and engineering. CRC, Boca Raton, pp 283–333
6. Süvegh K, Horányi TS, Vértes A (1988) Characterization of the β-Ni(OH)2/β-NiOOH system by positron lifetime spectroscopy. Electrochim Acta 33:1061–1066

Raman Spectroelectrochemistry

Salma Bilal
National Centre of Excellence in Physical Chemistry, University of Peshawar, Peshawar, Pakistan

Introduction

Raman Spectroscopy

Raman spectroscopy (named after C. V. Raman) is a spectroscopic technique used to study vibrational, rotational, and other low-frequency modes in a system. Generally Raman spectroscopy relies on inelastic or Raman scattering of monochromatic light, usually from a laser in the visible, near-infrared, or near ultraviolet range. The Raman effect occurs when light impinges upon a molecule and interacts with the electron cloud of the bonds of that molecule. Typically, a sample is illuminated with a laser beam. Scattered light from the illuminated spot is collected with a lens and sent through a monochromator. The laser light interacts with phonons or other excitations in the system, resulting in the energy of the laser photons being shifted up or down. The shift in energy gives information about the phonon modes in the system.

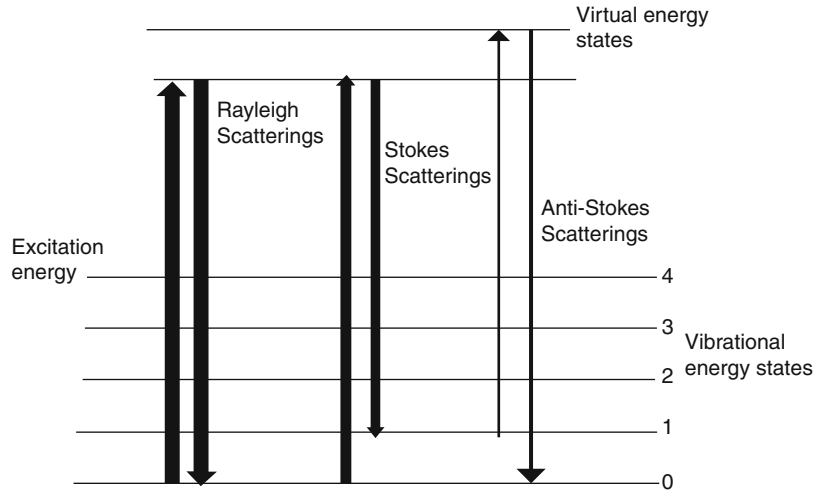

Raman Spectroelectrochemistry, Fig. 1 Schematic diagram of Raman scattering

For a molecule it is necessary that the molecular vibration or rotation must cause a change in a component of molecular polarizability in order to be Raman active. During the experiment radiation scattered by the sample is detected. Wavelengths close to the laser line (due to elastic Rayleigh scattering) are filtered out, and those in a certain spectral window away from the laser line are dispersed onto a CCD detector. The Raman scattering depends upon the polarizability (the amount of deformation of electron cloud) of the molecules. The amount of the polarizability and its change of the bond will determine the intensity and frequency of the Raman shift. The photon excites one of the electrons into a virtual state. For a molecule it is necessary that the molecular vibration or rotation must cause a change in a component of molecular polarizability. During the experiment radiation scattered by the sample is detected. When the photon is released the molecule relaxes back into a vibrational energy state. The molecule will typically relax into the first vibrational energy state and this generates Stokes Raman scattering. If the molecule is excited from an elevated vibrational energy state, it may relax into the vibrational ground energy state and the Raman scattering is then called anti-Stokes Raman scattering. Since most molecules are in their vibrational ground state at ambient temperature, the intensities of Stokes lines are higher than those of the anti-Stokes lines. This is the reason why only the Stokes lines are recorded as the Raman spectrum (Fig. 1).

The development of modern Raman spectrometers has led to a more efficient registration of weak Raman signals. Spectra that in the old equipments took several hours to register can often be recorded within few minutes, using a modern spectrometer. In the early spectrometers, the separation of Rayleigh and Raman scattering was accomplished by double or triple monochromators, but after this complex process with many components, only a small amount reaches the detector. The development of efficient notch filters allows simple separation of Raman and Rayleigh light and usually more than 30 % of the scattered light can be detected. Since the scattered light is detected more efficiently, low-power lasers (about 20 mW) can be used. The advantages are that these lasers are relatively cheap, do not require external cooling, and are less likely to burn the sample. The wide range of accessible wavelengths (100–4,000 cm^{-1}), the possible resolution (1 cm^{-1}or better), fast response of the detection setup, and the lack of interference by water (the most commonly employed electrolyte in electrochemistry) because of its weak Raman scattering have further added plus points to this development.

Raman Spectroelectrochemistry

Raman spectroscopy can be coupled with an electrochemical setup, since vibrational information is very specific for the chemical bonds in molecules and between molecules and electrode surfaces.

This technique can also be used for the study of more complex systems such as complicated carbon nanostructures or electrodes modified with a film of an intrinsically conducting polymer. The dependence of the observed features (in the Raman spectra of polyconjugated molecules) on the excitation line wavelength is an intrinsic property of these macromolecular systems [1]. This phenomenon significantly complicates vibrational investigations of conducting polymers based on Raman spectroscopy. Raman analysis of conducting polymers requires the registration of the spectra not only for different oxidation states of the polymer but also using different excitation wavelengths. Figure 2a shows development of Raman spectra during charging of a polyaniline (PANI) film in 0.5 **M** H_2SO_4, deposited on a gold disk electrode. Sample was illuminated with 514.5 Ar^+-ion laser Coherent Innova 70. When recorded at different applied potentials, the Raman spectra of the conducting polymer film provide useful information about the changes occurring in the polymer structure upon oxidation or reduction. At lower potential the spectra show only two bands, but as the potential increases the intensity of the bands increases and new bands appear showing the change in the structure of polymer with changing potential up to $E_{SCE} = 0.2$ V and then decreases with further potential increase. Normally the intensity of a particular band increases with increasing potential if it is related to the redox process of the polymer. At potentials more positive than the formal redox potential, these bands show a decreasing trend, while bands corresponding to the reduced form of the polymeric material show a decreasing trend with increasing potential. The appearance of strong bands around 1,620 cm^{-1} at lower potentials corresponds to the benzenoid structure in the polymer. Appearance of the strong band at 1,169 cm^{-1} and around 1,510 and 1,579 cm^{-1} is caused by modes of the quinoid structure, characteristics of the oxidized form of the polymer. With red excitation line ($l_0 = 647.1$ nm, Fig. 2b) the spectra show features different from the one in Fig. 2. Numerous bands that were not observed in Fig. 2 can clearly be seen here. Hence, the combination of recording Raman spectra at different excitation wavelengths can provide useful information about the changes in the structure of the sample upon changing the potential.

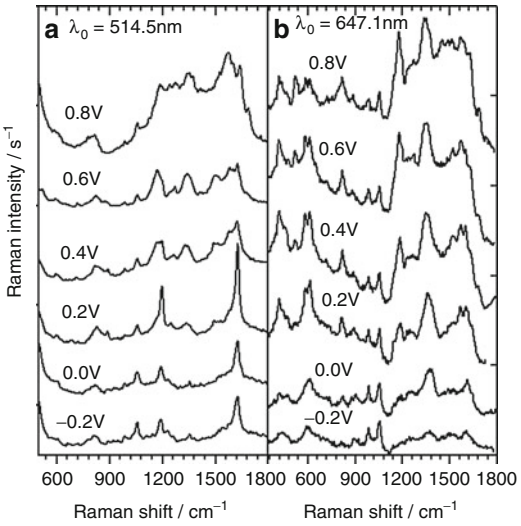

Raman Spectroelectrochemistry, Fig. 2 In situ Raman spectra of polyaniline in 0.5 **M** H_2SO_4 at different electrode potentials and different excitation wavelengths, as indicated

Surface-Enhanced Raman Spectroscopy (SERS)

A great disadvantage in any application of Raman spectroscopy is the extremely small cross-section of Raman scattering, between 10^{-13} and 10^{-26} cm^2/molecule. The larger value is obtained under resonance Raman conditions. With the discovery of a particular enhancement effect (upto 10^6) by Fleischmann et al. [2], that affects only species in close contact with the metal electrode surface and slightly later by Jeanmaire et al. [3] demonstrated surprisingly the feasibility of vibrational studies of electrochemical interfaces with Raman spectroscopy

(for an overview, see [4]). Because of the large enhancement, small sample volumes can be used and current detections are in picomole to femtomole range [5]. Surface-enhanced Raman spectra can only be obtained if the molecules to be investigated are adsorbed to the so-called SERS-active substrate. The most common SERS-active substrates are coinage metals (i.e., copper, silver, and gold), island films consisting of small metal particles deposited on glass surface, cold-deposited films, lithographically produced metal spheroids, etc. [6].

If the laser excitation wavelength matches with the one of the band maxima in the UV–vis spectra of the sample, the intensity of the scattered light is strongly increased. This is called "resonance enhancement" [7]. The problem with low sensitivity of Raman signals can be overcome when surface-enhanced resonance Raman (SERRS) is used. An enhancement factor of about 10^{10} and 10^{11} has been claimed for a dye molecule in SERRS experiments. In SERRS it is generally agreed that different effects must contribute to the enhancement of the Raman signals.

Preparation of the electrode is a main step in electrochemical SERS studies. In general, the surface of the electrode is roughened to provide the desired enhancement and an artificially increased surface area. As a common practice, roughening of the electrode is done by applying oxidation–reduction electrode potential cycling in a suitable electrolyte solution. Chloride-containing electrolyte solutions have frequently been used for coinage metals. Although chloride strongly adsorbs on these surfaces, however, studies have shown that the adsorbed chlorides can be washed off completely, leaving no spectroscopic evidence in the subsequently recorded spectra. Surface roughening can also be done by keeping the electrode potential at the upper limit for some time. Further information on electrochemical surface treatment procedure can be found elsewhere [8]. The enhancement mechanisms can be divided into electromagnetic field enhancement and chemical enhancement. In the former mechanism the electromagnetic field of the light at the surface is enhanced under conditions of surface plasmon resonance. If the surface plasmons are in resonance with the incident light, then both the resonance laser light and scattered Raman light are amplified through their interaction with the surface. Coinage metals are dominant as SERRS substrate as the resonance condition is satisfied at the visible frequencies, commonly used for Raman spectroscopy. The chemical enhancement mechanism is related to specific interactions, i.e., electronic coupling between metal and molecule. The interaction results in an increased cross-section of the Raman signal of the adsorbed molecule in SERRS experiment, compared to the cross-section of the free molecule in a normal Raman measurement. The chemical enhancement mechanism is restricted to molecules in the first layer of metal, since electronic transitions are only possible when the metal and molecules are in close contact [9, 10]. It has been known since early SERS observations that the relative intensities of SERS bands are different from those of free molecules in solution, and it has been speculated that this may be connected with the effect of orientation of the adsorbed molecule on the surface [11]. The electromagnetic enhancement theory explains the dependence of the Raman signal intensity on molecular orientation by describing how the electric field at the surface of metal particles couples with the polarizability tensors [12]. The greatest surface enhancement is observed for vibration that involves changes in the molecular polarizability perpendicular to the metal surface. Comparison of the relative band intensities in SERS and normal Raman spectra allow the average orientation and distance from the surface of the adsorbate functional groups to be determined [13]. Some other terminologies related to SERS are as follows:

- Surface-Unenhanced Raman Spectroscopy (SUERS)
- This terminology is used when non-coinage metals like platinum, illuminating wavelengths that are known not to support surface enhancement (i.e., 514.5 nm for gold electrode) or smooth surfaces, are used.

- Deenhanced Surface Raman Spectroscopy (DESERS)
- Spectroscopy performed with surfaces where enhancement has been quenched by deposition/adsorption of foreign metals atoms has been designated as deenhanced SERS (DESERS), and for a complete overview and further details see [14–16].

Applications of Raman Spectroelectrochemistry

Raman spectroelectrochemistry is the method of choice to analyze the structure of all kinds of materials, e.g.:

1. Carbon materials like graphite, graphene, carbon nanotubes, and fullerenes.
2. Information about crystalline or amorphous structure and crystallite size can be obtained from shift and shape of vibration modes.
3. Useful information can be obtained about the changes occurring in the structure of the sample material upon charging.
4. The state and quality of nanostructured materials for battery research as well as lithium content can be concluded by their characteristic vibration modes.
5. Worthy information can be obtained for the orientation of molecules on the surface of electrode in case of self-assembled monolayers (SERS).

References

1. Louarn G, Lapkowski M, Quillard S, Pron A, Buisson PJ, Lefrant S (1996) Vibrational properties of polyaniline-isotope effect. J Phys Chem 100:6998
2. Fleischmann M, Hendra PJ, McQuillan AJ (1974) Raman spectra of pyridine adsorbed at a silver electrode. Chem Phys Lett 26:163
3. Jeanmair DL, van Duyne RP (1977) Surface Raman spectroelectrochemistry: part I. Heterocyclic, aromatic, and aliphatic amines adsorbed on the anodized silver electrode. J Electroanal Chem 84:1
4. Haynes CL, MacFarland AD, van RP D (2005) Surface-enhanced Raman spectroscopy. Anal Chem 77:338A
5. Kneipp K, Kneipp H, Itzkan I, Dasari RR, Feld MS, Zander C, Enderlein J, Keller RA (2002) Single molecule detection in solution: methods and applications. Wiley-VCH Verlag, Berlin
6. Moskovits M (1985) Surface-enhanced spectroscopy. Rev Mod Phys 57:783
7. Sathayanarayana DN (2004) Theory and application. In: Vibrational spectroscopy. New Age International, New Delhi
8. Holze R (1994) Spectroscopic methods in electrochemistry: new tools for old problems. Bull Electrochem 10:45
9. Campion A, Kambhampati P (1998) Surface-enhanced Raman scattering. Chem Soc Rev 27:241
10. Ruperez A, Laserrna JJ (1996) Modern techniques in Raman spectroscopy. Wiley, Chichester
11. Creighton JA (1983) Surface raman electromagnetic enhancement factors for molecules at the surface of small isolated metal spheres: the determination of adsorbate orientation from sers relative intensities. Surf Sci 124:209
12. Grabbe ES, Buck RP (1989) Surface-enhanced Raman spectroscopic investigation of human immunoglobulin G adsorbed on a silver electrode. J Am Chem Soc 111:8362
13. Herne TM, Ahern AM, Garell RL (1991) Surface-enhanced Raman spectroscopy of tripeptides adsorbed on colloidal silver. Anal Chim Acta 246:75
14. Holze R (2009) Surface and interface analysis: an electrochemists tool box. Springer, Berlin/Heidelberg
15. Mayer P, Holze R (2003) Pyridine as a probe molecule for surface enhanced Raman spectroscopy of the silver-modified glassy carbon/solution interface. Surf Sci 522:55
16. Kania S, Holze R (1998) Surface enhanced Raman spectroscopy of anions adsorbed on foreign metal modified gold electrodes. Surf Sci 408:252

Rare Earth Metal Production by Molten Salt Electrolysis

Hongmin Zhu
School of Metallurgical and Ecological Engineering, University of Science and Technology Beijing, Beijing, China

Introduction

Rare earth metals (REM) include 15 lanthanides elements (Ln) from atomic number 57–71 located in the IIIB group of the periodic table and scandium (Sc) and yttrium (Y) elements, as listed in Table 1. The most common oxidation state for the rare earth metal elements is RE^{3+}, but some other

Rare Earth Metal Production by Molten Salt Electrolysis, Table 1 Classification of the rare earth metals

Element	Symbol	Atomic number	Melting point/°C	Valence
Scandium	Sc	21	1,539	3
Yttrium	Y	39	1,509	3
Lanthanum	La	57	920	3
Cerium	Ce	58	795	3,4
Praseodymium	Pr	59	935	3,4
Neodymium	Nd	60	1,024	3
Promethium	Pm	61		3
Samarium	Sm	62	1,072	2,3
Europium	Eu	63	826	2,3
Gadolinium	Gd	64	1,312	3
Terbium	Tb	65	1,356	3,4
Dysprosium	Dy	66	1,407	3
Holmium	Ho	67	1,470	
Erbium	Er	68	1,522	
Thulium	Tm	69	1,545	
Ytterbium	Yb	70	824	
Lutetium	Lu	71	1,656	

oxidation states, RE^{2+} and RE^{4+}, are occasionally found. For example, cerium (Ce), and to a much lesser extent Pr and Tb, can form RE^{4+} ions, and Sm, Eu, and to a lesser extent Yb can form RE^{2+} ions. These deviations from "normal" behavior (formation of only RE^{3+}) are sometimes attributed to the special stability of empty, half-filled, or filled shells: $Ce^{4+}(4f^0)$, $Eu^{2+}(4f^7)$, $Yb^{2+}(4f^{14})$, but $Pr^{4+}(4f^1)$ and Sm^{2+} $(4f^6)$ do not fully satisfy this criterion.

The high activity of REM makes it impossible to be obtained from an aqueous solution; therefore, currently most of the REM have been produced by molten salt electrolysis and some by thermal reduction method due to the existence of multivalent ions in the molten salts as shown in Table 1. Compared to the thermal reduction method, molten salt electrolysis is a relatively economical one because the process is continuous and easy to control. And it has been widely used in the industry to produce a single rare earth metal such as La, Ce, Pr, Nd and mixed rare earth metal alloys.

Usually two types of electrolyte systems in the industry have been applied, one is chloride system composing of $RECl_3$–KCI and another is fluoride–oxide system of RE_2O_3–REF_3–LiF [1]. Currently, in the USA, Japan, and Kazakhstan, fluoride–oxide system is employed to produce the mixed rare earth metals with a 20–25 kA capacity. While Germany applies chloride system to produce rare earth metals and the current capacity reaches 50 kA. Before 1997 most of the rare earth metals in China were produced from chloride system, only a small amount of rare earth metals from fluoride–oxide system. Since 2000, China has completely employed fluoride–oxide system to produce rare earth metals. Usually, the current efficiency is dependent on the electrolyte system, and less than 50 % for chloride system and less than 87 % for fluoride–oxide system are shown in Table 2. This is caused by the multiple oxidation states of the rare earth metal elements in the molten salts.

The most common raw materials for the REM molten salt electrolysis are in the RE^{3+} state, such as RE_2O_3, $RECl_3$. But RE^{2+} still exists to a certain extent in the molten salts, especially in the chloride melts, some rare earth metal elements have presented a higher level of divalent oxidation states, such as neodymium, samarium, europium, dysprosium, thulium, and ytterbium, which result in a lower current efficiency. For Sm and Eu molten salt electrolysis processes, even no metals can be obtained at the cathodes due to a cyclic transformation of $Sm^{2+}/Sm^{3+}(Eu^{2+}/Eu^{3+})$ and $Sm^{3+}/Sm^{2+}(Eu^{3+}/Eu^{2+})$ on the electrodes during electrolysis. And some of the rare earth metal elements show tetravalent oxidation states at the chlorine pressure far in excess of atmospheric pressure, such as Ce^{4+}. Most of the rare earth metal elements in oxidation state of +4 are not stable in chloride melts, because the reaction occurs according to the following equation: $RE^{4+} + Cl^- = RE^{3+} + 1/2Cl_2$.

However, the multiple oxidation states are also dependent on the electrolyte composition and temperature. In general, the RE^{2+} is more stable in the chloride melts than in the fluoride melts.

Electrolyte System

Usually, binary or ternary systems are used as the supporting electrolyte to satisfy the

Rare Earth Metal Production by Molten Salt Electrolysis, Table 2 The parameters for REM and REM alloy production by molten salt electrolysis

	Chloride system		Fluoride–oxide system	
Rare earth metals	Electrolyte composition	Current efficiency	Electrolyte composition	Current efficiency
La	$LaCl_3$–KCI	30–50 %	LaF_3–LiF–La_2O_3	Max 87 %
Ce	$CeCI_3$–KCI	30–50 %	CcF_3–LiF–Ce_2O_3	
Pr	$PrCl_3$–KCI	35–40 %	PrF_3–LiF–Pr_2O_3	Max 80 % ~ 82 %, 10kA, max 24kA
Nd	$NdCl_3$–KCI	Very low	NdF_3–LiF–Nd_2O_3	80 % ~ 82 %,10kA
Gd			GaF_3–LiF–Ga_2O_3 Ga–Fe alloy	
Dy			D_Y–Fe alloy	Max 80 %
Yb			YbF_3–LiF–Yb_2O_3	
Mixed rare earth metals	$ReCl_3$–KCl	35–50 %	RE_20_3–REF_3–LiF	65 %

The current efficiency is obtained from the industrial data

requirements for viscosity, density, conductivity, and melting point of the molten salts. When $RECl_3$ is selected as the raw material, according to the theoretical decomposition voltages of chlorides in Table 3, Li (Na, KCl, Rb, Cs)Cl or Be (Mg, Ca)Cl_2 are suitable for the supporting electrolytes, usually KCl–$RECl_3$ is applied in the industry due to the comprehensive properties. Most of the rare earth metal fluorides have presented higher theoretical decomposition voltages than their chlorides, and some even are close to the alkaline and alkaline earth fluorides. Only LiF, CaF_2, SrF_2, and BaF_2 can satisfy the requirements for the supporting electrolyte for the active rare earth metal oxide components such as Nd_2O_3 and La_2O_3 as given in Table 4. The electrolyte is generally composed of Re_2O_3–LiF–ReF_3.

Rare Earth Metal Production by Molten Salt Electrolysis, Table 3 The theoretical decomposition voltages for chlorides

T/°C E/V	400	600	800	1,000	1,200	1,400
LiCl	3.66	3.49	3.37	3.26	3.16	3.06
NaCl	3.61	3.42	3.24	3.14	3.00	2.89
KCl	3.86	3.66	3.48	3.35	3.23	3.11
RbCl	3.84	3.65	3.48	3.35	3.22	3.10
CsCl	3.90	3.71	3.56	3.43	3.31	3.20
$BeCl_2$	2.04	1.92	1.81	1.72	1.63	1.55
$MgCl_2$	2.77	2.61	2.47	2.36	2.25	2.14
$CaCl_2$	3.59	3.44	3.29	3.17	3.05	2.93
$SrCl_2$	3.74	3.59	3.44	3.31	3.19	3.07
$BaCl_2$	3.90	3.74	3.58	3.43	3.31	3.19
YCl_3	2.90	2.75	2.60	2.48	2.36	2.24
$LaCl_3$	3.12	2.96	2.81	2.68	2.57	2.46
$CeCl_3$	3.06	2.90	2.75	2.63	2.51	2.41
$PrCl_3$	3.07	2.91	2.76	2.64	2.52	2.41
$NdCl_3$	3.03	2.87	2.72	2.60	2.49	2.38
$PmCl_3$	2.90	2.66	2.41	2.14	1.86	1.57
$SmCl_3$	2.98	2.81	2.68	2.55	2.43	2.31
$EuCl_3$	2.63	2.46	2.33	2.19	2.06	1.94
$GdCl_3$	2.90	2.74	2.61	2.50	2.39	2.28
$TbCl_3$	2.88	2.73	2.60	2.49	2.38	2.27
$DyCl_3$	2.80	2.62	2.45	2.30	2.16	2.02
$HoCl_3$	2.91	2.75	2.60	2.47	2.35	2.23
$ErCl_3$	2.84	2.68	2.52	2.38	2.25	2.13
$TmCl_3$	2.81	2.64	2.48	2.33	2.20	2.07
$YbCl_3$	2.75	2.59	2.43	2.29	2.15	2.02
$LuCl_3$	2.81	2.59	2.36	2.12	1.86	1.60

Electrode Reactions

Chloride Melts

The typical electrode reactions for the chlorides molten salt electrolysis are as follows:

The cathode reaction:

$$RE^{3+} + 3e = RE \quad (1)$$

Rare Earth Metal Production by Molten Salt Electrolysis, Table 4 The theoretical decomposition voltages for fluorides

T/°C E/V	400	600	800	1,000	1,200	1,400
LiF	5.72	5.52	5.32	5.16	5.02	4.89
NaF	5.24	5.02	4.80	4.60	4.45	4.31
KF	5.18	4.97	4.76	4.60	4.45	4.31
RbF	5.08	4.88	4.68	4.54	4.40	4.27
CsF	5.10	4.91	4.75	4.63	4.51	4.39
BeF_2	4.78	4.62	4.48	4.34	4.20	4.06
MgF_2	5.21	5.04	4.86	4.68	4.50	4.35
CaF_2	5.76	5.59	5.42	5.25	5.09	4.93
SrF_2	5.71	5.54	5.37	5.20	5.04	4.88
BaF_2	5.69	5.52	5.36	5.20	5.05	4.90
YF_3	5.37	5.21	5.06	4.90	4.77	4.65
LaF_3	5.29	5.13	4.96	4.80	4.65	4.49
CeF_3	5.25	5.08	4.92	4.75	4.59	4.43
PrF_3	5.25	5.09	4.93	4.77	4.61	4.45
NdF_3	5.22	5.06	4.90	4.74	4.58	4.42
PmF_3						
SmF_3	5.18	5.01	4.85	4.69	4.53	4.38
EuF_3	4.84	4.67	4.50	4.34	4.19	4.04
GdF_3	5.28	5.11	4.95	4.79	4.63	4.50
TbF_3	5.31	5.14	4.98	4.82	4.67	4.54
DyF_3	5.25	5.09	4.93	4.77	4.62	4.50
HoF_3	5.27	5.10	4.94	4.78	4.63	4.49
ErF_3	5.26	5.10	4.93	4.78	4.63	4.51
TmF_3	4.60	4.44	4.27	4.11	3.97	3.85
YbF_3	4.86	4.70	4.55	4.40	4.26	4.14
LuF_3	5.21	5.04	4.88	4.72	4.57	4.45

On the anode reaction:

$$2Cl^- = Cl_2(g) + 2e \quad (2)$$

Therefore, the total reaction is

$$2RECl_3 = 2RE + 3Cl_2(g) \quad (3)$$

Chlorides system is suitable to produce the rare earth metals or intermediate alloys with low melting point. The REM including La, Ce, Pr, and some mixed rare earth metal alloys have been produced from the chloride system. The disadvantages for the chlorides electrolysis lie in high hygroscopicity and volatility of electrolyte and low current efficiency.

Fluoride–Oxide Melts

In the fluoride–oxide system, the corresponding electrode reactions are the following:

The cathode reaction

$$RE^{3+} + 3e = RE \quad (4)$$

The anode reaction

$$3O^{2-} + 2C = CO + CO_2 + 6e \quad (5)$$

The total reaction

$$RE_2O_3 + 2C = 2RE + CO + CO_2 \quad (6)$$

Fluoride–oxide system is suitable to produce high melting point rare earth metals and has been successfully used in production in La, Ce, Pr, Nb, and mixed rare earth alloys with a higher current efficiency than chloride system. But the electricity energy consumption is as high as l0 kWh/kg (REM), while the theoretical value for Nd electrolysis from Nd_2O_3–LiF–NdF_3 melts is 1.334 kWh/kg-Nd, showing utilization efficiency of the electricity energy of less than 16 %. Currently the widely used cell capacity in industry is 5 kA though the highest single cell capacity has already reached 25 kA.

Chlorides Electrolysis

Current Efficiency

It is reported that the maximum current efficiency (CE) for chlorides electrolysis is 70 %, usually in the range of 30–50 % in the industry depending on the operational conditions such as the water content of the raw materials, current density, temperature, and impurities. Especially, the water in the raw materials greatly reduces the current efficiency [2]. Under the same operation conditions, the CE value is mainly related to RE^{2+} stability in the melts. The existence of RE^{2+} in the melts will make the electrode reaction Eq. 7 occur prior to RE^{3+} reduction to metal RE, and the reduction product RE will react with RE^{3+} to form RE^{2+} according to Eq. 8, resulting in the reduction product RE transfer to RE^{2+}, and

therefore current efficiency is reduced by reducing the amount of the RE.

$$RE^{3+} + e \rightarrow RE^{2+} \quad (7)$$

$$RE^{3+} + RE \rightarrow RE2^{+} \quad (8)$$

The higher the stability of RE^{2+} is, the lower the current efficiency is. The stability of RE^{2+} is dependent on the rare earth metal element itself and electrolyte composition. For example, Sm, Eu, and Yb form highly stable RE^{2+} ions in the chloride melts and are unable to obtain corresponding metals by molten salt electrolysis due to a very low current efficiency. If Sm, Eu, and/or Yb ions exist in the chloride system as trace impurities, the current efficiency will be lowered significantly. This is explained later by the electrochemical analysis results. Besides Sm, Eu, and Yb, nearly all the rare earth metal elements form RE^{2+} ions in the chloride melts. For example, in alkaline chloride melts, electrochemical investigation has showed that Nd^{3+} is reduced on an inert cathode through two steps, according to Eqs. 9 and 10. The presence of Nd^{2+} will cause a lower current efficiency. So the chloride electrolytic process is not subject to Nd production in industry. In addition to Nd, the other REM also have similar trends to Nd.

$$Nd^{3+} + e = Nd^{2+} \quad (9)$$

$$Nd^{2+} + 2e = Nd^{0} \quad (10)$$

The possibility of formation and existence of the different oxidation states in molten chlorides is confirmed by direct measurements of redox potentials of lanthanides that were performed by a potentiometric method. The ratio between their concentrations ($[Ln^{3+}]/[Ln^{2+}]$) is related to the redox potentials through the Eq. 11 [3].

$$E_{Ln3+/Ln2+} = E_{Ln3+/Ln2+}* + RT/nF \ln Ln^{3+}/Ln^{2+} \quad (11)$$

where $E_{Ln3+/Ln2+}*$ is a conditional standard redox potentials.

Sm^{3+} Electrochemical Behaviors in Chloride Melts

Sm^{3+}/Sm^{2+} Transformation in Chloride Melts

Stability of samarium ions (Sm^{3+}, Sm^{2+}) in the alkaline chloride melts changes as functions of the solvent salt cations and temperature [4]. Sm^{3+} exhibits a higher stability for a larger solvent salt cation and lower temperature. Electrochemical reduction of Sm^{3+} into Sm^{0} in KCl–NaCl–CsCl melt at an inert cathode has been found to occur in two steps as shown in Eqs. 12 and 13. And the reduction of Sm^{2+} to Sm^{0} takes place at near the decomposition potential of the supporting electrolyte. In addition, Sm^{2+} losing one electron to form Sm^{3+} takes place at the anode in terms of reaction Eq. 14, making $Sm^{2+} \rightarrow Sm^{3+}$/transformation at the electrodes; therefore, this process can circulate in the cathode and anode, and therefore nearly no Sm metal can be obtained at the cathode, resulting an extremely low current efficiency. This is the reason why samarium cannot be produced from the chloride melts by molten salt electrolysis. It is reported that when the concentration of Sm^{3+} ions reach 0.1 wt% in the chloride melts, the current efficiency will be substantially decreased. Eu^{3+} behaves in nearly the same manner as Sm^{3+} in the chloride melts.

$$Sm^{3+} + e = Sm^{2+} \quad (12)$$

$$Sm^{2+} + e = Sm^{0} \quad (13)$$

$$Sm^{2+} - e = Sm^{3+} \quad (14)$$

The Redox Potentials of Sm^{3+}/Sm^{2+}

The conditional standard potentials $E^{0}{}_{(Ln3+/Ln2+)}$ on the inert electrode [5] are strongly affected by the salt solvents. For example, at 1,073 K, these potentials were −1.880 and −0.742 V in molten equimolar KCl–CsCl mixture [6], −1.966 and −0.844 V in molten KCl [7], and −2.087 and −0.981 V in molten CsCl, for samarium and europium, respectively. The dependence of the conditional standard potentials Sm^{3+}/Sm^{2+} changes inversely with the cationic radii of the solvent.

While samarium ions are electrochemically reduced on an active electrode, such as nickel, silver, and aluminum electrodes, Sm alloy is formed with the electrode material according to Eqs. 15 and 16:

$$Sm^{2+} + 2e\ (Al) = Sm_xAl_y(alloy) \quad (15)$$

$$Sm^{2+} + 2e\ (Ag) = Sm_xAg_y(alloy) \quad (16)$$

For example, electroreduction of samarium ions in KCl–NaCl–CsCl eutectic melts on Pt electrode involves reduction of Sm^{3+} into Sm^{2+} at the potentials of −1.2 to −1.4 V, and the reduction at more negative potentials about −2.3 to −2.4 V corresponds to that of Sm^{2+} to Sm^0 and formation of Pt_xSm_y intermetallide confirmed by the voltammetry [4].

The Stability of RE^{2+} in the Chloride Melts

The stability of the divalent and trivalent rare earth metals ions may be judged upon by comparing the standard Gibbs energies of the $RECl_2$ and $RECl_3$ formation in a given condition. The relative stability of the two valences in the molten salts can be expressed by the equilibrium constant for the disproportionation reaction according to Eq. 17. Obviously, the more constant the equilibrium of the reaction to the right hand is, the more instable for the divalence is, and vice versa. The stability of the ions is dependent on the temperature, cation, and anion types, for example, divalence of the rare earth metals is more stable in the chloride system than in the fluoride–oxide system:

$$3RE^{2+} = 2RE^{3+} + RE \quad (17)$$

Fluoride–Oxide Electrolysis

Current Efficiency

Currently, molten fluoride–oxide electrolysis has been widely applied to produce a single rare earth metal such as La, Ce, Pr, and Nd and mixed rare earth metals such as Gd–Fe, Dy–Fe Ho–Fe, and Er–Fe alloys in industry. The maximum cell capacity has reached 25 kA, and the current efficiency is usually above 80 % with an energy consumption of about 10.6 kWh/kg. Clearly, fluoride–oxide electrolysis has shown a higher current efficiency than chloride electrolysis. This is attributed to the positive effects of F^- on the stability of the higher oxidation state

Nd^{3+} Cathodic Processes

LiF–NdF_3

According to references [8, 9], the reduction process involves one step Eq. 18 in mixed chloride–fluoride melts, while two steps in pure chloride melts as shown in Eqs. 8 and 9.

$$Nd^{3+} + 3e \rightarrow Nd \quad (18)$$

The addition of fluoride ions in chloride melts can stabilize the higher valences of cationic species, and thus, the intermediate step Eq. 9 is not pronounced in the fluoride–chloride melts [8]. Cyclic voltammetry [10] on a molybdenum electrode in LiF–NdF_3 melts at 810 °C has proved that reduction of Nd^{3+} ions into Nd in a single step; this is also confirmed by C. Hamela [11]. It is proved that the electrochemical reduction process is controlled by the diffusion of neodymium ions in the melts.

LiF–NdF_3–Nd_2O_3 System

The voltammetric characteristics of LiF–NdF_3 and LiF–NdF_3–Nd_2O_3 on tungsten electrodes at 900 °C are shown in Figs. 1 and 2 [12]. Due to much higher concentration of $[NdF_6]^{3-}$ species in the melts, the voltammetric characteristics for the two melts with or without Nd_2O_3 are similar.

The structure of the trivalent neodymium fluoride species in the melt is the octahedral $[NdF_6]^{3-}$ complex anion identified by Raman spectroscopy [13]. The dissolution of Nd_2O_3 results in the formation of neodymium oxyfluorides in the melts. It also has been found that the $[NdOF_5]^{4-}$ is present [10]. Actually, $[NdF_6]^{3-}$ and $[NdOF_5]^{4-}$ coexist in the melt since the concentration of NdF_3 is much

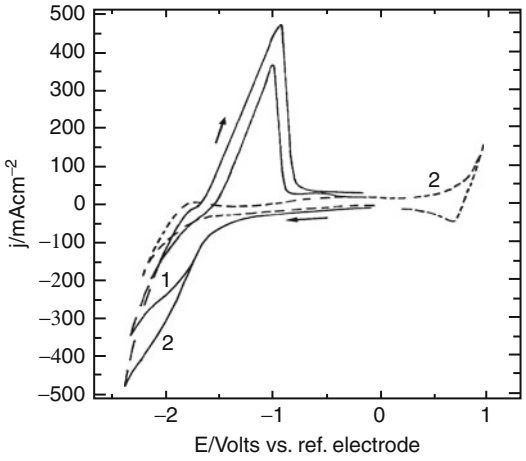

Rare Earth Metal Production by Molten Salt Electrolysis, Fig. 1 CV of fused LiF without (– – –) and with (—) NdF_3 (1 mol%) on tungsten electrode at 900 °C. dE/dt (mV s^{-1}) : (1) 20, (2) 100 [10]

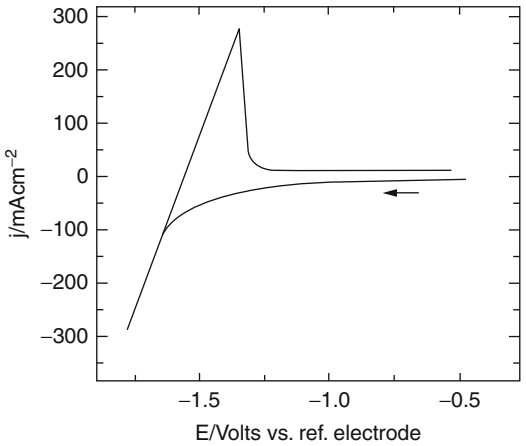

Rare Earth Metal Production by Molten Salt Electrolysis, Fig. 2 CV of LiF–NdF_3 eutectic composition melt with Nd_2O_3 on tungsten electrode at 900 °C; dE/dt = 100 mV s^{-1}[10]

higher than that of Nd_2O_3. While at the anode the oxidation of neodymium oxyfluorides $[NdOF_5]^{4-}$ generates oxygen according to the following Eqs. 19 and 20. This has been confirmed by the Ref. [14] that oxygen generation at the anode during the electrolytic production of neodymium from oxide–fluoride melts. The produced oxygen subsequently reacts with the carbon anode and then CO and CO_2 gases are produced.

$$2[NdF_6]^{3-} + 6e = 2Nd(s) + 12\ F^- \quad (19)$$

$$3[NdOF_5]^{4-} + 3F^- = 3/2O_2(g) + 3[NdF_6]^{3-} + 6e \quad (20)$$

However, in LiF–NdF_3–Nd_2O_3 melts, whether NdF_3 or Nd_2O_3 is consumed at the electrode is still controversial. Tamamura et al. [15] claim that NdF_3 is the raw material in the electrolytic production of neodymium in oxide–fluoride melts. According to Kaneko et al. [14], Stefanidaki [13], and Keller [16], only Nd_2O_3 is consumed by controlling the cell voltage in a low region. More work is needed to prove the above points.

Conclusions

In this chapter, the two electrolyte systems are introduced to produce rare earth metals by molten salt electrolysis. The involved electrode processes, current efficiency, and the oxidation states of the rare earth metal ions and their stability have been discussed. The lower current efficiency for chloride melts is caused by the higher stability of divalent ions of rare earth metals in the melts. Fluoride ions have lowered the stability of divalent ions; therefore a higher current efficiency is reached in the fluoride–oxide system. As an example, the electrochemical reduction process for NdF_3 and Nd_2O_3 has been discussed.

Future Directions

In the last two decades the world production of rare earth has increased remarkably. However, compared to the modern aluminium electrolysis Héroult-Hall cell, the electricity energy consumption for rare earth electrolysis is still very high due to the low current efficiency ($\leq$80%) and very high cell voltage ($\geq$10V). Therefore, reducing the energy consumption for rare earth

electrolysis will be the major future direction. It is also worth to mention that the anode gas management for the rare earth electrolysis should be considered to eliminate the emission of perfluorocarbons (PFCs, CF_4 and $C2F_6$).

Cross-References

► Refractory Metal Production by Molten Salt Electrolysis

References

1. Hecheng Lin (2000) World nonferrous metal. 3:9–13
2. Zhiqiang Zhao, Haijun Jia, Bingyi Yan (2005) Science and Technology of Baotou Steel Corporation, vol. 31, Supplement. Nov 2005
3. Khokhlov VA, Novoselova AV, Nikolaeva EV, Tkacheva OY, Salyulev AB (2007) Russ J Electrochem 43(8):961–967
4. Kushkhov KB, Vindizheva MK, Karashaeva RA, Tlenkopachevz MR (2010) Russ J Electrochem 46(6):691–701
5. Novoselova AV, Khokhlov VA, Shishkin VY (2001) Russ J Appl Chem 74(10):1672–1677
6. Novoselova AV, Shishkin VY, Khokhlov VA (1999) Rasplavy 6:32339
7. La–Lu Sc Y (1982) Gmelin handbook of inorganic chemistry: Rare Earth Elements, Part C 4b. Springer, Berlin
8. Mottot Y (1986) Thesis, University of Pierre et Marie Curie
9. Castrillejo Y, Bermejo MR, Barrado E, Martinez AM, Diaz Arocas P (2003) J Electroanal Chem 545:141
10. Stefanidaki E, Hasiotis C, Kontoyannis C (2001) Electrochim Acta 46:2665–2670
11. Hamela C, Chamelot P, Taxil P (2004) Electrochim Acta 49:4467–4476
12. Thoma RE (1966) Progress in science technology of the rare earths, vol 2. Pergamon Press, New York, p 90
13. Stefanidaki E, Photiadis GM, Hasiotis C, Kontoyannis C (2000) In: Berg R, Hjuler HA (eds) Progress in molten salt chemistry, vol 1. Elsevier, Paris, p 505
14. Kaneko A, Yamamoto Y, Okada C (1993) J Alloys Compd 193:44
15. Tamamura H, Shimooka T, Utsunomiya M (1990) Proc Seventh Int Symp Molten Salts 90–17:611
16. Keller R, Larimer KT (1997) Rare earths: science, technology and applications III. The Minerals, Metals & Materials Society, 175

Reactive Metal Electrode

Hirofumi Maekawa
Department of Materials Science and Technology, Nagaoka University of Technology, Nagaoka, Japan

Definition, Characteristics, and Advantages

In electrochemistry, a typical reaction cell is mainly composed of anode, cathode, reference electrode, and diaphragm. In most of the cathodic reduction, a diaphragm is required, which sometimes demands continuous electrolysis under high voltage. Some kinds of metal are used as an anode to decrease voltage between electrodes in practical electrochemical synthesis. Such electrodes are called sacrificial electrode, sacrificial anode, or sacrificial metal anode, and it is a nice tool in organic electrochemical synthesis [1–4]. Ionization of the metal material at the anode means the supply of one electron to the anode. The generated electron is used for passing current. Recently, sacrificial metal anode is positively applied to electrochemical synthesis, and the metal ion derived from anode sometimes plays important roles in chemical reaction and gives remarkable influences to regiochemistry, stereochemistry, selectivity of the products by coordination, catalytic effects, formation of a new reagent in situ, etc. [5, 6]. In these cases, the electrode is especially called reactive electrode, reactive anode, or reactive metal anode, but "reactive electrode" may be used as the same technical term instead of sacrificial electrode. Magnesium, aluminum, and zinc are generally available for reactive metal anodes, and an aprotic polar solvent such as DMF or NMP is frequently used as the solvent. There are also some reports on mixed electrode of carbon and sulfur [7] and on the Reformatsky reaction by behavior of the anode surface as activated zinc metal [8].

Application of reactive metal electrode gives several advantages in electrochemical synthesis.

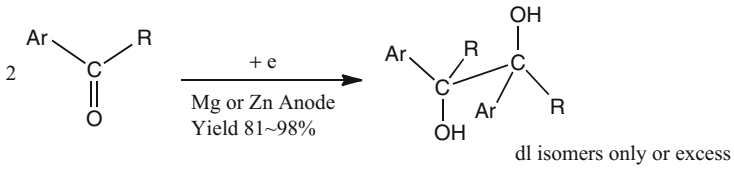

Reactive Metal Electrode, Scheme 1 Stereoselective synthesis of pinocols

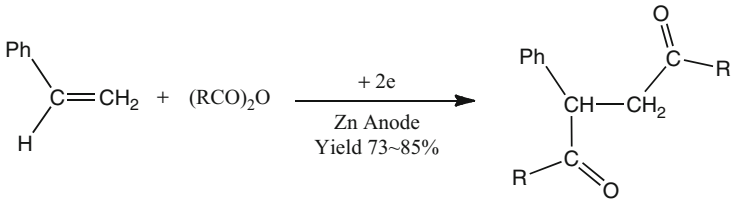

Reactive Metal Electrode, Scheme 2 Diacylation of Styrenes

First one is electrolysis under low voltage without diaphragm. Second one is decreasing the amount of supporting electrolyte because the generated metal ion will continuously dissolve in the solvent and help carrying the current. Third one is appearance of different selectivity by behavior of the metal ion under electrolysis. In some cases, good choice of reactive metal anode material sometimes gets an organic compound with the metal ion to form an organometallic reagent and improves the yield of the reaction. Furthermore, suppression of oxidizing organic compounds at the anode is also a positive effect of reactive metal anode. A suitable reactive metal anode has to be chosen with consideration on redox potential of reagents and products.

Examples and Synthetic Application

In the early years after development of sacrificial electrode (reactive metal anode), some reviews were reported [1, 2, 4]. Many experimental results are also reported in recent years and typical examples of the reactions are shown below:

1. Diastereoselective Synthesis of Pinacols [9]

   Electrochemical reduction of benzaldehydes and aromatic ketones with zinc or magnesium anode gave the corresponding homo-coupling compounds, 1,2-diol, with high diastereoselectivity in high yield. Stereochemistry of the product is controlled by oxygen-metal-chelate complex. The metal ion is derived from the anode material in the electrochemical reaction.
2. Fixation of Carbon Dioxide [10]

   Electrochemical carboxylation of organic halides with aluminum, zinc, or magnesium anode brought about the selective formation of carboxylic acids in high yield. Carboxylation of organic halides suffered from esterification of carboxylate anion with unreacted organic halide. This method enabled us to synthesize carboxylic acids by trapping carboxylate anion with metal ion.
3. Synthesis of Drugs [11]

   Electrochemical carboxylation of a-halogenated arenes under the carbon dioxide atmosphere with zinc anode afforded the effective formation of phenylpropionic acid derivatives in high yield. This method is application of carboxylation of aromatic halides with reactive metal anode to synthesis of *anti*-inflammatory pharmaceutical drugs.
4. Nickel-Catalyzed Electroreductive Coupling [12]

   Nickel-catalyzed electroreductive homo-coupling reaction of organic halides and coupling reaction between organic halide and activated olefins could be carried out with iron anode in ionic liquid. With addition of small amount of DMF, coupling compounds were obtained at room temperature in good to high

yield. This method is characterized by use of aromatic halide and nickel salt.

5. Electrochemical Synthesis of Polysilanes [13]
   Electrochemical reduction of 1,1-dichlorodialkylsilanes and 1,2-dichlorotetraalkyldisilanes with magnesium anode in an undivided cell gave the corresponding polysilanes. Magnesium electrode was only effective for this synthesis of polysilanes, and platinum, zinc, nickel, and copper were less effective. This method is an application of this reactive metal anode to attractive polymer synthesis.
6. 1,2-Diacylation of Styrenes and Activated Olefins [14]
   Electroreduction of styrenes or alkyl methacrylates in the presence of aliphatic acid anhydrides or N-acylimidazoles with zinc anode brought about novel one-pot vicinal double C-acylation to afford the corresponding 1,4-diketones in good to high yields. This is an example of cross-coupling reaction with no use of halogenated compounds.

Future Directions

It is quite interesting to know what the reactive metal anode plays a role in, but it is not easy to analyze the effects because the role of the reactive metal anode may be different, depending on a kind of the metal or each reaction. However, development of reactive metal anode exploited a new field of electrochemical synthesis in this 30 years. Typical examples are selective synthesis of carboxylated compounds, cross-coupling reaction of activated halogenated compounds and carbonyl compounds, and cross-coupling reaction between non-halogenated compounds. In recent years, many types of transition metal-catalyzed reactions have been reported in the field of organic synthesis, and some professors received the Nobel Prize on cross-coupling reactions. From the view of electrochemical synthesis and green sustainable chemistry, novel methods of reactive metal anode will be developed with involving application of transition metal-catalyzed reactions, ionic liquids, recovery of anode material, elemental strategy, etc.

Cross-References

- ▶ Electrochemical Fixation of Carbon Dioxide (Cathodic Reduction in the Presence of Carbon Dioxide)
- ▶ Electrosynthesis in Ionic Liquid
- ▶ Electrosynthesis of Polysilane

References

1. Chaussard J, Folest JC, Nedelec JY, Perichon J, Sibille S, Troupel M (1990) Use of sacrificial anodes in electrochemical functionalization of organic halides. Synthesis 5:369–381. doi:10.1055/s-1990-26880
2. Silvestri G, Gambino S, Filardo G (1991) Use of sacrificial anodes in synthetic electrochemistry. Processes involving carbon dioxide. Acta Chem Scand 45:987–992. doi:10.3891/acta.chem.scand.45-0987
3. Lund H, Hammerich O (Eds.) (2001) Organic electrochemistry 4th ed. Marcel Dekker, New York
4. Tokuda M (2006) Efficient fixation of carbon dioxide by electrolysis – facile synthesis of useful carboxylic acids – J Natur Gas Chem 15:275–281. doi:10.1016/S1003-9953(07)60006-1
5. Lehmkuhl H (1973) Preparative scope of organometallic electrochemistry. Synthesis 7:377–396. doi:10.1055/s-1973-22221
6. Tuck DG (1979) Direct electrochemical synthesis of inorganic and organometallic compounds. Pure Appl Chem 51:2005–2018. doi:10.1351/pac197951102005
7. Guillanton GL Do QT Simonet J (1990) Electrogenerated electrophilic reagents from sulphur: a new access to bis-methoxyaryl sulphides. J. C. S. Chem Commun: 1990:393–394. doi:10.1039/C39900000393
8. Schwarz KH, Kleiner K, Ludwig R, Schick H (1992) Electrochemically supported Reformatskii reaction: a convenient preparation of 2-substituted 1-ethyl 3-oxoalkanedioates. J Org Chem 57:4013–4015. doi:10.1021/jo00040a051
9. Thomas HG, Littmann K (1990) The use of sacrificial anodes for diastereoselective formation of pinacols. Synlett 12:757–758. doi:10.1055/s-1990-21241
10. Silvestri G, Gambino S, Filardo G, Gulotta A (1984) Sacrificial anodes in the electrocarboxylation of organic chlorides. Angew Chem Int Ed Engl 23:979–980. doi:10.1002/anie.198409791
11. Yamauchi Y, Hara S, Senboku H (2010) Synthesis of 2-aryl-3,3,3-trifluoropropanoic acids using electrochemical carboxylation of (1-bromo-2,2,2-trifluoroethyl)arenes and its application to the

synthesis of β, β, β-trifluorinated non-steroidal *anti*-inflammatory drug. Tetrahedron 65:473–479. doi:10.1016/j.tet.2009.11.053
12. Barhdadi R Courtinard C Nédélec JY Troupel M (2003) Room-temperature ionic liquids as new solvents for organic electrosynthesis. The first examples of direct or nickel-catalysed electroreductive coupling involving organic halides. Chem Comm 1434–1435. doi:10.1039/B302944A
13. Shono T Kashimura S Ishifune M Nishida R (1990) Electroreductive formation of polysilanes. J Chem Soc Chem Comm: 1160–1161. doi:10.1039/C39900001160
14. Yamamoto Y, Goda S, Maekawa H, Nishiguchi I (2003) Novel one-pot vicinal double C-acylation of styrenes and methacrylates by electroreduction. Org Lett 15:2755–2758. doi:10.1021/ol035020v

Reconstituted Redox Proteins on Surfaces for Bioelectronic Applications

Claudia Ley[1] and Dirk Holtmann[2]
[1]DECHEMA Research Institute, Frankfurt am Main, Germany
[2]DECHEMA Research Institute of Biochemical Engineering, Frankfurt am Main, Germany

Introduction

Many redox proteins contain a cofactor or more precisely a prosthetic group as a nondiffusible organic or inorganic compound located at the enzyme's active site. The cofactor plays an essential role for the enzyme's catalytic activity [1]. It is linked firmly to the protein backbone, and the linkage may be of non-covalent or covalent nature and is often accompanied by additional interactions between the cofactor and its protein surrounding (e.g., ionic or hydrophobic). The most prominent examples for cofactors of organic origin are heme and flavin adenine dinucleotide (FAD) which can be found in myoglobin and hemoglobin or in case of FAD in glucose oxidase (Fig. 1). Furthermore, pyrroloquinoline quinone (PQQ), the cofactor of, e.g., certain alcohol dehydrogenases, is of interest since it functions not only as cofactor but also as redox shuttle [1]. Inorganic cofactors like certain metal clusters can be found, e.g., in nitrogenases and hydrogenases. A further example is photosystem I, a protein complex participating in photosynthesis, which displays both, a quinone cofactor as well as several iron-sulfur clusters [2].

Extraction of the Prosthetic Group from the Holoprotein

The prosthetic group can be removed from the holoprotein, which is the complete functional protein unit, to yield the cofactor-free apoprotein (Fig. 2). This can be done in several ways which include dialysis, extraction with an organic solvent, or chromatographic steps. Most prominent is the method developed by Teale for the extraction of non-covalently bound heme [3]. After acidification of the solution, resulting in partial denaturation of the protein, the heme cofactor is extracted with methyl ethyl ketone yielding an organic heme-containing and an aqueous apoprotein-containing phase. The method has been applied, e.g., for myoglobin, hemoglobin, horseradish peroxidase, and catalase [3]. The preparation of the apoprotein as well as the reconstitution depends strongly on protein structure and the position of the cofactor in the protein [1]. For example, the heme of myoglobin is located close to the surface of the protein, and preparation of functional myoglobin apoprotein is well described. In contrast for P450 enzymes, apoprotein preparation is not easy since the protein has to be denatured to a high extent to access the deeply buried heme. Nevertheless, some interesting approaches have been developed to overcome these problems like heme transfer from the P450 to apomyoglobin [4]. When the prosthetic group is linked covalently to the protein, one option is also the direct expression of the apoprotein [5].

Apoprotein Reconstitution

The apoprotein can be reconstituted with its natural cofactor or an artificial one to obtain

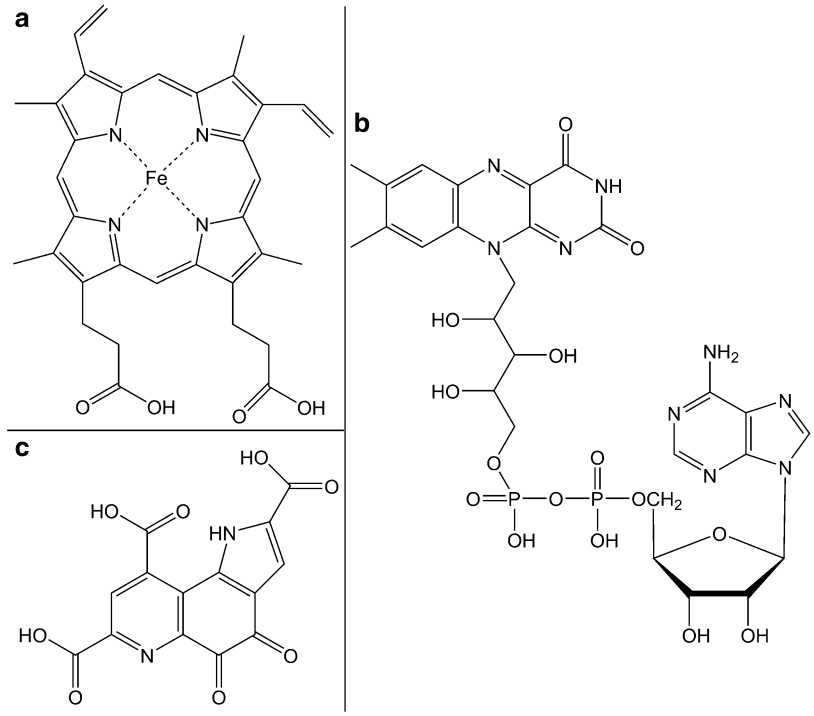

Reconstituted Redox Proteins on Surfaces for Bioelectronic Applications, Fig. 1 Structures of three prominent cofactors: (**a**) heme b (or iron protoporphyrin IX), (**b**) FAD, and (**c**) PQQ

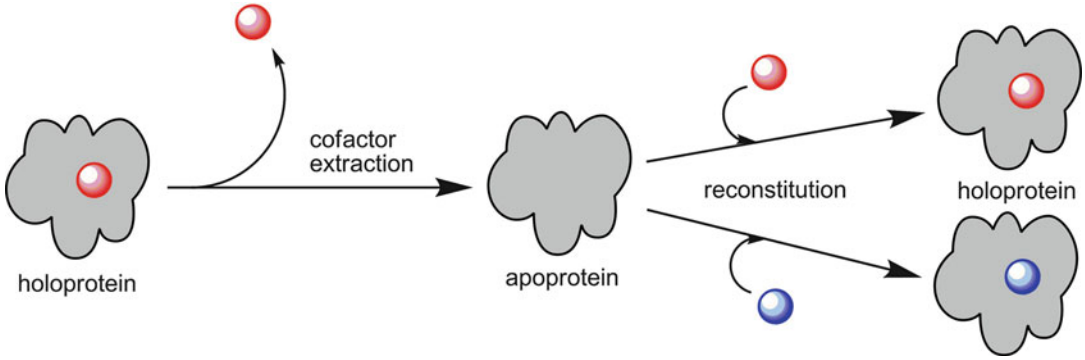

Reconstituted Redox Proteins on Surfaces for Bioelectronic Applications, Fig. 2 Extraction of the cofactor (*red*) from the holoprotein (*left*) yielding the apoprotein (*center*). The apoprotein can be reconstituted with the natural (*red*) or an artificial cofactor (*blue*) to yield again a functional holoprotein (*right*)

a functional holoenzyme (Fig. 2). The holoenzyme often displays a changed catalytic behavior when reconstituted with a nonnatural cofactor. In this way, it has been possible to evaluate catalytic mechanisms and gain insight into enzyme kinetics. The introduction of a modified cofactor which lacks the covalent binding site opens up the possibility to get information about the nature of the covalent bonding and if this bonding is necessary for catalysis. Furthermore, by changing substituents at the cofactor, the relation between its structure and electron transfer properties yields important information [6].

Reconstituted Redox Proteins at Electrode Surfaces

Several studies deal with direct electrochemistry of reconstituted myoglobin at hydrophilic electrode surfaces with nonnatural cofactors where, for example, substituents at the heme porphyrin ring or the central metal cation have been changed [6]. Thereby incorporation of an artificial heme resulted in shifts of the redox potential, alteration in electrode transfer kinetics, as well as different ligand-binding properties. In bioelectronic applications, redox proteins can normally not be attenuated directly via the electrode since they possess an insulating protein shell. One way to establish an electrical contact between the electrode and the protein's active site is the reconstitution with a cofactor to which an electroactive group has been bound so that the accessibility of the active site for electron transfer is improved. This has been done, for example, with myoglobin, to whose heme cofactor a photoactivable ruthenium group has been coupled [7]. As a result for the ruthenium reconstituted myoglobin electron transfer could be induced by light irradiation which is not seen for native myoglobin [7]. Another example for a photochemical approach is the reconstitution of the flavoprotein glucose oxidase at a photoisomerizable monolayer to which FAD was bound. In this study, the assembly could be converted from an insulating to a charge-transporting state by light irradiation [8]. Furthermore, glucose oxidase and D-amino acid oxidase have been reconstituted with ferrocene-modified FAD [9]. The artificial holoenzymes show direct electrical communication with the electrode and respond well to different substrate concentrations implying a possible use for amperometric biosensors. Also coupling of a ferrocene unit to hemin and reconstitution with horseradish peroxidase yielded a catalytically active enzyme which displays electroactivity [10]. The redox active groups introduced work as an electron relay or wire and enable a long-range electron transfer. The attachment of the cofactor to gold nanoparticles, or other nanomaterials like carbon nanotubes, facilitates electron transfer to the active site as it has been shown for glucose oxidase or PQQ (Fig. 3) [11, 12]. This is done in combination with immobilization of the nanomaterial-bound cofactor at an electrode surface where the nanoparticle may serve as an electron relay to the macroelectrode. Besides the direct access to the active site, the advantage of immobilizing the cofactor at an electrode surfaces is also the short distance between the electrode and the enzyme and the defined orientation of the reconstituted protein. Electrode surface modifications include mainly self-assembled monolayer systems (Fig. 3) or functionalized polymers. In addition to nanoparticles, the immobilization of PQQ at modified electrodes should be mentioned since it is used for the production of enzyme electrodes due to its electron shuttling function (Fig. 3). For example, apo-glucose dehydrogenase was reconstituted at a polyaniline/polyacrylic acid polymer modified with PQQ [13], and cholesterol oxidase was reconstituted with FAD which has been complexed to a PQQ-containing SAM [14]. Other interesting approaches include the reconstitution with DNA-modified cofactors, which are characterized by their good molecular recognition properties [15]. DNA oligomers were bound to hemin and reconstitution with apomyoglobin and apo-horseradish peroxidase to give catalytically active enzymes. The reconstituted proteins were immobilized at a surface by hybridization of the heme-bound DNA oligomer with its surface-bound counterpart [15]. Also in vivo reconstitution of apo-glucose dehydrogenase in *E.coli* cells was observed electrochemically at carbon paste electrodes [16].

Future Directions

Reconstituted proteins are of special interest for applications in biofuel cells, biosensors, bioelectronics, and nanobiotechnology since direct electron transfer between an electrode and

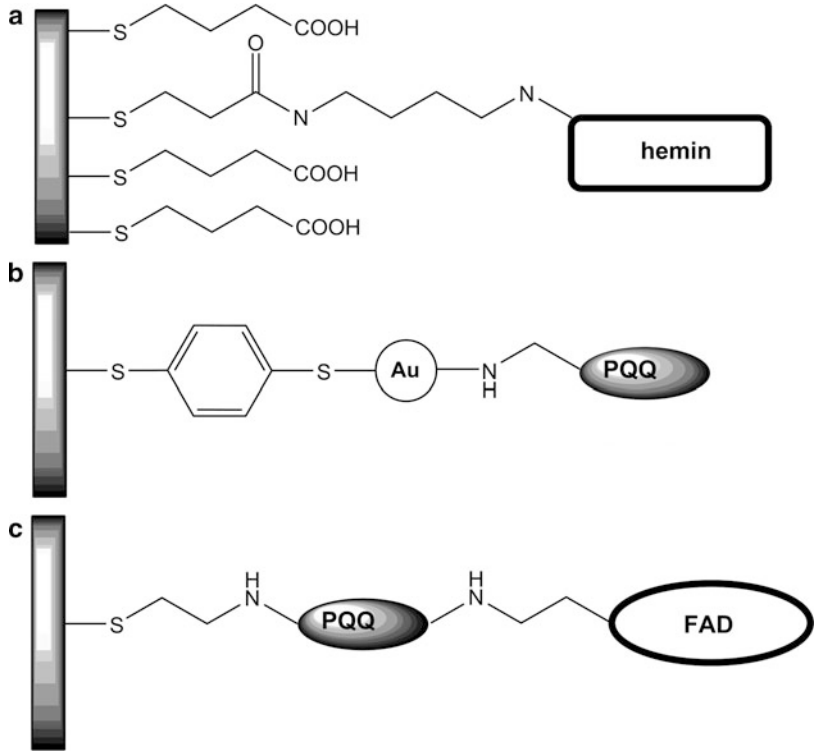

Reconstituted Redox Proteins on Surfaces for Bioelectronic Applications, Fig. 3 Immobilization of cofactors at gold electrodes (*left*) modified with self-assembled monolayers (SAM). (**a**) Immobilization of hemin at a SAM. This assembly was subsequently used for the reconstitution of horseradish peroxidase [17]. (**b**) Immobilization of the cofactor PQQ at an Au nanoparticle, which in turn is immobilized at the electrode via a SAM, for the reconstitution of glucose dehydrogenase [12]. (**c**) Immobilization of the cofactor FAD for reconstitution of glucose oxidase [18]. As electron relay, PQQ has been immobilized via a SAM in between the electrode and the cofactor

the cofactor at the enzymes active site is established. The reconstitution method enables a direct manipulation of the active site and may be used for production of tailor-made biocatalysts converting substrates of interest. Due to the unique orientation of reconstituted proteins at surfaces, they serve as molecular scaffolds for nanostructuring of surfaces.

Cross-References

- ▶ Biosensors, Electrochemical
- ▶ Cofactor Regeneration, Electrochemical
- ▶ Cofactor Substitution, Mediated Electron Transfer to Enzymes
- ▶ Direct Electron Transfer to Enzymes

References

1. Fruk L, Kuo C-H, Torres E, Niemeyer CM (2009) Rekonstitution von Apoenzymen als chemisches Werkzeug für die strukturelle Enzymologie und Biotechnologie. Angew Chem 121:1578–1603
2. Iwaki M, Itoh S (1989) Electron transfer in spinach photosystem I reaction center containing benzo-, naphtho- and anthraquinones in place of phylloquinone. FEBS Lett 256:11–16
3. Teale FWJ (1959) Cleavage of the heam-protein link by acid methylethylketone. Biochim Biophys Acta 35:543
4. Muller-Eberhard U, Liem HH, Yu CA, Gunsalus IC (1969) Removal of Heme from cytochrome P-450$_{CAM}$ by hemopexin and apomyoglobin associated with loss of P-450 hydroxylase activity. Biochem Biophys Res Commun 35:229–235
5. Kim J, Fuller JH, Kuusk V, Cunane L, Z-w C, Mathews FS, McIntire WS (1995) The cytochrome

subunit is necessary for covalent FAD attachment to the flavoprotein subunit of p-cresol methylhydroxylase. J Biol Chem 270:31202–31209
6. Mie Y, Sonoda K, Neya S, Funasaki N, Taniguchi I (1998) Electrochemistry of myoglobins reconstituted with azahemes and mesohemes. Bioelectrochem Bioenerg 46:175–184
7. Hamachi I, Tanaka S, Shinkai S (1993) Light-driven activation of reconstituted myoglobin with a ruthenium tris(2,2'-bipyridine) pendant. J Am Chem Soc 115:10458–10459
8. Yehezkeli O, Moshe M, Tel-Vered R, Feng Y, Li Y, Tian H, Willner I (2010) Switchable photochemical/electrochemical wiring of glucose oxidase with electrodes. Analyst 135:474–476
9. Riklin A, Katz E, Willner I, Stocker A, Bückmann AF (1995) Improving enzyme-electrode contacts by redox modification of cofactors. Nature 376:672–675
10. Ryabov AD, Goral VN, Gorton L, Csöregi E (1999) Electrochemically and catalytically active reconstituted horseradish peroxidase with ferrocene-modified hemin and an artificial binding site. Chem Eur J 5:961–967
11. Xiao Y, Patolsky F, Katz E, Hainfeld JF, Willner I (2003) "Plugging into enzymes": nanowiring of redox enzymes by a gold nanoparticle. Science 299:1877–1881
12. Zayats M, Katz E, Baron R, Willner I (2005) Reconstitution of apo-glucose dehydrogenase on pyrroloquinoline quinone-functionalized au nanoparticles yields an electrically contacted biocatalyst. J Am Chem Soc 127:12400–12406
13. Laurinavicius V, Kurtinaitiene B, Liauksminas V, Ramanavicius A, Meskys R, Rudomanskis R, Skotheim T, Boguslavsky L (1999) Oxygen insensitive glucose biosensor based on PQQ-dependent glucose dehydrogenase. Anal Lett 32:299–316
14. Vidal J-C, Espuelas J, Castillo J-R (2004) Amperometric cholesterol biosensor based on in situ reconstituted cholesterol oxidase on an immobilized monolayer of flavin adenine dinucleotide cofactor. Anal Biochem 333:88–98
15. Fruk L, Niemeyer CM (2005) Covalent hemin–DNA adducts for generating a novel class of artificial heme enzymes. Angew Chem Int Ed 44:2603–2606
16. Iswantini D, Kano K, Ikeda T (2000) Kinetics and thermodynamics of activation of quinoprotein glucose dehydrogenase apoenzyme in vivo and catalytic activity of the activated enzyme in *Escherichia coli* cells. Biochem J 350:917–923
17. Zimmermann H, Lindgren A, Schuhmann W, Gorton L (2000) Anisotropic orientation of horseradish peroxidase by reconstitution on a thiol-modified gold electrode. Chem Eur J 6:592–599
18. Willner I, Heleg-Shabtai V, Blonder R, Katz E, Tao G (1996) Electrical wiring of glucose oxidase by reconstitution of FAD-modified monolayers assembled onto au-electrodes. J Am Chem Soc 118:10321–10322

Redox Capacitor

Shigeaki Yamazaki and Masashi Ishikawa
Kansai University, Suita, Osaka, Japan

Introduction

Today, electrochemical capacitors (ECs), often called "electric double-layer capacitors," "supercapacitors," "ultracapacitors," and so on, have attracted worldwide research interest because of their potential applications as energy storage devices in many fields. The drawback of ECs is certainly their limited energy density, which restricts applications to power density over only few seconds. According to the situation, many research efforts have focused on designing new materials to improve energy and power density [1].

The energy capacity of ECs arises from either double-layer capacitance for electric double-layer capacitors (EDLCs) or pseudocapacitance for redox capacitors [2, 3]. The energy storage mechanism of EDLCs is based on non-faradic phenomena in electric double layer formed at an electrode/electrolyte interface. In regard to electrode active materials for EDLCs, carbon materials such as activated carbons have been most widely used [4] because of their reasonable cost, good electrical conductivity, and high specific surface area. However, there is a limitation in their specific capacitance; the gravimetric capacitance of most carbon materials does not linearly increase with an increase in the specific surface area above $\sim$1,200 $m^2\ g^{-1}$ [5].

On the other hand, pseudocapacitance arises from a faradic reaction at an electrode surface as an oxidation or reduction process, which can provide higher capacitance and/or higher power capability than carbon electrodes utilized in conventional EDLCs. Electrode materials that exhibit such pseudocapacitive storage are typically organic materials such as conducting polymers and transition metal oxides [2, 4].

Organic Materials

Many investigators have reported promising research on ECs based on polymer electrodes, because some polymer materials not only are generally cheap and light and have suitable morphology and fast doping-undoping process but also can be relatively easily manufactured into ECs. There are many organic materials such as polypyrrole, polyaniline, polythiophene, and its derivatives for redox capacitors as shown in Scheme 1. These organic molecules can be operated in nonaqueous or aqueous electrolytes. It has been reported that polyaniline (Scheme 1b) [6], poly-3-methylthiophene (Scheme 1d) [7], and polyfluorophenylthiophene (Scheme 1g) [8] can be operated in a nonaqueous electrolyte, such as propylene carbonate containing tetraethylammonium tetrafluoroborate. Among them, poly-1,5-diaminoanthraquinone (Scheme 1j) [9] shows a high specific capacitance of 200–300 Fg^{-1} but only in an acidic aqueous electrolyte. Generally, conducting polymers do not have very good cycleability and capacity retention because swelling and shrinking of electroactive polymers lead to degradation during cycling.

To improve cycleability, many researchers proposed composite electrodes and new organic materials. The polymer modified by conductive materials such as carbon materials has been proposed. For example, Xia et al. presented a poly(2,2,6,6,-tetramethylpiperidinyloxy methacrylate)nitroxide polyradical/activated carbon composite as a negative electrode material [10]. The capacity of the composite electrode was 30 % larger than that of the pure activated carbon electrode. This composite electrode could be operated for over 1,000 cycles with only slight capacity loss. For another material, the network of cyclic indole trimer (CIT) is one of the most durable organic for ECs. Naoi et al. reported that the CIT electrode showed electrochemical redox activity and excellent cycleability in an aqueous H_2SO_4 electrolyte [11] as well as a nonaqueous electrolyte of $LiBF_4$ dissolved in EC + DMC [12]. In the aqueous system, the CIT electrode maintained its high capacity of 52 Ah kg^{-1} (187 F g^{-1}) after 100,000 cycling, while the capacity decreased down to 5 Ah kg^{-1} for a polyindole electrode. In the case of above nonaqueous electrolyte system, CIT maintained 70 % (55 Ah kg^{-1}) of its initial capacity after 50,000 cycles (Scheme 1).

Electric energy can be stored and delivered in conducting polymers as delocalized π-electrons are accepted and released during electrochemical doping-undoping, respectively. There are two types of doping process as follows:

$$\text{p-doping (anion doping)}$$
$$[\text{polymer}] + \text{xA}^- \leftrightarrow [(\text{polymer})\text{x}^+\text{xA}^-] + \text{xe}^-$$
$$\text{n-doping (cation doping)}$$
$$[\text{polymer}] + \text{yC}^+ + \text{ye}^- \leftrightarrow [(\text{polymer})\text{y}^-\text{yC}^+]$$

Conducting polymer ECs are classified into three types (Fig. 1). Type I capacitors utilize p-doping conducting polymers such as polypyrrole, polythiophene, and polyaniline for both positive and negative electrodes. The type I capacitors show low potential (< 1V), and only half of the total capacity can be utilized. In the type II capacitors, two different p-dope polymers are used and have different potential ranges of doping and undoing. The proton polymer battery is a practical application of this type. The type II capacitors provide higher capacity and higher working voltage than type I system. Type III devices utilize p- and n-doping conducting polymers such as polythiophene derivatives and polyacene, for both positive and negative electrodes, respectively. Type III capacitors can provide the widest operating voltage (2.5–3.0V), which is about two times higher than type II, and the highest energy density among these three types. The type III capacitors have similar discharge characteristics to batteries, where operating voltage drops very rapidly at the end of discharge.

Transition Metal Oxides

Transition metal oxides for ECs can generally provide higher energy density than conventional

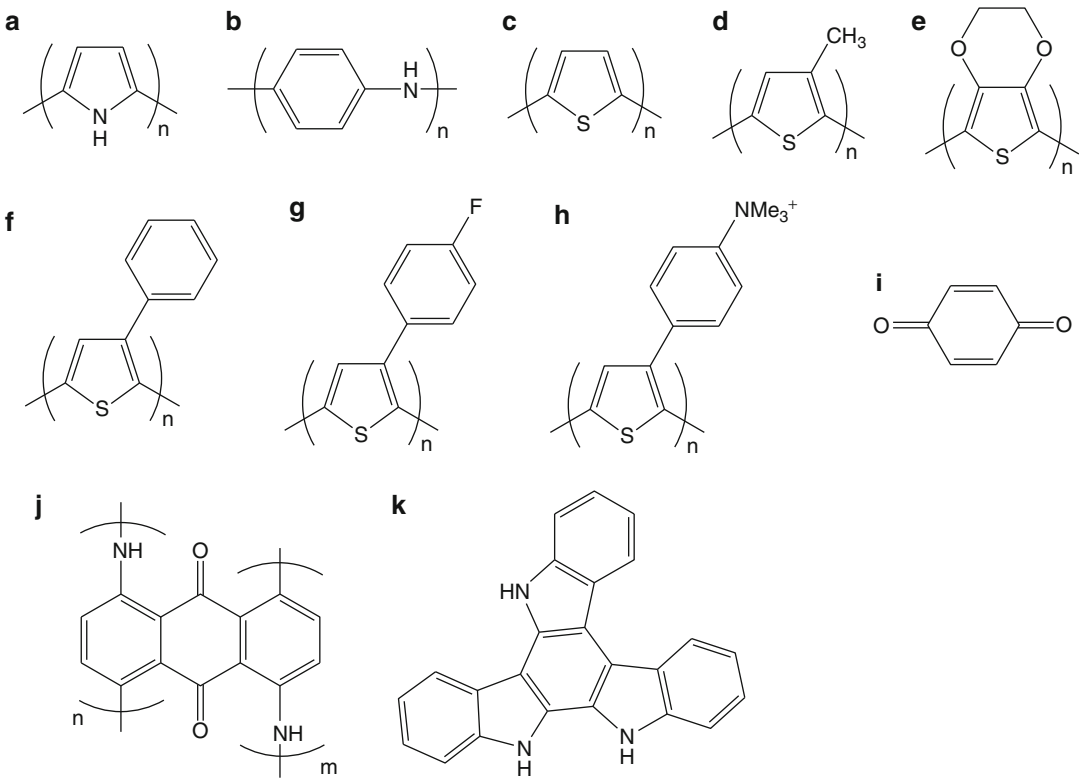

Redox Capacitor, Scheme 1 Organic materials for ECs include polypyrrole (**a**), polyaniline (**b**), polythiophene, its derivatives (**c**)–(**h**), *p*-benzoquinone (**i**), poly-1,5-diaminoanthraquinone (**j**), and cyclic indole trimer (**k**)

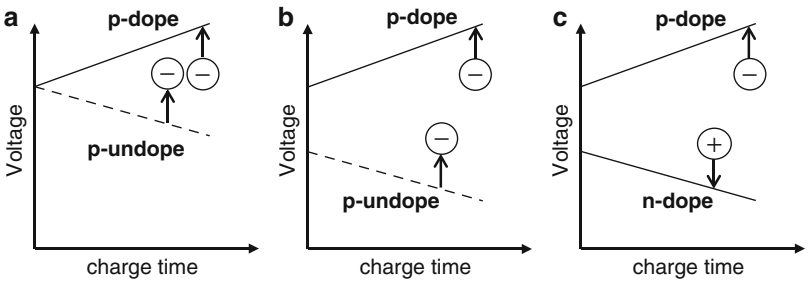

Redox Capacitor, Fig. 1 Classification of ECs utilizing conducting polymer materials, type I (**a**), type II (**b**), and type III (**c**)

carbon materials and better electrochemical stability than polymer materials. Among transition metal oxides, hydrous ruthenium oxide is the most promising electrode material because of its high theoretical specific capacitance (900–1,400 F g^{-1}) [13–17] depending on the hydration number, high conductivity, long cycle life, and good electrochemical reversibility as well as its high-rate capability. In 1995, Zheng et al. [13] reported that amorphous hydrous RuO_2 prepared by a sol–gel method exhibited a specific capacitance of 720 F g^{-1}. Such a high capacitance is attributed to hydrous surface layers that enable facile transport of electrons and protons. However, the capacitance decreased rapidly at high rates due to proton depletion and oversaturation in the electrolyte during charge–discharge cycling. A two-dimensionally

controlled RuO_2 nanosheet was fabricated by Sugimoto et al. [18] for better electron transport. Moreover, in order to improve the rate capability, many researchers have attempted to prepare nano-sized particles of hydrous RuO_2 with carbon materials such as activated carbons [14–16, 19], carbon black [17, 20–22], and CNTs [23]. For example, Hu et al. [16] reported that nano-sized (3 nm) hydrous RuO_2/carbon composites exhibited high specific capacitance of 800–1,200 F g^{-1} (per RuO_2). Moreover, Naoi et al. [22] reported that a superhighly dispersed nano-sized (0.5–2.0 nm) hydrous RuO_2/ketjen black composite could be prepared by an in situ sol–gel process induced by ultracentrifugal mechanical agitation. After annealing at 150 °C, the composite showed a high specific capacitance of 821 F g^{-1} (per composite).

The scarcity and cost of the precious metals are major disadvantages for massive devices of ECs. Due to cost consideration, RuO_2, MnO_2 [24], CoOx [25], VOx [26], Fe_3O_4 [27, 28], Ni $(OH)_2$ [29], WC [30], and Mo_2C [30] have been studied as alternative materials. The research efforts have focused on compounds providing high-rate capability and capacitance.

Manganese oxides, characterized by low cost, abundance, and environmental compatibility, serve as a low cost replacement for precious metals. The first study reporting the capacitive behavior of manganese dioxide was published in 1999 by Lee and Goodenough [24]. This was followed by many studies that dealt with the pseudocapacitive properties of manganese dioxide materials prepared by dip coating, electrodeposition, etc. The capacitive properties of manganese oxides are sensitive to morphologies, crystal structures, cation valence, and defect chemistry. The relationship between the crystallographic structures and their pseudocapacitive properties has been investigated exhaustively by Brousse et al. [31] and Devaraj and Munichandraiah [32]. These and other groups reported that birnessite-type manganese oxides could provide the highest capacitance [33, 34].

Several groups have reported that MnO_2 is formed as an ultrathin film on a planar current collector, and anomalously high gravimetric capacitances can be observed [35, 36]. The implication of this finding has been translated to 3-dimensional electrode designs in which nanoscopic MnO_2 deposits are incorporated directly onto surface nanostructured carbon such as carbon nanotubes [36–39], templated mesoporous carbons [40], and carbon aerogel/nanoforms [41]. Such materials on the nanostructured carbon substrates serve a high specific surface area on a three-dimensional current collector, which facilitates the infiltration and rapid transport of an electrolyte into the nanoscopic MnO_2 phase (Table 1).

Redox Capacitor, Table 1 Summary of the various classes of transition metal oxides

Electrode material	Electrolyte	Working voltage (V)	Capacitance (F g^{-1})	References
$RuO_2 \cdot nH_2O$ powder	H_2SO_4	1.0	720 (n = 0.5)	[13]
$RuO_2 \cdot nH_2O$/activated carbon	H_2SO_4	1.0	720	[14]
Ruthenic acid nanosheet	H_2SO_4	1.0	658	[18]
$RuO_2 \cdot nH_2O$/activated carbon	H_2SO_4	1.0	1,200	[16]
$RuO_2 \cdot nH_2O$/ketjen black	H_2SO_4	0.8	821	[22]
$CoOx \cdot nH_2O$	NaOH	0.7	230	[25]
$VOx \cdot nH_2O$	KCl	1.0	167	[26]
Nanoporous $Ni(OH)_2$ film	KOH	0.65	578	[29]
Mn_3O_4	Na_2SO_4 adding Na_2HPO_4	1.0	230	[33]
MnO_2 thin film	Na_2SO_4	0.9	698	[35]
MnO_2/CNT/carbon paper	K_2SO_4	1.0	322	[36]
$\alpha MnO_2 \cdot nH_2O$/CNT	Na_2SO_4	0.6	277	[38]
MnO_2/mesoporous carbon	KCl	1.0	600	[40]

Novel Concept for Charge Storage Mechanism Involving "Electrolyte"

Recently, novel striking redox capacitors utilizing an electrolyte charge storage system have been attempted by few researchers [42–45]. Before them, such a system had been considered impossible for an electrochemical capacitor because of an incidental shuttle reaction or charge migration of active redox species in an electrolyte between electrodes. In 2007, Ishikawa et al. reported that EC containing an aqueous NaBr solution with a potentiostatic treatment at 70 °C exhibits much enhanced capacitance when compared to EC without the treatment [46]. In their later study, the mechanism of enhanced capacitance was found to be based on some redox processes involving bromine species (iodine species is also possible) in the electrolyte. This mechanism provides the reversible cycling of ECs, which can be stabilized especially by a pretreatment of an activated carbon electrode with bromine species. Utilizing this strategy, Yamazaki and Ishikawa et al. attained excellent capacitance and a high practical cell voltage of 1.8 V in spite of an aqueous electrolyte system (Fig. 2a and b).

Furthermore, the aqueous EC utilizing the bromide system shows outstanding performance (Fig. 3); its energy density at a low power density corresponding to a current density of 100 mA g^{-1} is about 1.2 times higher than a 2.7V class nonaqueous EC [triethylmethylammonium tetrafluoroborate ($TEMABF_4$) dissolved in propylene carbonate (PC)] in spite of an aqueous EC system. Moreover, the EC system has not only higher energy density but also much higher power density than the reference nonaqueous EC because of its high ionic conductivity (Fig. 3).

To achieve higher energy density and higher voltage operation than aqueous ECs utilizing the bromide system, nonaqueous electrolyte systems have also been proposed such as an ionic liquid electrolyte-based EC system [47] and lithium-ion capacitor system [48].

Future Advanced Developments for Redox Capacitors

Despite high capacitance of redox materials such as transition metal oxide, the cell voltage of conventional symmetric devices as introduced in the above chapter is limited to ~1V, and subsequently both power and energy densities remain unsatisfactory for industrial applications. Recently, therefore, asymmetric design often called a hybrid capacitor and nonaqueous EC system with the above materials such as polymer materials and transition metal oxides have been studied. The term "asymmetric design" means a capacitor using different materials with different operating potentials as negative and positive electrode materials, which can increase overall cell potential, resulting in enhanced energy and

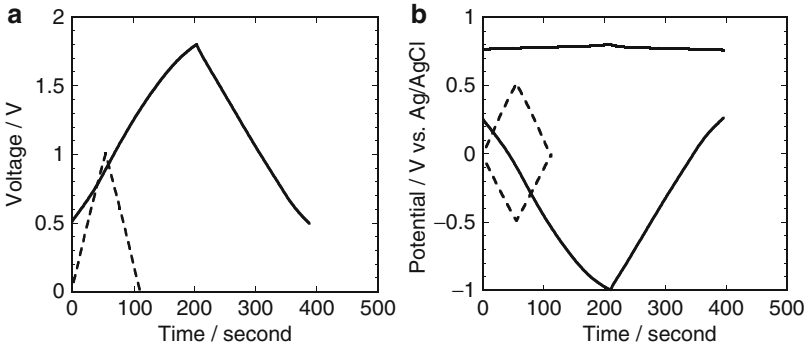

Redox Capacitor, Fig. 2 Voltage or potential vs. time curves during galvanostatic cycles of the EC cell utilizing bromide redox system (———) and the reference EC cell (– – –) containing an aqueous 3.5 mol dm^{-3} NaBr electrolyte at 1,000 mA g^{-1}; (**a**) voltage between positive and negative electrodes, (**b**) potential of negative and positive electrodes versus Ag/AgCl reference

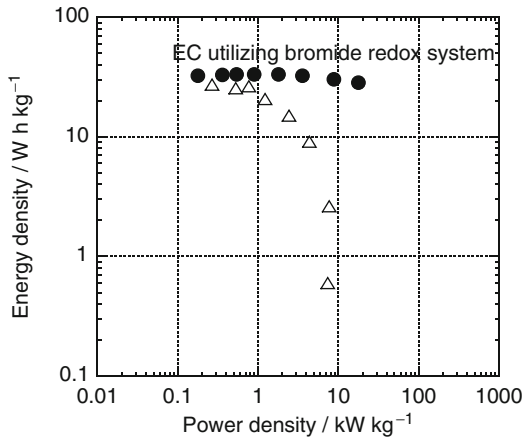

Redox Capacitor, Fig. 3 Ragone plots (relationship between energy density and power density) for the EC cell utilizing bromide redox reactions in the aqueous 3.5 mol dm^{-3} NaBr electrolyte (●) and the conventional nonaqueous EC containing 1.96 mol dm^{-3} $TEMABF_4$/PC(△)

power densities. Asymmetric hybrid capacitors include various combinations of positive and negative electrode materials: metal oxide/metal oxide [27], conducting polymer/metal oxide [49], metal oxide/carbon [50, 51], and conducting polymer/carbon materials [52].

Cross-References

- ▶ Electrical Double-Layer Capacitors (EDLC)
- ▶ Hybrid Li-Ion Based Supercapacitor Systems in Organic Media
- ▶ Lithium-Ion Batteries

References

1. Miller JR, Burke AF (2008) Electrochemical capacitors: challenges and opportunities for real-world applications. ECS Interface 17:53–57
2. Conway BE (1999) Electrochemical supercapacitors: scientific fundamentals and technological applications. Kluwer Academic/Plenum, New York
3. Miller JR, Simon P (2008) Electrochemical capacitors for energy management. Science 321:651–652
4. Beguin F, Frackowiak E (2009) Carbons for electrochemical energy storage and conversion systems. CRC Press, Boca Raton
5. Barbieri O, Hahn M, Herzog A, Kotz R (2005) Capacitance limits of high surface area activated carbons for double layer capacitors. Carbon 43:1303–1310
6. Prasad KR, Munichandraiah N (2002) Electrochemical studies of polyaniline in a gel polymer electrolyte. Electrochem Solid-State Lett 5:A271–A274
7. Mastragostino M, Paraventi R, Zanelli A (2000) Supercapacitors based on composite polymer electrodes. J Electrochem Soc 147:3167–3170
8. Villers D, Jobin D, Soucy C, Cossement D, Chahine R, Breau L, Belanger D (2003) The influence of the range of electroactivity and capacitance of conducting polymers on the performance of carbon conducting polymer hybrid supercapacitor. J Electrochem Soc 150:A747–A752
9. Hashmi SA, Suematsu S, Naoi K (2004) All solid-state redox supercapacitors based on supramolecular 1,5-diaminoanthraquinone oligomeric electrode and polymeric electrolytes. J Power Sources 137:145–151
10. Li H, Zou Y, Xia Y (2007) A study of nitroxide polyradical/activated carbon composite as the positive electrode material for electrochemical hybrid capacitor. Electrochim Acta 52:2153–2157
11. Machida K, Takenouchi H, Hiraki R, Naoi K (2005) Redox capacitor properties of indole derivatives-electrochemical characteristics and long-term cycleability of cyclic indole trimer. Electrochemistry 73:489–495
12. Machida K, Nakagawa Y, Ogihara N, Naoi K (2005) Redox capacitor properties of indole derivatives III-electrochemical characteristics of 5-carboxy cyclic indole trimers in non-aqueous electrolyte. Electrochemistry 73:1035–1041
13. Zheng J-P, Cygan P-J, Jow T-R (1995) Hydrous ruthenium oxide as an electrode material for electrochemical capacitors. J Electrochem Soc 142:2699–2703
14. Zheng J-P (1999) Ruthenium oxide-carbon composite electrodes for electrochemical capacitors. Electrochem Solid-State Lett 2:359–361
15. Ramani M, Haran BS, White RE, Popov BN, Arsov L (2001) Studies on activated carbon capacitor materials loaded with different amounts of ruthenium oxide. J Power Sources 93:209–214
16. Hu C-C, Chen W-C, Chang K-H (2004) How to achieve maximum utilization of hydrous ruthenium oxide for supercapacitors. J Electrochem Soc 151:A281–A290
17. Lee Y-H, Oh J-G, Oh H-S, Kim H (2008) Novel method for the preparation of carbon supported nano-sized amorphous ruthenium oxides for super capacitors. Electrochem Commun 10:1035–1037
18. Sugimoto W, Iwata H, Yasunaga Y, Murakami Y, Takasu Y (2003) Preparation of ruthenic acid nanosheets and utilization of its interlayer surface for electrochemical energy storage. Angew Chem Int Ed Engl 42:4092–4096
19. Zhang J, Jiang D, Chen B, Zhu J, Jiang L, Fang H (2001) Preparation and electrochemistry of hydrous ruthenium oxide/active carbon electrode materials for supercapacitor. J Electrochem Soc 148: A1362–A1367
20. Kim H, Popov BN (2002) Characterization of hydrous ruthenium oxide/carbon nanocomposite

supercapacitors prepared by a colloidal method. J Power Sources 104:52–61
21. Min M, Machida K, Jang J-H, Naoi K (2006) Hydrous RuO_2/carbon black nanocomposite with 3D porous structure by novel incipient wetness method for supercapacitors. J Electrochem Soc 153:A334–A338
22. Naoi K, Ishimoto S, Ogihara N, Nakagawa Y, Hatta S (2009) Encapsulation of nanodot ruthenium oxide into KB for electrochemical capacitors. J Electrochem Soc 156:A52–A59
23. Park J-H, Ko J-M, Park O-O (2003) Carbon nanotube/RuO_2 nanocomposite electrodes for supercapacitors. J Electrochem Soc 150:A864–A867
24. Lee H-Y, Goodenough J-B (1999) Supercapacitor behavior with KCl electrolyte. J Solid State Chem 144:220–223
25. Hu C-C, Hsu T-Y (2008) Effects of complex agents on the anodic deposition and electrochemical characteristics of cobalt oxides. Electrochim Acta 53:2386–2395
26. Hu C-C, Huang C-M, Chang K-H (2008) Anodic deposition of porous vanadium oxide network with high power characteristics for pseudocapacitors. J Power Sources 185:1594–1597
27. Brousse T, Belanger D (2003) A hybrid Fe_3O_4-MnO_2 Capacitor in mild aqueous electrolyte. Electrochem Solid-State Lett 6:A244–A248
28. Wang S-Y, Wu N-L (2003) Operating characteristics of aqueous magnetite electrochemical capacitors. J Appl Electrochem 33:345–348
29. Zhao D-D, Bao S-J, Zhou W-J, Li H-L (2007) Preparation of hexagonal nanoporous nickel hydroxide film and its application for electrochemical capacitor. Electrochem Commun 9:867–874
30. Morishita T, Soneda Y, Hatori H, Inagaki M (2007) Carbon-coated tungsten and molybdenum carbides for electrode of electrochemical capacitor. Electrochim Acta 52:2478–2484
31. Brousse T, Toupin M, Dugas R, Athouel L, Crosnier O, Belanger D (2006) Crystalline MnO_2 as possible alternatives to amorphous compounds in electrochemical supercapacitors. J Electrochem Soc 153:A2171–A2180
32. Devaraj S, Munichandraiah N (2008) Effect of crystallographic structure of MnO_2 on its electrochemical capacitance properties. J Phys Chem C 112:4406–4417
33. Komaba S, Ogata A, Tsuchikawa T (2008) Enhanced supercapacitive behaviors of birnessite. Electrochem Commun 10:1435–1437
34. Inoue R, Nakayama M (2009) Pseudocapacitive properties of vertically aligned multilayered manganese oxide. Electrochem Solid-State Lett 12:A203–A206
35. Pang S-C, Anderson MA, Chapman TW (2000) Novel electrode materials for thin-film ultracapacitors: comparison of electrochemical properties of sol–gel-derived and electrodeposited manganese dioxide. J Electrochem Soc 147:444–450
36. Bordjiba T, Belanger D (2009) Direct redox deposition of manganese oxide on multiscaled carbon nanotube/microfiber carbon electrode for electrochemical capacitor. J Electrochm Soc 156:A378–A384
37. Hu C-C, Wu Y-T (2004) Effects of electrochemical activation and multiwall carbon nanotubes on the capacitive characteristics of thick MnO_2 deposits. J Electrochm Soc 151:A2060–A2066
38. Raymundo-Pinero E, Khomenko V, Frackwiak E, Beguin F (2005) Performance of manganese oxide/CNTs composites as electrode materials for electrochemical capacitors. J Electrochm Soc 152: A229–A235
39. Xie X, Gao L (2007) Characterization of a manganese dioxide/carbon nanotube composite fabricated using an in situ coating method. Carbon 45:2365–2373
40. Dong X, Shen W, Gu J, Xiong L, Zhu Y, Li H, Shi J (2006) MnO_2-embedded-in-mesoporous-carbon-wall structure for use as electrochemical capacitors. J Phys Chem B 110:6015–6019
41. Fischer AE, Pettigrew KA, Rolison DR, Stround RM, Long JW (2007) Incorporation of homogeneous carbon structures via self-limiting electroless deposition: implications for electrochemical capacitors. Nano Lett 7:281–286
42. Naitou M, Yamazaki S, Yamagata M, Ishikawa M (2008) Effects of bromide ion for electric double layer capacitors. In: The third Asian conference on electrochemical power sources (ACEPS-3) Abstract Pc-03, p.291, Soul
43. Lota G, Frackowiak E (2008) Striking capacitance of carbon/iodide interface. Electrochem Commun 11:87–90
44. Yamazaki S, Ito T, Yamagata M, Ishikawa M (2010) Performance of electrochemical capacitor utilizing bromide ion as redox species. In: 218th Electrochem. Soc. Meeting abstract #312, Las Vegas; Yamazaki S, Ito T, Murakumo Y, Naitou M, Shimooka T, Yamagata M, Ishikawa M, J Electrochem Soc (in contribution)
45. Lota G, Fic K, Frackwiak E (2011) Alkali metal iodide/carbon interface as a source of pseudocapacitance. Electrochem Commun 12:38–41
46. Shimooka T, Yamazaki S, Sugimoto T, Jyozuka T, Teraishi H, Nagao Y, Oda H, Matsuda Y, Ishikawa M (2007) Capacitance enhancement of aqueous EDLC Systems by electrochemical treatment. Electrochemistry 75:273–279
47. Yamazaki S, Ito T, Yamagata M, Ishikawa M, Non-aqueous electrochemical capacitor utilizing electrolytic redox reactions of bromide species in ionic liquid. Electrochim Acta (in press)
48. Ishikawa M, Yamazaki S, Yamagata M (2011) Novel designs of electrode-electrolyte interface for supercapacitors. In: 2nd International symposium on enhanced electrochemical capacitors (ISEECap'11) abstract p. 30, Poznan
49. Pasquier AD, Laforgue A, Simon P, Amatucci GG, Fauvarque J-F (2002) A novel asymmetric hybrid

$Li_4Ti_5O_{12}$/poly(fluorophenylthiophene) energy storage device. J Electrochem Soc 149:A302–A306
50. Brousse T, Marchand R, Taberna P-L, Simon P (2006) TiO_2(B)/activated carbon non-aqueous hybrid system for energy storage. J Power Sources 158:571–577
51. Demarconny L, Raymundo-Pinero E, Beguin F (2011) Adjustment of electrodes potential window in an asymmetric carbon/MnO_2 supercapacitor. J Power Sources 196:580–586
52. Balducci A, Henderson WA, Mastragostino M, Passerini S, Simon P, Soavi F (2005) Cycling stability of a hybrid activated carbon/poly(3-methylthiophene) supercapacitor with *N*-butyl-*N*-methylpyrrolidinium bis(trifluoromethanesulfonyl)imide ionic liquid as electrolyte. Electrochim Acta 50:2233–2237

Redox Processes at Semiconductors-Gerischer Model and Beyond

Frank Willig[1] and Lars Gundlach[2]
[1]Fritz-Haber-Institut der Max-Planck-Gesellschaft, Berlin, Germany
[2]Department of Chemistry and Biochemistry and Department of Physics and Astronomy, University of Delaware, Newark, DE, USA

Introduction

In this article we describe ideas and experimental results that are fundamental to electron transfer between molecules (redox ions) and the surface of semiconductor (SC) electrodes. We do not make any attempt here of covering the extensive literature on electrochemistry at semiconductor electrodes. Rather, experimental data are shown to illustrate relevant results. We consider only the transfer of one electron between a molecular monomer (redox ion) and the electrode. We do not consider electron transfer from dimers and higher aggregates and also not the more complicated processes like corrosion, etching, and tunneling through barriers. In the case of ultrafast injection from an excited dye molecule, we show results where the system is exposed to ultrahigh vacuum since the solvent environment would obscure the most interesting results obtained from time-resolved measurements of electron transfer. The effects arising from the addition of a solvent environment are mentioned.

Electron Transfer Between a SC Electrode and Redox Ions (Molecules) in Solution

The free energy of charge carriers in the semiconductor electrode (SC) is characterized by the Fermi energy and that of the charge exchanging molecules (redox ions) in solution by their redox potential. When the two subsystems are brought into contact with their free energy levels not too far apart, the two subsystems will exchange charges until a common electrochemical potential is established throughout the whole system [1] (Fig. 1).

The corresponding equilibrium situation is established via setting up a space-charge region with a corresponding band bending in the near-surface region of the semiconductor. Figure 2 illustrates the band bending for the lower edge of the conduction band and the upper edge of the valence band versus distance. Note that the applied potential (η) drops over the space-charge layer in the semiconductor and only a negligible fraction of the voltage drop occurs at the electrode surface. Thus, the rate constant of electron transfer remains virtually unchanged at the surface of the semiconductor when the applied voltage is changed. This is very different from a metal electrode. The arrow in Fig. 2 indicates the reduction in the electron concentration at the surface due to applied voltage because the latter enhances the barrier height for electrons moving from the bulk of the semiconductor to the surface.

Gerischer [1, 3] postulates a density of states function in the form of a Gaussian distribution for the reduced species in solution and a corresponding Gaussian distribution shifted toward the vacuum level for the oxidized species. The two distributions are labeled occupied and unoccupied in Fig. 1. Solvent configurations with the highest probability give rise to the two peaks, and the Gaussian distribution arises from different solvent configurations formed around the

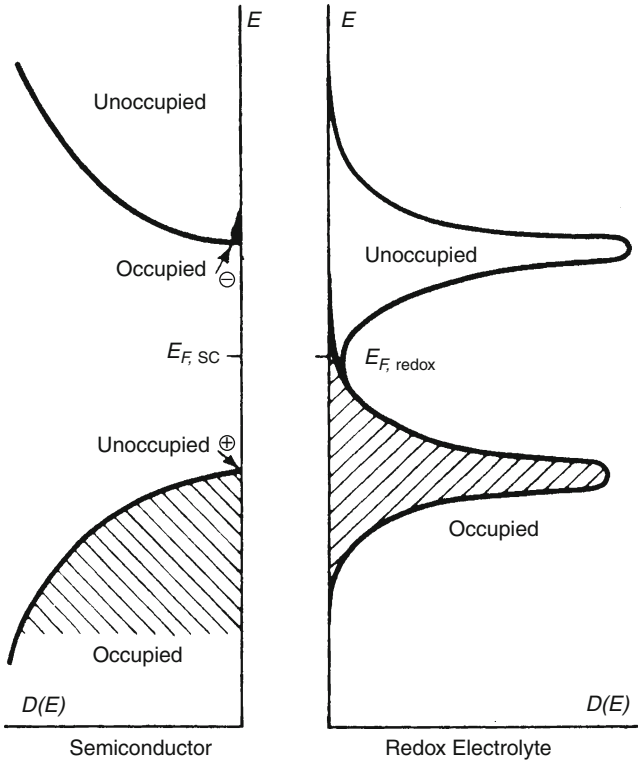

Redox Processes at Semiconductors-Gerischer Model and Beyond, Fig. 1 Scheme illustrating equilibrium between a semiconductor electrode and a redox electrolyte. The density of states D(E) in the valence band and conduction band on the left (labeled occupied and unoccupied, respectively) and one Gaussians each for the density of states D(E) of the reduced redox ions and the oxidized redox ions on the right (labeled occupied and unoccupied, respectively). The free energy is the same throughout the system, with the Fermi energy $E_{F,SC}$ at the same energy as the redox potential $E_{F,\,redox}$ (Reproduced from Fig. 23, Ref. [1])

reduced and the oxidized redox ions, respectively. The two peaks and the corresponding distributions for reduced and oxidized redox ions are shifted against each other on the energy axis due to the fact that the system has a slow and a fast polarization response to a sudden change in the charge of the redox ion. The polarization response of the electronic subsystem to a change in the charge is fast, instantaneous for the time scales considered here, and the polarization response from the change in the spatial coordinates of the solvent molecules is slow to a sudden change in the charge on the redox ion. Removing an electron from the reduced redox ion has to overcome the attraction of a more positively charged environment than is present when the electron is returned to the oxidized redox ion after the slow polarization response is already completed and the system is completely relaxed. Completing the slow polarization response after removal of the electron means that the effective positive charge in the environment has decreased around the now oxidized redox ion that carries less negative charge than the reduced redox ion. Thus, less energy is gained from the return of the electron to the oxidized redox ion after the environment has relaxed in response to the lowered negative charge than had to be spent in separating the electron from the reduced redox ion where the environment forms a higher positive charge around the redox ion with a higher negative charge, i.e., the reduced redox ion. Marcus [4] has presented a quantitative measure for the change in polarization energy for a system where the redox ions are conducting spheres carrying a different charge and the environment is a dielectric medium with two different dielectric constants, one for the fast response and the other for the slow response. Other authors (e.g., [5]) have added an additional slow polarization energy that arises from a change in the equilibrium coordinates of the atoms making up the molecule (redox ion) when the charge is changed on the molecule. The polarization energy has thus an outer (solvent) and an inner (atoms of the molecule) contribution. Classical Marcus theory

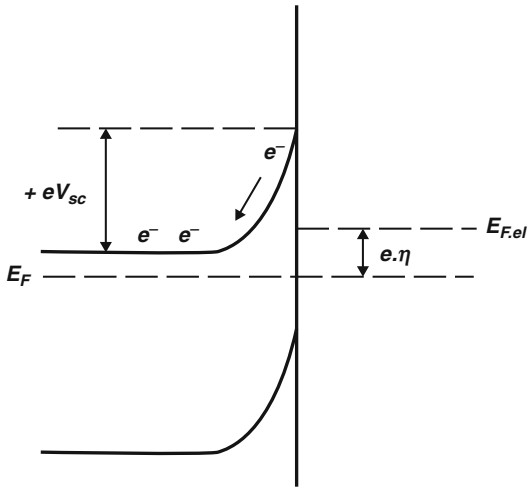

Redox Processes at Semiconductors-Gerischer Model and Beyond, Fig. 2 Band bending due to the space-charge layer near the surface of the semiconductor. The ordinate is energy and the abscissa distance. The Fermi level (E_F) is downshifted against the redox potential ($E_{F,el}$) by the applied potential η (multiplied by the elementary charge e). The SC is n-doped (Fermi level lies close to the conduction band edge in the bulk). The applied potential enhances the barrier for electrons moving from the bulk of the semiconductor to the surface and thus reduces the electron concentration at the surface (2) (Reproduced from Fig. 2.4, Ref. [2])

of the rate constant of electron transfer of a redox ion in a polarizable medium [4] predicts also a Gaussian energy dependence of the rate constant. As long as the rate constant of electron transfer is described with the tools of only classical physics assuming a fast and a slow polarization response, the predictions of classical Marcus theory for the rate constant of electron transfer are identical with those derived from the assumption of a density of states for the redox ions in the form of two Gaussian energy distributions, one for the reduced and the other for the oxidized species as illustrated in Fig. 1. The peaks of the two distributions are separated on the energy axis in Fig 1 by twice the amount of the above polarization energy. Classical Marcus theory of electron transfer and the Gerischer scenario (Fig. 1) both fail when quantum effects become important. The latter arises in the dynamics of electron transfer when strong coupling between the electronic states and high-energy vibrational modes in the molecules (redox ions) are incorporated into the model [5, 6]. This strong coupling is a common feature of different classes of molecules and redox ions [7–9]. The additional qualitative effect arising from high-energy (quantum) vibrational modes in the molecule (redox ion) is faster electron transfer compared to the classical model when electron transfer occurs to a low-lying acceptor, i.e., electron transfer becomes faster in the downhill high-energy wing of the energy distribution than is predicted by the classical calculation of the rate constant, means the shape deviates here from a Gaussian. Such quantum effects are automatic ingredients if quantum theory is employed for calculating rates of electron transfer [5, 6]. For a long period of time, quantum theory was used in the form of perturbation theory, where the maximum permissible strength of electronic interaction had an upper limit and thus the electron transfer time had a lower limit. Recently, fully quantum mechanical calculations of electron transfer have been presented without the restrictions of perturbation theory that can address ultrafast electron transfer at semiconductor electrodes, as will be described below. Experimental results will be shown below where the peak of the distribution curves shown in Fig. 1 corresponds to electron transfer in the range of a few femtoseconds. Conventional experimental measurements in electrochemistry can only access the time window of nanoseconds, at the most picoseconds. The corresponding rate constants correspond to the tails of the distribution curves, many order of magnitude smaller than at the peak. Rate constants in the wings can be visualized if a logarithmic plot of the rate constant versus energy is used instead of the linear plot shown in Fig. 1. In the wings the rate constants decrease about exponentially with increasing energy difference. Therefore, the energy range with sufficient overlap between electronic donor and acceptor states making a significant contribution to charge exchange across the interface is usually comprising only an energy interval twice the mean thermal energy ($2k_BT$ with T = temperature and k_B = Boltzmann's constant) above the respective band edge of the semiconductor.

A systematic variation in the type of redox ion and measurements of the corresponding exchange currents have been performed at metal electrodes [10] and at insulator electrodes, where charge can be injected by redox ions only into the valence band [11]. Electron transfer reactions at semiconductor/liquid interfaces were studied by the Marcus group with a Fermi golden rule approach [12, 13] and agreed reasonable well with experimental results by the Lewis group [14, 15]. Such data displays considerable uncertainty in the value of the reorganization energy for a specific redox ion even if the measurements were carried out in an identical ionic environment. Shifts in the redox energy at the electrode surface compared to the value measured against a reference electrode can also occur. Using such compiled data of the reorganization energies of redox ions, one can arrive at rough qualitative prediction concerning the value of the rate constant with a logarithmic plot instead of Fig. 1. Quantum effects arising in the downhill energy wing can make the prediction even less reliable. The uncertainty margin for the thus estimated rate constant should be expected in the range of a factor of 10–100. Depending on the type of measurement, the interfacial rate constant can be obtained with different dimensions, i.e., s^{-1}, cms^{-1}, cm^3s^{-1}, and cm^4s^{-1}. Making plausible assumptions about the reaction distance and reaction volume such values can be converted with an uncertainty margin.

Photocurrent Transient Due to Light Absorption in the Bulk of the SC and Interfacial Electron Transfer

The photocurrent due to the photo-generation of minority carriers is controlled by the discharge of the minority carriers from the surface of the electrode into the electrolyte and by competing recombination reactions of the minority charge carriers with the majority charge carriers. Of course, there are also competing side reactions of the minority carriers at the crystal surface, e.g., those leading to the corrosion of the electrode surface. Several attempts can be found in the literature of obtaining the rate constant of interfacial electron transfer in the SC/redox electrolyte system from the time-resolved photocurrent response to optical bulk excitation of the SC electrode. This is not possible, however, since the photocurrent transient contains the influence of electron transfer to the redox ions in the electrolyte only indirectly as a reaction channel competing with recombination between minority and majority carriers near the surface of the electrode. Figure 3 illustrates the different processes in the energy versus distance diagram along with an equivalent circuit augmented by two current sources where the relevant physical processes can be introduced in the form of appropriate equations describing transport and reactions of the charge carriers [16]. Superimposed on the actual dynamics is the response of the system to a change in voltage arising from the passive elements like capacitors and resistors in the circuit as illustrated on top of Fig. 3.

The electrical photo response to excitation with a weak laser pulse of 10 ps duration absorbed in the bulk of Si is measured as time-dependent voltage drop across the external resistor R_M. If the time elapsed after the laser pulse is short compared to the RC constant of the circuit, the measured signal can be interpreted as photovoltage. It can be interpreted as photocurrent if the elapsed time is long compared to the RC constant. Figure 4 shows the response of an n-Si electrode in the ns time window to the absorption of a laser pulse of 10 ps duration. The black shaded area in Fig. 3 illustrates the generation of electron–hole pairs by the incident light inside of the Si material.

The apparent instantaneous initial rise of the signal shown in Fig. 4 arises from the separation of photo-generated electron–hole pairs that are generated inside the depletion layer. The ensuing slower rise is the diffusional flux of screened minority carriers arriving from the bulk at the edge of the depletion layer, convoluted with the RC response of the circuit. At the edge of the depletion layer, the holes are separated from the screening charge. This process is described by

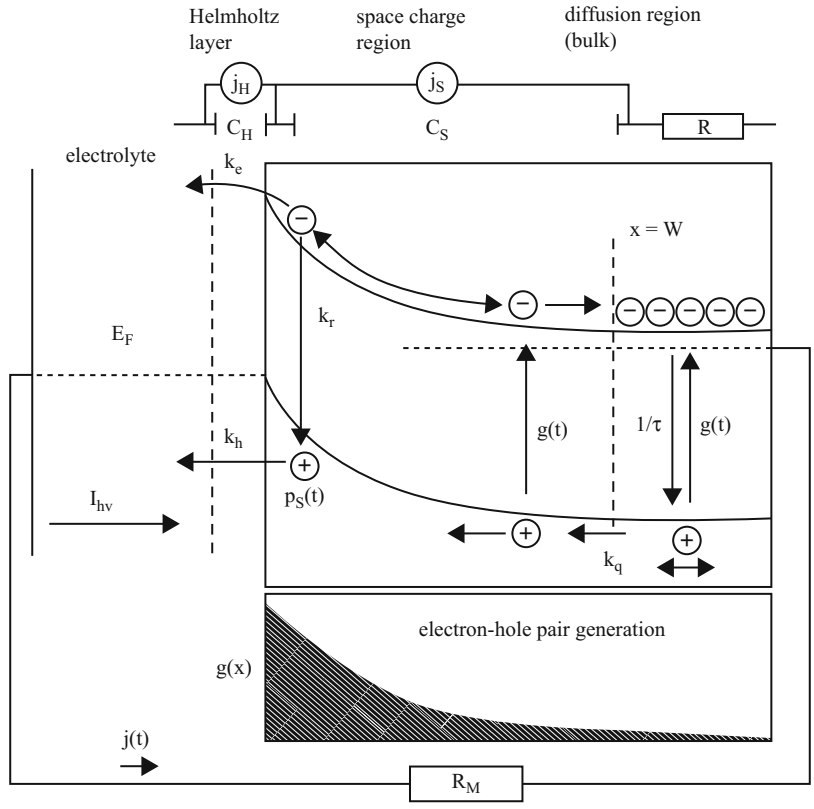

Redox Processes at Semiconductors-Gerischer Model and Beyond, Fig. 3 Light is impinging from the left and is absorbed in the SC electrode generating electron–hole pairs with function g(t). Holes are the minority carriers in the n-Si electrode. Screened minority carriers generated in the bulk (*right-hand side*) diffuse toward the depletion layer where they are separated from the screening charge (rate constant kq) and move from there to the electrode surface driven by the electric field of the depletion layer. The time-dependent concentration of holes at the electrode surface is $p_S(t)$. Bimolecular recombination of holes and electrons occurs with rate constant k_r. A reduced redox ion transfers an electron to the hole at the surface with rate constant k_h; an oxidized redox ion accepts an electron from the surface of the SC electrode with rate constant k_e. The simplest equivalent circuit with two current sources for the equations describing reactions and transport of charge carriers is shown on *top* of the diagram. The electric response is measured as time-dependent voltage across the external resistor R_M (Reproduced from Fig. 1, Ref. [16])

the phenomenological rate constant k_q. The signal is convoluted with the RC response, and the latter controls in particular the decay. The smooth solid curve is the total calculated response which includes the current sources describing transport and reactions of the charge carriers. The dashed curves are calculated with the current sources omitted. They represent the so-called RC response arising from the passive elements in the equivalent circuit shown on top of Fig. 3. The parameter in the inset is the band bending. Calculations have shown that the measured photovoltage is due to the displacement current flowing through the capacitor C_S formed by the depletion layer. The measured photovoltage is not sensitive to the faradaic current at the interface because the capacitor C_H is much larger than C_S making the contribution from the current source in C_H very small [16, 17]. Thus, the measured signal is not sensitive to interfacial electron transfer, specifically not to the rate constant k_h in Fig. 3 for electron transfer from reduced redox ions in solution to the holes at the surface of the n-Si electrode.

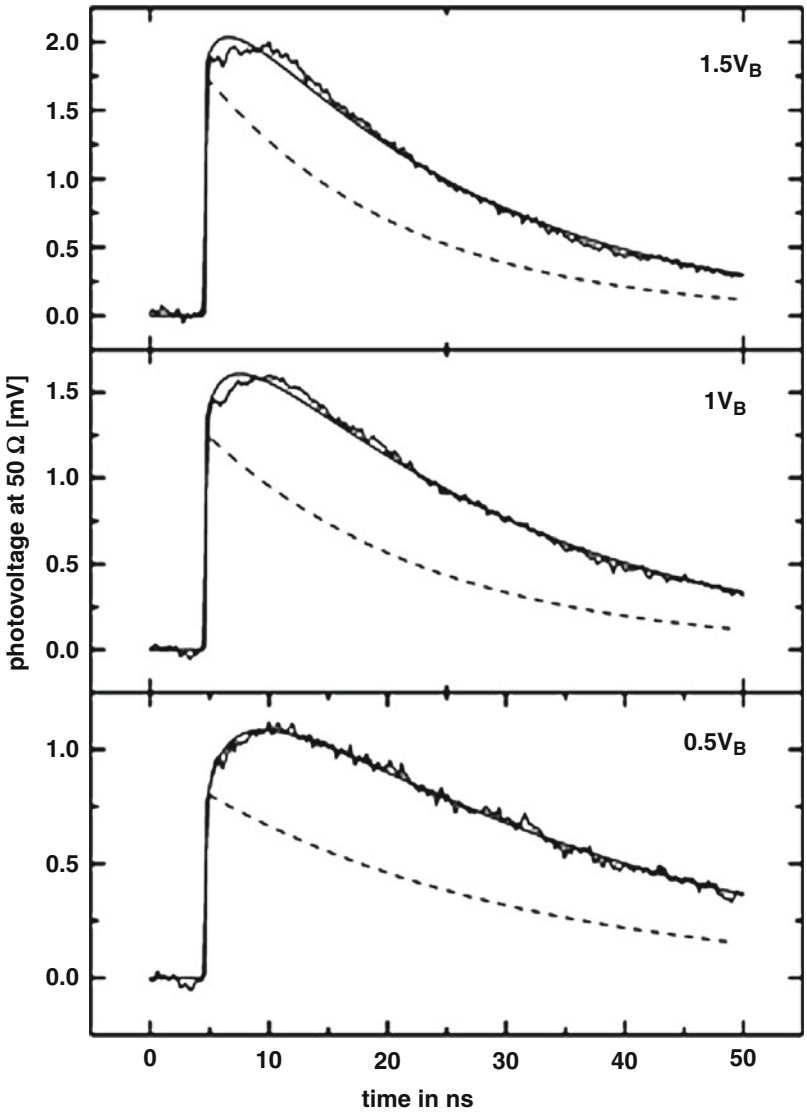

Redox Processes at Semiconductors-Gerischer Model and Beyond,
Fig. 4 Calculated and measured photovoltage across the external resistor R_M. A weak laser pulse (10^7 photons/mm^2) of 10 ps duration with 590 nm central wavelength impinged on the n-Si electrode. The thin curve is the calculated response including the current sources, whereas the dashed curve is the response without the current sources (so-called RC response). Time resolved is the diffusional flux of screened minority carriers arriving at the edge of the depletion layer convoluted with the RC response. Holes are separated from the screening charge and driven to the surface by the electric field in the depletion layer (Reproduced from Fig. 3, Ref. [16])

Recombination between the photo-generated holes (minority carriers) and electrons (majority carriers in the n-Si electrode) near the surface gives rise to a time-dependent dip in the photocurrent measured in response to a rectangular illumination of 1 ms duration (Fig. 5). The shape of the photocurrent signal in dependence on the bias voltage can be simulated by introducing a corresponding rate for bimolecular recombination between electrons and holes into the current source for the depletion layer (upper part of Fig. 3). Negative bias voltage lowers the band bending depicted in Fig. 3 and increases the dip, i.e., decreases the stationary photocurrent. The flat-band situation is reached at a bias of – 0.95 V as indicated by the disappearance of the initial photocurrent peak, labeled peak (filled squares in Fig. 5). Both the stationary photocurrent, labeled final (filled circles in Fig. 5), and the corresponding stationary recombination loss are linked to the stationary accumulation of holes at the interface. The stationary photocurrent disappears already at finite band bending of about 0.3 V with respect to the flat-band potential at – 0.95 V (Fig. 5).

The concentration of electrons in the depletion layer increases exponentially with the bias voltage going into negative direction. This leads to an increased recombination and a deeper dip in the photocurrent transient. Both the rate of electron transfer from the reduced redox ions to the holes at the electrode surface and the concentration of reduced redox ions must have an influence on the measured photocurrent of the holes since discharge into the electrolyte reduces the concentration of holes at the surface of the electrode and competes with recombination. A high concentration of the reduced redox ions combined with a reasonably high value of the rate constant k_h will keep the concentration of photo-generated holes fairly small at the surface of the n-Si electrode and thus reduce the recombination loss. On the other hand, the concentration of holes will increase at the surface if the concentration of the reduced redox ions is made very small slowing down discharge into the electrolyte. With a higher concentration of holes, there will be enhanced bimolecular recombination with the electrons. Bimolecular recombination of the holes with the electrons will dominate once a sufficient concentration of holes has accumulated at the surface. With only a slow discharge in the equations for the current source compared to bimolecular recombination, the photocurrent transient is predicted to develop an asymmetric shape with respect to switching on and off the illumination (Fig. 6). Moreover, the recombination dip should appear now as S-shaped time dependence of the initial photocurrent transient. Both features are very different when the photocurrent transient is measured in the presence of a high concentration of reduced redox ions with a fast discharge of the holes (Fig. 5). There is almost perfect agreement of the experimental data (noisy curve in Fig. 6) with the predicted

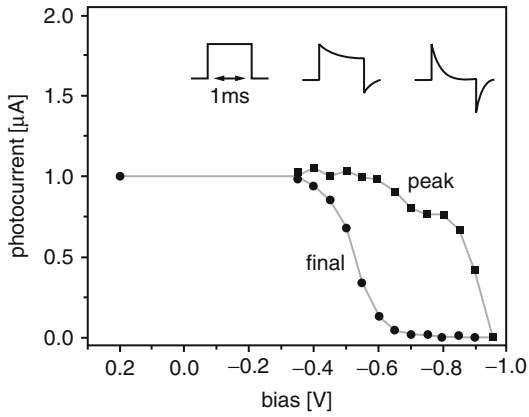

Redox Processes at Semiconductors-Gerischer Model and Beyond, Fig. 5 Peak value (*filled square*) and stationary plateau value (*filled circle*) of the photocurrent transient in response to a rectangular illumination pulse of 1 ms duration in dependence on the voltage bias. The inbuilt depletion layer voltage is decreased with the bias shifting in negative direction. The flat-band potential is at – 0.95 V. The reduced redox ions that can discharge the holes at the surface are 0.005 M 1,1′-dimethylferrocene (Reproduced from upper part of Fig. 4, Ref. [16])

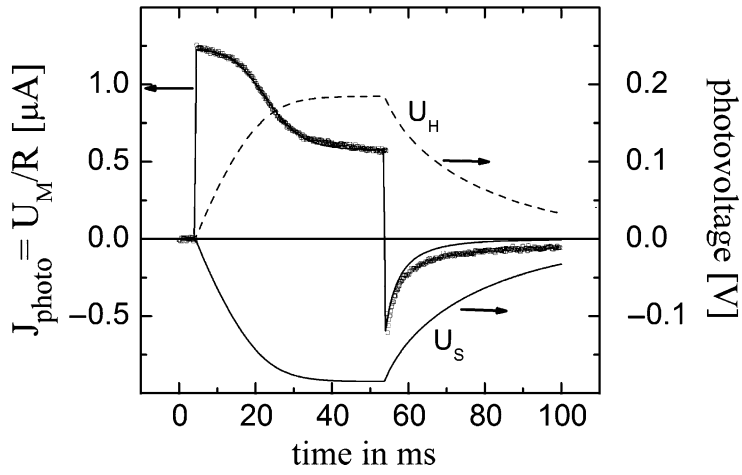

Redox Processes at Semiconductors-Gerischer Model and Beyond, Fig. 6 (Reproduced from upper part of Fig. 5, Ref. [16])

time dependence of the photocurrent transient (thin solid curve in Fig. 6). In summary, the photocurrent transient does not show the rate constant of electron transfer at the interface. From its shape one can obtain qualitative information on whether recombination or discharge is dominating the fate of the photo-generated minority carriers at the surface.

Photocurrent transient (voltage across R_M) in response to a rectangular illumination pulse. The signal is strongly asymmetric with respect to beginning and end of the illumination. The concentration of reduced redox ions is negligible, and recombination of the holes with electrons dominates their fate. The calculated thin curve virtually merges with the measured noisy curve except for some deviation at the right-hand side. The voltage calculated for the Helmholtz layer U_H and for the depletion layer U_S cannot be measured.

Electron Injection into a SC Electrode from Photoexcited Adsorbed Molecules

Several interesting effects can arise in dye-sensitized charge injection, for example, spin-dependent recombination kinetics that has been studied with organic insulator crystals functioning as electrodes [18]. There are several ways of light-induced charge injection, e.g., injection from the locally excited electronic dye molecule into a semiconductor or direct optical electron transfer from the ground state of an adsorbed molecule to states in the empty conduction band of a semiconductor. Experiments have shown that the latter process is less efficient than the first one [19]. The most impressive progress has been made in this field with the recent feasibility of measurements on the femtosecond time scale. The most important tool for studying the latter is a frequency tunable laser generating pulses of a few femtosecond duration. The most recent progress is the direct measurement of the energy distribution of the injected electron in the electronic acceptor states of the semiconductor [20, 21]. The data is collected as femtosecond two-photon photoemission signal [20–22]. The energy distribution of the corresponding excited molecular donor state has been obtained from the stationary absorption spectrum of the adsorbed molecule [22, 23]. Time-dependent interfacial electron transfer in the above system is probed either by femtosecond transient absorption spectroscopy [24–26], mostly applied in the case of a nanostructured electrode, or by femtosecond two-photon photoemission (fs-2PPE) spectroscopy [20, 21] which is more sensitive and able to time-resolve the reaction on a well-prepared planar surface in ultrahigh vacuum. Since the solvent environment of a traditional electrochemical system has been omitted from these systems, the investigations focus on the role of the high-energy (quantum) molecular vibrations in the dynamics. We note here that adding a solvent environment would cause a downward energy shift of the electronic levels in the adsorbed molecule, introduce additional inhomogeneous broadening of the electronic levels, increase the reorganization energy of the reaction, and would make transient absorption measurement extremely difficult in the most relevant time window shorter than 100 fs. The solvent when excited by an ultrashort laser pulse generates the so-called coherent artifact which obscures the actual signal. The ET reaction would still occur on the same time scale as in the absence of the solvent if the downshift of the electronic level due to the solvent environment is compensated and the molecular donor level still positioned high enough above the lower conduction band edge. Vibrational peaks would be broadened or completely obscured due to additional inhomogeneous broadening caused by the solvent environment. To avoid these difficulties and for employing fs-2PPE, the experimental data shown below was collected in ultrahigh vacuum.

The availability of time-resolved [20, 26] and frequency-resolved experimental data [22, 23] for the same systems has motivated several different theory groups to model ultrafast heterogeneous electron transfer with advanced theoretical tools [23, 27–34]. Recent quantum mechanical calculations of the injection dynamics [23, 27–30, 34] are not any more based on a perturbation

approach as was customary for earlier model calculations but permit an arbitrarily high value for the electronic interaction energy between the excited state of the molecular donor and the electronic acceptor states of the solid. Thus, the new theoretical calculations can address the experimentally observed ultrashort electron transfer times of a few femtoseconds. The simplest assumption about the electronic coupling is a constant matrix element across the whole conduction band of the semiconductor. By choosing perylene as the molecular donor with its excited donor level located high above the lower conduction band edge of the wide-gap semiconductor TiO_2 [20], the most general case of a heterogeneous electron transfer reaction can be realized. This case is referred to as the wide-band limit [35], where the complete electron transfer spectrum is mapped as energy distribution of the injected electron onto the continuum of empty electronic states of the electrode [20]. Another advantage of using perylene as the donor is vibrational structure in the optical spectra being dominated by just one high-energy vibrational mode. Therefore, low-resolution spectra can be fitted by considering only this 0.17 eV skeletal stretch mode [23]. The injection dynamics predicted by the fully quantum mechanical calculations for the perylene/TiO_2 system is illustrated in Fig. 7.

The dynamics [27, 28, 37] is characterized by two different energy distributions, i.e., that of the donor state and that of the injected electron, as illustrated in Fig. 7. The corresponding electron injection from an excited donor state high above the lower edge of the conduction band occurs in the wide-band limit [35] and gives rise to an exponential decay in the population of the donor state due to electron transfer [37]. This general case is realized by the perylene dye/TiO_2 systems [20, 26]. Strong coupling of the electronic states to high-energy vibrational modes [7–9] is a characteristic feature of all the molecules that have been used as visible light sensitizers of wide bandgap semiconductors. This strong coupling leads to the wide energy spread and vibrational structure in the energy distribution of the injected electron. Just one high-energy vibrational mode is considered in Fig. 7 since this is sufficient for describing low-resolution spectra of perylene dye/TiO_2 systems [23, 38] used in the experiments. The energetic position of the donor state with respect to the conduction band of TiO_2 is known from UPS data combined with optical absorption spectra and independently from two-photon photoemission experiments [20]. Excitation by an ultrashort laser pulse creates the excited donor state at the respective photon energy above the ground state [20, 28]. When generated by an ultrashort laser pulse, the energy distribution of the donor state consists firstly of the width of this laser pulse, secondly of a Lorentzian which is controlled by the ET time

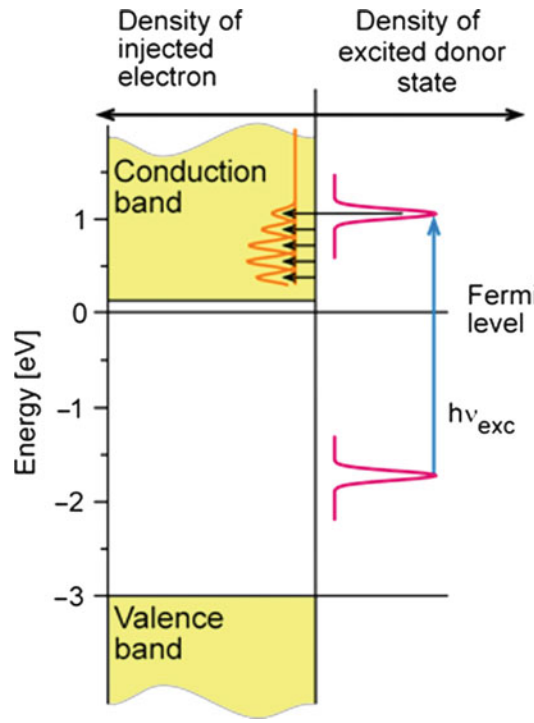

Redox Processes at Semiconductors-Gerischer Model and Beyond, Fig. 7 Scheme illustrating laser pulse induced ultrafast nonadiabatic heterogeneous electron transfer according to fully quantum mechanical model calculations [27, 28, 30, 31, 34]. The energy distribution of the excited molecular donor state (*upper red curve*) is much narrower than the energy distribution of the injected electron. The latter spreads from the donor state to lower energies in the electronic acceptor states and shows vibrational structure. For details see text (Reproduced from Fig. 1 Ref. [36])

of the system [29, 35], and thirdly by any inhomogeneous distribution of the states involved in the electronic transition [20]. The excited donor state shifts with higher photon energy to a higher vibrationally excited state (not shown in Fig. 1). Redistribution of vibrational excitation energy to other modes is much slower than ultrafast electron injection from the initially excited vibrational state in this system [39]. The dynamics in this system is very different from earlier injection scenarios where it was assumed that redistribution of vibrational excitation energy occurs either faster than electron transfer or at least on a comparable time scale. Figure 7 shows the energy distribution of the injected electron to spread from the excited donor state to acceptor states at much lower energies. The energy lost by the injected electron is used for exciting a high-energy (quantum) vibrational mode in the ionized molecule. Specific advantages of using the perylene/TiO_2 system for testing the theoretical predictions illustrated in Fig. 7 are firstly the high-lying excited singlet state which functions as the donor state and realizes the wide-band limit [35], secondly slow redistribution of vibrational excitation energy on the picosecond time scale [39] and much slower singlet–triplet conversion, and thirdly the fact that low-resolution spectra [23, 37] are dominated by just one high-energy vibrational mode, i.e., the 0.17 eV skeletal stretch mode.

The electron transfer spectrum is obtained as a cross section along the energy axis [20, 22] through the complete set of the fs-2PPE data [23, 39], in this case for the perylene/TiO_2 system with the –COOH anchor–bridge group (Fig. 8a). The injected electron spreads over a wide energy range reaching electronic acceptor levels more than 0.5 eV below the donor state. Convoluting a spectrum structured by the dominant 0.17 eV stretch mode of perylene with a Gaussian of 80 meV width (FWHM), which accounts for the instrumental response of the used time-of-flight (TOF) detector [20], results in the fit to the data points. Fully quantum mechanical model calculations have shown that the femtosecond two-photon photoemission (fs-2PPE) signal preserves both energy spread and vibrational structure of the energy distribution of the injected electron [39]. The energetic width of the donor state has been extracted from the stationary absorption spectrum of the adsorbed molecules [22]. The scheme in Fig. 7 considers also additional broadening due to the short laser pulse. The energy distribution of the injected electron covers a much wider range than the excited donor state. The injected electron retains its energy distribution unchanged for a sufficiently long time in this system, here 200 fs [20] allowing for the measurement of the initial distribution. The electron is injected into surface states, probably created by the anchor groups where energy relaxation is much slower than the 40 fs time scale measured for energy relaxation in bulk states of TiO_2 [40]. By inserting different anchor–bridge groups between the perylene chromophore and the surface atoms of TiO_2 the injection time has been varied from 10 fs to one picosecond [20]. With perylene attached via the anchor–bridge group $–CH_2–SH$ to an Ag electrode electron transfer from the excited state of the molecule occurs on the same time scale of a few fs [21] as for perylene attached via the –COOH group to the TiO_2 electrode. At the metal electrode it would be extremely difficult, however, to measure the initial energy distribution of the injected electron. The latter is immediately distorted by inelastic scattering processes occurring with the high density of thermal electrons in the metal electrode. From Figs. 7 and 8a, it is clear that strong coupling of the electronic states to high-energy vibrational modes controls the dynamics of electron transfer from a typical molecular donor like perylene to the semiconductor TiO_2. Figure 8b explains the choice of the delay time td = 40 fs at which the cross section along the energy axis has been taken to obtain the data points of Fig. 8a. Figure 8b shows a cross section along the time axis through the complete set of fs-2PPE data [20]. The transient contains an early peak arising from photoemission from the excited singlet state of perylene and a second peak due to photoemission from the injected electrons at the surface of TiO_2. The latter population is generated from the first population. Thus, the first peak decays with

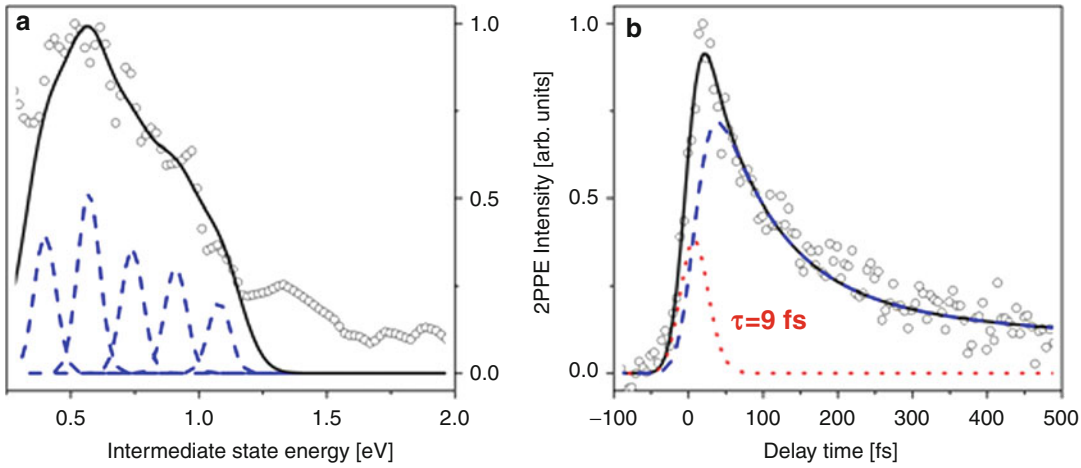

Redox Processes at Semiconductors-Gerischer Model and Beyond, Fig. 8 (**a**) Experimental data points are obtained from a cross section along the energy axis of the complete set of femtosecond two-photon photoemission data [20]. The data points are collected at a delay time of 40 fs determined from the data shown in (**b**). The energy distribution of the data points can be fitted using a structured spectrum predicted by a theoretical model for the perylene/TiO_2 system [39] and by convoluting with the response function of the used time-of-flight detector. (**b**) Experimental data points are obtained from a cross section along the time axis of the complete set of femtosecond two-photon photoemission data [20]. The transient contains two contributions; photoemission from the excited molecular donor state is followed by photoemission from the electronic acceptor states filled via electron transfer from the donor state. The time constant for the decay of the first peak is identical with that for the rise of the second peak, i.e., it is the electron transfer time, here 9 fs (Reproduced from Fig. 2 Ref. [36])

the same time constant that is controlling the rise of the second peak; it is the electron transfer time, i.e., 9 fs for the –COOH anchor–bridge group [20, 26]. The delay time td = 40 fs is chosen such that the peak due to photoemission from the injected electron is probed after the peak due to photoemission from the excited singlet state has decayed. The ultrafast injection time of 9 fs and the excitation of the high-energy vibrational mode in the ionized molecule demonstrate ultrafast nonadiabatic electron transfer as the dominant ET mechanism. Recent experimental results (Fig. 8) and recent quantum mechanical model calculations are in agreement, but both differ strongly from early quantum mechanical perturbation theory models where it was automatically assumed that nonadiabatic electron transfer is slow. The fully quantum mechanical model of the injection dynamics illustrated in Fig. 7 has the virtue of incorporating strong coupling of the electronic states to high-energy vibrational modes and allowing at the same time for ultrafast ET [27, 28, 30, 31, 34]. Theoretical model calculations of the above type need the input of parameter values which are taken either from experimental data or from specific theoretical calculations.

It is important to note here that the ultrafast injection dynamics are very different from Gerischer's much earlier intuitive injection scenario [41, 42]. The latter assumes strong thermal broadening of the excited donor state which is not borne out by the experimental data [22, 26]. Moreover, a thermally relaxed donor state is assumed in Gerischer's scenario which would imply for the perylene/TiO_2 system that electron transfer must be slowed down by a factor of 1,000 compared to the measured electron transfer times [20, 26] because intermolecular relaxation of vibrational energy has been measured for perylene in the time range of several ps [39]. A correspondingly slow electron injection in the picosecond time domain is realized with an excited donor state located below the conduction band edge rendering electron transfer thermally activated. An experimental example for this case

has been found with electron injection from a dye J-aggregate into AgBr [43]. The latter represents a rather special situation, and the general case shown in Fig. 7 is not described by the Gerischer's scenario for dye-sensitized injection.

The recent fully quantum mechanical model of dye-sensitized electron injection has addressed also the specific border case where the excited donor state lies above but fairly close to the lower edge of the conduction band. For the latter case a slowdown in the electron transfer time is predicted compared to the case of the wide-band limit. Moreover, if the excited donor state is generated with a sufficiently short laser pulse, the population is predicted to show time-dependent oscillations in this border case. Time-dependent oscillations are also predicted for the populations of the injected electron and of vibrational states in the ionized molecule [37, 44]. The electronic level of a donor molecule can be shifted through a chemical modification of the chromophore; however, the chemical change might bring about additional changes in the system. A better defined energy shift of the donor level can be realized with a semiconductor quantum dot where the electronic levels shift with the size of the particle [45]. Recently, a low-lying excited donor state has been realized in the form of an exciton in a PbSe nanocrystal attached to the surface of TiO_2, and strong oscillations have been reported for a second harmonic signal probing this interface [46]. The latter signal could indeed indicate that the theoretically predicted electron transfer dynamics for the border case of a low-lying donor state [37, 44] has been realized in the system, but this has to be checked in more detail.

References

1. Gerischer H (1961) Semiconductor electrode reactions. In: Delahay P, Tobias CW (eds) Advances in electrochemistry and electrochemical engineering, vol 1. Interscience, New York, 4:139–232
2. Notten PHL, van den Meerakker JEAM, Kelly JJ (1991) Etching of III-V semiconductors an electrochemical approach. Elsevier Advanced Technology, Oxfordshire
3. Gerischer H (1960) Über den Ablauf von Redoxreaktionen an Metallen und an Halbleitern. I. Allgemeines zum Elektronenübergang zwischen einem Festkörper und einem Redoxelektrolyten. Z. phys. Chem. NF 26:223–247
4. Marcus RA (1965) J Chem Phys 43:679
5. Ulstrup J, Jortner J (1975) J Chem Phys 63:4358
6. Schmickler W (1976) Electrochim Acta 21:161
7. Halasinski TM, Weissman JL, Ruiterkamp R, Lee TJ, Salama F, Head-Gordon M (2003) J Phys Chem A 107:3660
8. Eastwood D, Gouterman M (1970) J Mol Spectrosc 35:359
9. Zakeeruddin SM, Nazeeruddin MK, Pechy P, Rotzinger FP, Humphry-Baker R, Kalyanasundaram K, Grätzel M (1997) Inorg Chem 36:5937
10. Hale JM (1971) The rates of reactions involving only electron transfer at metal electrodes. In: Hush NS (ed) Reactions of molecules at electrodes. Wiley 229, and references therein
11. Willig F (1981) Electrochemistry a the organic molecular crystal/aqueous electrolyte interface. In: Gerischer H, Tobias CW (eds) Advances in electrochemistry and electrochemical engineering, vol 12. Wiley 1:1, and references therein
12. Gao YQ, Marcus RA (2000) J Chem Phys 113:6351
13. Gao YQ, Georgievskii Y, Marcus RA (2000) J Chem Phys 112:3358
14. Fajardo AM, Lewis NS (1997) J Phys Chem B 101:11136
15. Pomykal KE, Lewis NS (1997) J Phys Chem B 101:2476
16. Schwarzburg K, Willig F (1997) J Phys Chem B 101:2451
17. Willig F (1988) Ber Bunsenges Phys Chem 92:1312–1319
18. Charle KP, Willig F (1988) Spin-dependent kinetics in dye-sensitized charge carrier injection into organic crystal electrodes. In: Conway BE, Bockris JOM, White RE (eds) Modern aspects of electrochemistry. Plenum, New York, pp 359–389
19. Wang L, Willig F, May V (2007) J Chem Phys 126:134110
20. Gundlach L, Ernstorfer R, Willig F (2007) Prog Surf Sci 82:355
21. Gundlach L, Willig F (2007) Chem Phys Lett 449:82
22. Gundlach F, Letzig T, Willig F (2009) J Chem Sci 121:561
23. Wang L, May V, Ernstorfer R, Willig F (2005) J Phys Chem B 109:9589
24. Rehm JM, McLendon GL, Nagasawa Y, Yoshihara K, Moser J, Grätzel M (1996) J Phys Chem 100:9577
25. Burfeindt B, Hannappel T, Storck W, Willig F (1996) J Phys Chem 100:16463
26. Ernstorfer R, Gundlach L, Felber S, Storck W, Eichberger R, Willig F (2006) J Phys Chem B 110:25383
27. Ramakrishna S, Willig F, May V (2000) Phys Rev B 62, R16330

28. Wang L, Willig F, May V (2006) Mol Simul 3:765
29. Persson P, Lundqvist MJ, Ernstorfer R, Goddard WA III, Willig F (2006) J Chem Theory Comput 2:441
30. Sebastian KL, Tachya M (2006) J Chem Phys 124:064713
31. Kondov L, Thoss M, Wang H (2006) J Phys Chem A 110:1364
32. Prezhdo OV, Duncan WR, Prezhdo VV (2009) Prog Surf Sci 84:30
33. Abuabara SG, Rego LGC, Batista VS (2005) J Am Chem Soc 127:1823
34. Mohr J, Schmickler W, Badiali JP (2006) Chem Phys 324:140
35. Muscat JP, Newns DM (1978) Prog Surf Sci 9:1
36. Gundlach L, Willig F (2012) Ultrafast photoinduced electron transfer at electrodes: the general case of a heterogeneous electron transfer reaction, Chem Phys Chem 13 doi:10.1002/cphc.201200151 p. 2877–2881
37. Ramakrishna S, Willig F, May V, Knorr A (2003) J Phys Chem B 107:607
38. Tsivlin DV, Willig F, May V (2008) Phys Rev B 77:035319
39. Zimmermann C, Willig F, Ramakrishna S, Burfeindt B, Pettinger B, Eichberger R, Storck W (2001) J Phys Chem B 105:9245
40. Gundlach L (2005) Dissertation, Freie Universität Berlin, http://wwwdissfu-berlinde/diss/receive/FUDISS_thesis_000000001801
41. Gerischer H (1972) Photochem Photobiol 16:243
42. Gerischer H, Willig F (1976) Reactions of excited dye molecules at electrodes. In: Boschke FL (ed) Topics in current chemistry. Springer, Berlin, pp 31–84
43. Troesken B, Willig F, Schwarzburg K, Ehret A, Spitler M (1995) J Phys Chem 99:5152
44. Ramakrishna S, Seideman T, Willig F, May V (2009) J Chem Sci 121:589
45. Brus LE (1984) J Chem Phys 80:4403
46. Tisdale WA, Williams KJ, Timp BA, Norris DJ, Aydil ES, Zhu XY (2010) Science 328:1543

Reference Electrodes

Heike Kahlert
Institut für Biochemie, Universität Greifswald, Greifswald, Germany

Introduction

Reference electrodes are necessary to control the potential of a working electrode (e.g., during voltammetric measurements) or to measure the potential of an indicator electrode in potentiometric measurements, since the Galvani potential difference of a single electrode is not measurable [1]. An ideal reference electrode would have the following characteristics:

(i) It is chemically and electrochemically reversible, i.e., its potential is governed by the Nernst equation, (ii) the potential should remain practically constant, when current flows through the electrochemical cell (ideally nonpolarizable electrode), and (iii) the thermal coefficient should be small. Whereas there is no practical reference electrode that offers all these properties to the same extent, a variety of reference systems very close to that ideal behavior exist [2, 3]. The choice and construction of the reference electrode depend on the experimental conditions such as temperature, pressure, size, nature and composition of the electrolyte, and the electrochemical method applied in the measurement. With voltammetric or amperometric techniques, the tolerated uncertainty in the potential is still relatively large since the analyte concentration is related primarily to the measured current, which is quite constant in a certain potential window. With potentiometric sensors, however, the zero-current potential is directly related to the activity of the analyte ion. The potential change at the reference electrode as a function of the sample composition must therefore be kept reliably small. In the two-electrode configuration in voltammetric measurements, one of the electrodes may also play the role of a reference electrode. The same metal can be used for both electrodes (the working and the counter/reference electrode) if the surface area of the reference electrode is much higher than that of the working electrode, since the electrode potential is varied by the current density, i.e., in that case the current density of the working electrode is much higher than that on the reference electrode and hence the potential change at the reference electrode is small. A classical example is the large nonpolarizable mercury pool electrode in Heyrovský dc polarography. The two-electrode configuration is also widely used in arrangements with microelectrodes as working electrodes. The primary standard in electrochemistry is the standard hydrogen electrode, the potential of which is

zero by definition [4]. Because of the difficulties in handling with the standard hydrogen electrode, reference electrodes of the second kind or quasireference electrodes are widely used. If the reference electrode consists of compartments including electrolyte solutions, it has to be separated from the test solution. For this purpose, a diaphragm is used in order to prevent the mixing of both solutions while providing the conductivity between them. Common materials are porous like sintered glass and porcelain. Different arrangements of diaphragms are given in [3]. To prevent a contact between the analyte solution and the reference electrolyte, a second salt bridge (double salt bridge) is recommendable.

In the following, a short overview of the most widespread and most important reference electrodes will be given.

Quasireference Electrodes

Quasireference electrodes are simple noble metal wires (silver, gold, platinum) or plane layers of these metals maintaining a given but not well-defined potential during the course of an electrochemical measurement. They have to be calibrated with an inner standard or with respect to a conventional reference electrode. A reference redox couple like complexes between large ligands and a transition metal, e.g., the redox couple ferrocene/ferrocenium, can be used as an inner standard, especially in nonaqueous solutions [5–7]. The calibration with respect to a conventional reference electrode is only reliable when one can be sure that the potential of the quasireference electrode is the same in the calibration and in the application experiment. The main advantage of a quasireference is that no additional reference electrolyte solution is necessary, and hence, a contamination of the test solution by solvent or ions of a reference electrolyte is excluded.

The Hydrogen Electrode

The hydrogen electrode consists of a platinum wire or a platinum sheet covered with platinum black (i.e., platinized) and an acidic aqueous electrolyte solution. The hydrogen gas is usually continuously supplied. The reversible electrochemical equilibrium can be formulated as follows:

$$H_2 + 2H_2O \overleftrightarrow{} 2H_3O^+ + 2e^- \qquad (1)$$

The Galvani potential difference of such electrode is:

$$\begin{aligned}\Delta\phi &= \Delta\phi^{\ominus} + \frac{RT}{2F}\ln a^2_{H_3O^+} + \frac{RT}{2F}\ln\frac{1}{f_{H_2}} \\ &= \Delta\phi^{\ominus} + \frac{RT}{F}\ln\frac{a_{H_3O^+}}{\sqrt{f_{H_2}}}\end{aligned} \qquad (2)$$

By definition, the potential of the standard hydrogen electrode (SHE) is zero at all temperatures. The standard conditions are defined as:

$$a_{H_3O^+} = 1$$

$$\left(\text{i.e., } a_{H_3O^+} = \gamma_{H_3O^+} + \frac{m_{H_3O^+}}{m^{\ominus}} \text{ with } \gamma_{H_3O^+} = 1,\right.$$

$$\left. m_{H_3O^+} = 1\,\text{mol kg}^{-1}, \text{ and } m^{\ominus} = 1\,\text{mol kg}^{-1}\right)$$

and $f_{H_2} = 1$ (i.e., the fugacity of hydrogen is calculated according to $f_{H_2} = \gamma_{H_2}\frac{p_{H_2}}{p^{\ominus}}$ with $\gamma_{H_2} = 1$, $p_{H_2} = 1$ bar $= 10^5$ Pa, and $p^{\ominus} = 1$ bar $= 10^5$ Pa). Earlier, $p^{\ominus} = 1$ standard atmosphere $= 101.325$ kPa was used. It causes a difference in the potential of SHE of +0.169 mV, and this value has to be subtracted from the standard electrode potentials given previously in different tables. However, because of the uncertainty of the $E^{\ominus}$ values of about 1 mV, this difference can be neglected. As it is difficult to adjust the activity of hydronium ions to 1, for practical purpose, relative hydrogen electrodes (RHE) in acidic solutions are widely used. The nature and the concentration of the acid is the same in the reference and in the test solution. The potential of the electrode can be calculated by using well-known activity coefficients of the hydrochloric acid. The standard hydrogen electrode allows very precise measurements to be

made; however, the demanding handling restricts its use [8]. For instance, the hydrogen gas must be of highest purity, esp. with respect to oxygen, H_2S, AsH_3, SO_2, CO, and HCN because these gases poison the platinum electrode. In solution, volatile substances, e. g., HCl, can be purged from the solution by the hydrogen gas, metals can be reduced at the electrode, redox systems may influence the electrode potential, etc.

Practical Reference Electrodes of the Second Kind

Electrodes of the second kind consist of a metal, a sparingly soluble salt of this metal (or an oxide or hydroxide of this metal), and an electrolyte containing the anions of the sparingly soluble compound to establish an equilibrium with the precipitate. The potential of the electrode depends on the fixed activity of the anion in the solution.

The silver/silver chloride electrode is an example of this kind of electrodes, and beside the calomel electrode most commonly used. The net reaction can be described by the following equation:

$$Ag^0 + Cl^- \overleftrightarrows AgCl \downarrow + e^- \qquad (3)$$

The activity of the metal ions in the solution depends on the solubility equilibrium and can be described by the solubility product K_s according to:

$$a_{Ag^+} = \frac{K_s}{a_{Cl^-}} \qquad (4)$$

Thus, the electrode potential is proportional to the logarithm of the activity of the chloride in the electrolyte solution:

$$\begin{aligned} E &= E^{\ominus}(Ag,\ Ag^+) + \frac{RT}{F} \ln a_{Ag^+} \\ &= E^{\ominus}(Ag,\ Ag^+) + \frac{RT}{F} \ln K_s - \frac{RT}{F} \ln a_{Cl^-} \end{aligned} \qquad (5)$$

or

$$E = E_c^{\ominus\prime}(Ag,\ AgCl) - \frac{RT}{F} \ln a_{Cl^-} \qquad (6)$$

$E_c^{\ominus\prime}(Ag,\ AgCl)$ is the formal potential of the silver/silver chloride electrode including the solubility product.

The common arrangement of the silver/silver chloride electrode is that a silver wire is covered with silver chloride, which can be achieved chemically or electrochemically. The electrolyte solution in these reference systems is normally a potassium chloride solution (mostly saturated or 3M) and only seldom sodium or lithium chloride. Compared to the calomel electrode, the silver/silver chloride reference system has the great advantage that measurements at elevated temperatures are possible. Special devices have been developed based on the silver/silver chloride reference systems for measurements in high temperature aqueous solutions [9] and under changing pressure conditions [10]. Because reference systems based on silver/silver chloride can be produced in a very small size and also as planar layers, they are often used in microsystems.

The calomel electrode consists of mercury and mercury (I) chloride (calomel Hg_2Cl_2) in contact with a potassium chloride solution of constant activity. In case that the supporting electrolyte in the cell contains perchlorate anions, it is advisable to use NaCl instead of KCl since $KClO_4$ is sparingly soluble and could precipitate in the diaphragm. In most cases, saturated KCl solution is used; however, in such solution already at temperatures above 35 °C, a disproportion reaction takes place. The back reaction by cooling down the electrode is very slow so that a hysteresis of the electrode potential occurs. This is the reason why it is recommended that the calomel electrode only be used at temperatures in maximum up to 70 °C. In Table 1 electrode potentials of the silver/silver chloride electrode and for the calomel electrode at different temperatures and different concentrations of KCl are given. Note that the electrode potentials differ when other salts than potassium chloride (e.g., NaCl) are used because of the different solubility products.

The trend in the development of modern electroanalytical techniques is a miniaturization of

Reference Electrodes, Table 1 Electrode potentials of the calomel electrode and of the silver/silver chloride electrode at different temperatures and different concentrations of KCl (the concentrations are related to 25 °C) [3]

	E/mV			
	Calomel		*Silver/silver chloride*	
T/°C	c_{KCl} 1 mol L^{-1}	Saturated	c_{KCl} 3 mol L^{-1}	Saturated
0			224.2	220.5
10	285.4	260.2	217.4	211.5
20	283.9	254.1	210.5	201.9
25	281.5	247.7	207.0	197.0
30	280.1	244.4	203.4	191.9
40	278.6	241.1	196.1	181.4
50	275.3	234.3	188.4	170.7
60	271.6	227.2	180.3	159.8
70	267.3	219.9	172.1	148.8
90	262.2	212.4	153.3	126.9

the measuring devices, including the reference electrodes. Although the development of new technological approaches such as the thick film and thin film techniques supported arrangements with planar reference electrodes, special problems with miniaturized reference electrodes still exist, and there is no general role for the conception of an integrated micro reference electrode. The lifetime of miniaturized reference electrodes is limited because of the non-negligible solubility of AgCl, the reduced electrolyte volume (rapid contamination as well as exhaustion and drying out of the reference electrolyte), the miniaturization of the diaphragm (small pores can easily be blocked), etc.

References

1. Bard AJ, Faulkner LR (2001) Electrochemical methods, 2nd edn. Wiley, New York, pp 24–28
2. Ives DJG, Janz GJ (1961) Reference electrodes. Academic, New York
3. Kahlert H (2010) Reference electrodes. In: Scholz F (ed) Electroanalytical methods, 2nd edn. Springer, Berlin, pp 291–308
4. Inzelt G (2006) Standard potentials. In: Bard AJ, Stratman M, Scholz F, Pickett CJ (eds) Inorganic electrochemistry, vol 7A, Encyclopedia of electrochemistry. Wiley-VCH, Weinheim, p 1
5. Gritzner G, Kuta J (1982) Recommendations on reporting electrode potentials in nonaqueous solvents. Pure Appl Chem 54:1527–1532
6. Gritzner G, Kuta J (1984) Electrode potentials in nonaqueous solvents (recommendations 1983). Pure Appl Chem 56:461–466
7. Lund H (1983) Reference electrodes. In: Baizer MM, Lund H (eds) Organic electrochemistry. Marcel Dekker, New York
8. Buck RP, Rondinini S, Covington AK, Baucke FGK, Brett CMA, Camoes MF, Milton MJT, Mussini T, Naumann R, Pratt KW, Spitzer P, Wilson GS (2002) Measurement of pH. Definition, standards, and procedures (IUPAC Recommendations 2002). Pure Appl Chem 74:2169–2200
9. Lvov SN, Gao H, Macdonald DD (1998) Advanced flow-through external pressure-balanced reference electrode for potentiometric and pH studies in high temperature aqueous solutions. J Electroanal Chem 443:186–194
10. Peters G (1997) A reference electrode with free-diffusion liquid junction for electrochemical measurements under changing pressure conditions. Anal Chem 69:2362–2366

Refractory Metal Production by Molten Salt Electrolysis

Pierre Taxil
Laboratoire de Génie Chimique, Université de Toulouse, Toulouse, France

General Comments

Certain elements of the middle part of the periodic table (columns IVB, VB, and VIB), devoted to transition metals, are so-called refractory metals because of their high fusion temperature (above 2,000 °C), which have relevant consequences in particular on their thermoelastic properties, microhardness, and a correlative industrial use as tools for metal working at high temperature [1, 2] and formally their use as resistance in light bulbs. The most relevant elements of this category are tantalum, niobium (col. IVB), hafnium and zirconium (VB), and molybdenum and tungsten (VIB). Another important common property of them is the thermodynamic stability of their oxide coatings which offers them high

corrosion resistance in oxidizing conditions comparable to noble metals whereas they are considered intrinsically among the most reactive metals [3]. Their particularity of shutting oxidation currents and opening reduction currents puts them in the category of valve metals, with other well-known metals such as titanium [4]. These metals coated with their oxide layer in surface find a lot of applications: supercapacitors with Ta or Nb, with high dielectric constant and potential breakdown [5] for high-tech electronics (mobile phones, camcorders, and computers); microhardness for tools and surgery; and superconductivity of pure Nb and Nb alloys [5] for supermagnets. Their relative low abundance in the earth's crust makes them strategic substances, sensitive to the market price, recyclables and explains the trend to use them, for applications calling on their surface properties as a thin coating over usual metals.

The elaboration of refractory metals consists of reducing their salts or oxide phases by oxidant compounds. Molten salt electrolysis is appropriate for this application, for various reasons: First is their extended electrochemical window (more than 3 V) that allows the ions of most of the reactive metals to be discharged before the solvent and then lower cost, lower pollution, and easiness of processing, compared to metallothermic processes, are to be noticed [6]. Nevertheless, refractory metals being multivalent elements, the chemical composition of the electrolyte is critical for avoiding the formation of stable intermediate species instead of the metal during the electroreduction process.

This chapter aims to describe the elaboration process and refining of refractory metals by techniques involving molten salt media. Tungsten and molybdenum preparation will not be mentioned, as far for these elements, molten salt electrolysis is little reported and moreover controversial.

Niobium and Tantalum

These metals have similar properties, and they are together in one of their natural origins, the so-called columbite ore, containing columbium (former name of niobium) and tantalum. Nevertheless, their respective production and use rates are quite different: 1,000–1,500 t/year for Ta and about 16,000 t/year for Nb, far more present in the earth's crust than Ta, that explain their respective costs, in inverse ratio of their production level.

The main production sites of Ta are Australia (54 %), Brazil (13 %), Canada, China, South West Asia, and Europe, while Nb provides almost exclusively from Brazil (93 %).

Molten salt route is one relevant way for producing these metals; extractive metallurgy can provide the oxides (Nb_2O_5, Ta_2O_5) or the fluoride compounds (K_2NbF_7; K_2TaF_7).

Chloride and Fluoride Melts

Niobium oxides, provided by the ore treatment, are dissolved in chloride melts (NaCl-KCl or LiCl-KCl) in the form of $NbCl_5$ [7], and Nb metal is produced by electroreduction in the molten chloride solution. A French company, Cezus, developed this process at the industrial scale in the 1990s [8] for Nb and other refractory metals. Nevertheless, the cathodic process in pure chloride melts was proved to be too complex to be industrially valid, with a series of intermediate steps [8, 9], and provides nonadherent or powder metal layers with a low current efficiency. Better results are obtained in chloride melts containing fluoride ions because of the complexation of Nb in NbF_7^{2-} ions which are reduced in only two steps: $Nb^V \rightarrow Nb^{IV} \rightarrow Nb$ [10, 11], with current efficiencies less than 100 % since Nb^V reacts readily with Nb cathodic product (proportionation reaction) for giving the intermediate species, Nb^{IV}.

The complexing role of fluoride ions in the reduction of refractory metals is now well known for the metal recovery [12]. The technology of extracting tantalum in molten salts is based on the formation of K_2TaF_7, obtained by reaction of HF on the oxide Ta_2O_5 extracted from raw materials [14] before the reduction of this compound by sodium in the liquid phase:

$$K_2TaF_7 + 5\ Na \rightarrow\ Ta + 5\ NaF + 2\ KF$$

Other salt compounds are added in the reactor for lowering the temperature between 400 °C and 900 °C below the fusion point of pure K_2TaF_7 [13]. Another reduction mode involves the electrochemical reduction of K_2TaF_7 in molten fluoride salts [5]. It is well stated now that the electroreduction of Ta^V in fluorides proceeds in a five-electron single step directly leading to Ta metal [14], and thus current efficiency of the preparation of Ta by the electrochemical route is close to 100 %.

Anode Reaction

Classically the anode material is mostly carbon, cheap, and an appropriate material. In pure fluoride melts, the reaction would be the discharge of fluoride ions, reacting with carbon to give perfluorocarbons, highly polluting gas, CF_4 or C_2F_6, at high overpotentials. For this reason, pure fluoride melts must be avoided for electrowinning refractory metals. Chlorides must be always present in the electrolyte in order to develop the discharge of Cl^- ions in Cl_2 at the anode.

Niobium and Tantalum Coatings

Taking into account on one hand the low resources of Nb and Ta on the earth and on the other hand that a great part of their properties concerns their surface only, it seems to be really reasonable to use them as surface coatings on more usual metals or carbon. The anodic metal is Ta or Nb, and the electrolysis allows the anodic metal to be transferred from the anode to the cathode surface, according to an electrorefining operation. During these last decades, successful coatings were realized in pure fluoride melts, with Ta and Nb [15, 16], exhibiting such characteristics (compacity, adherence on the substrate, and purity) that they are directly available for applications of the metal coating [16].

Niobium and Tantalum Alloys and Compounds

Superconducting niobium alloys with nickel, titanium, and germanium are prepared by coelectrodeposition in molten salts (Nb-Ge [17], Ti-Nb [18]); or metalliding: Ni-Nb [19].

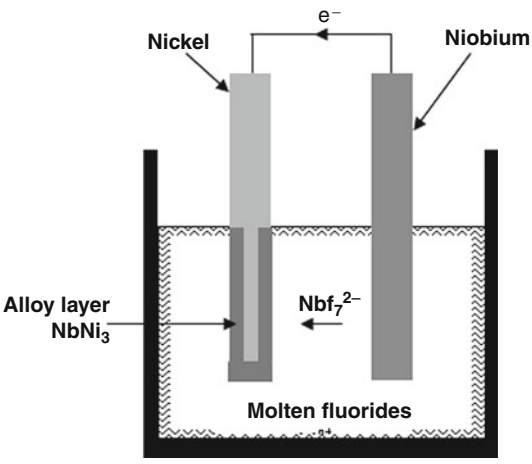

Refractory Metal Production by Molten Salt Electrolysis, Fig. 1 Principle scheme of metalliding of nickel with niobium

This process works as a galvanic cell where the anodic metal (Nb) dissolves in the bath. Nb ions react with the cathodic metal (Ni) to give a defined compound $NbNi_3$ (Fig. 1). Likewise, tantalum and niobium carbides are also prepared by coelectrodeposition of Ta and C [20] or metalliding [21].

Hafnium and Zirconium

Hafnium and zirconium are in the same column of the classification in the periodic table and have hence similar properties except in the nuclear field. Both are associated in the same ore, called zircon, containing only 2–3 % Hf compared to Zr. The production of zircon is abundant: 800,000 t/year in Australia (57 %), South Africa (25 %), and other countries. The treatment of zircon leads to the oxide ZrO_2, zirconia (with 2–3 % of HfO_2), which has its own and well-known applications as refractory ceramics. Electrowinning of pure Zr and pure Hf needs the dissolution of the oxides and their exhaustive separation in advance, Zr being neutron transparent and used as fuel sheath, while Hf is impervious to neutrons and involved in the control systems of nuclear reactors. Carbochlorination in molten chlorides of the oxides leads to $ZrCl_4$ with 2–3 % of $HfCl_4$.

Distillation of $ZrCl_4$-$HfCl_4$ Mixtures

This technology is based on the circulation, at 350 °C and under the atmospheric pressure, of the gaseous ascending $ZrCl_4$-$HfCl_4$ mixture going in contact with a solution $AlCl_3$-KCl, descending in the column. The distillation process leads to the collection of $ZrCl_4$, more soluble in the liquid phase in the bottom of the column, while pure $HfCl_4$ is recovered in the gas phase from the top of the column. The process, finalized by Cezus in 1981, offers the advantage of a significantly lower cost of chemicals than liquid-liquid extraction and more efficiency and more productivity than fractionated crystallization [22].

Zirconium and Hafnium Electrowinning

Zirconium is prepared from $ZrCl_4$ by the Kroll process (chemical reduction of the chloride by liquid magnesium at 900 °C), but the electrochemical route in molten salts is considered as a good alternative. As for Ta and Nb, pure chloride melts are not appropriate for the electrowinning to yield the metal because of too complex cathode process. The addition of fluoride ion source (KF) allows to stabilize Zr ions in the form of K_2ZrF_6 which is reduced in one step to Zr [23].

For hafnium electrowinning, electrolysis process is readily preferred to Kroll process; Cezus developed the process in pure chloride media from $HfCl_4$, reduced in Hf in a one single step [24]. However, the mechanism is controversial, other authors proposing two steps in pure chloride and a single step in chloride-fluoride melts [25].

Electrowinning by Direct Reduction of Metal Oxides (FFC Process)

Discovered in 1997 at the Cambridge University by **F**arthing, **F**ray, and **C**hen (FFC) and developed in the industry from 2001, this recent process involves a molten salt electrolyzer with a cathodic basket containing metal oxides and a carbon anode [26]. The cell polarization promotes the deoxidation of metal oxides by a cathode reaction releasing O^{2-} ions in the bath, the ionic transfer of these ions towards the anode and the anodic formation of CO_2 (Fig. 2). The process is based on the ability of the solvent cation to gain oxide ions at the cathode interface.

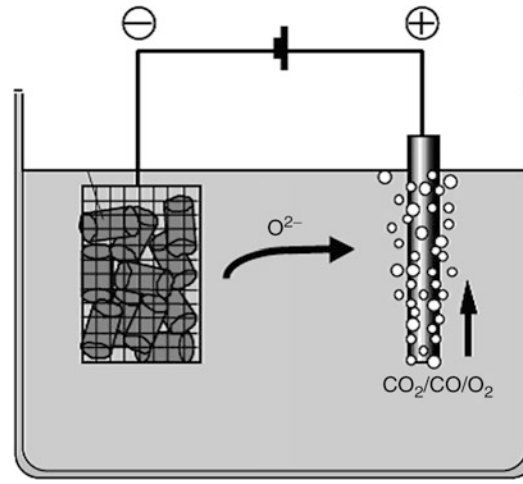

Refractory Metal Production by Molten Salt Electrolysis, Fig. 2 Principle scheme of the FFC process

Calcium and lithium having a high affinity for oxygen in molten salts are appropriate for this role. The solvent and temperature mostly selected are LiCl-$CaCl_2$ and 850–900 °C, respectively. The patent of the process claims that a host of metals such as Ti, Ge, Si, Zr, Hf, Sm, U, Ta, and Nb or their alloys can be produced with starting materials as oxides [27]. The most cited metal produced by this technology is now titanium (from TiO_2) but the English company Metalysis developed a complete device for the production of tantalum from Ta_2O_5 [28]. Alloys such as Nb_3Sn are also prepared by mixing the oxides of parent metals in the appropriate ratio for the alloy.

FFC process exhibits advantages compared to the other metallothermic processes such as Kroll process, in particular a lower cost and far less polluting, but it has major drawbacks:

- The low conductivity of the oxides and of the insufficient contact with the metal basket at the origin of low current efficiencies (less than 50 %).
- The anode reaction consumes carbon leading to the greenhouse gases CO and CO_2; moreover

CO_2 is partially soluble in molten solutions to react with O^{2-} to form carbonate ions which are reduced at the cathode, which causes further decrease in the current efficiency. Inert anodes are now being developed for discharging O^{2-} directly in the form of O_2, but a higher anodic voltage by 1 V is necessary.

Recycling of Refractory Metals

Recycling of refractory metals from wastes is an important issue today since they are in relatively low amount in the earth's crust and it should really be a substantial economy of expensive raw materials and also of energy. Molten salt electrolysis is proved to be appropriate to this function which can be assimilated in the case of metallic wastes to electrorefining. Today, waste treatment of other transition metals like actinides or lanthanides is a reality in the nuclear field, while other strategic elements such as silicon are expected to be recovered with a molten salt technology.

Cross-References

► Rare Earth Metal Production by Molten Salt Electrolysis

References

1. Schmid K (2006) Manufacturing engineering and technology. Pearson Prentice Hall, Upper Saddle River, pp 86–93
2. Veronski A, Hejwowski T (1991) Creep-resisting materials, Thermal fatigue of Metals. CRC Press, p 81–93
3. Pourbaix M (1963) Corrosion, Atlas d'équilibres thermodynamiques. Gauthier-Villard, Paris, pp 70–83
4. Young L (1961) Anodic oxide films. Acad. Press, New York; Young L (1954) Anodic oxide films on tantalum electrodes. Trans Faraday Soc, 50:153–171
5. Polak C (2009) Metallurgie et Recyclage du niobium et du tantale. Techniques de l'Ingénieur, M2 365v2 (2–16):1–3
6. Kermarrec M (2004) Applications Industrielles des Sels Fondus, Agence Rhône-Alpes Pour la Maîtrise des Matériaux, Savoie Technolac
7. Gonzales J et al (1998) Chlorination of niobium and tantalum ores. Thermochim Acta 311:61–69
8. Lamaze AP, Paillère P (1990) Fused salts for continuous production of multivalent metal from halide. European patent n°394154A
9. Ting G, Fung KW, Mamantov G (1976) Voltammetric studies of $NbCl_5$. J Electrochem Soc 123:624–631
10. Sienerth KD, Mamantov G Meeting ECS 1993, Proceedings of the symposium on molten salts, pp 365–372
11. Khalidi A, Bouteillon J (1993) Comportement électrochimique de $NbCl_5$. J Appl Electrochem 23:801
12. Chamelot P, Taxil P, Lafage B (1994) Voltammetric studies of Tantalum electrodeposition baths. Electrochem Acta 17:2571–2574
13. Agulyanski A (2003) Potassium fluorotantalate in solid, dissolved and molten conditions. J Fluorine chem 123:155–161
14. Taxil P, Mahenc J (1987) Formation of corrosion resistant layers by electrodeposition of refractory metals or by alloy electrowinning in molten fluoride. JAppl Electrochem 17:261–269; Polyakova LP et al (1992) Secondary processes during electrodeposition of tantalum in molten salts. J Appl Electrochem 22:628–637
15. Senderoff S, Mellors GW (1966) Coherent coatings of refractory metals. Science 153:1475–1481
16. Taxil P (1986) Dépôts de tantale et de niobium dans les sels fondus et leurs applications. Dissertation, Toulouse (France)
17. Cohen U (1983) Electrodeposition of niobium-germanium alloys. J Electrochem Soc 130:1480
18. Polyakova LP, Taxil P, Polyakov EG (2003) Electrochemical behaviour and codeposition of titanium and niobium in chloride-fluoride melts. J Alloys Comp 359:244–255
19. Taxil P, Qiao ZY (1985) Electrochemical alloying of nickel with niobium in molten fluorides. J Appl Electrochem 15:947–952
20. Stern KH, Gadomski ST (1983) Electrodeposition of tantalum carbides from molten salts. J Electrochem Soc 130:300–305; Massot L, Chamelot P, Taxil P (2006) Preparation of tantalum carbide films by reaction of electrolytic carbon coating with the tantalum coating. J Alloys Comp 424(1–2):199–203
21. Chamelot Massot P, Taxil P Preparation of tantalum carbide films by reaction of electrolytic carbon coating with the tantalum coating. J Alloys Comp
22. Tricot R (1994) Techniques de l'Ingénieur. Métallurgie Extractive et recyclage des métaux de transition, Zirconium et Hafnium, M2360
23. Steinberg MA, Sibert ME, Wainer E (1954) Process development of the electrolytic production of zirconium from K_2ZrF_6. J Electrochem Soc 101(2):63–78
24. Lamaze AP, Charquet D (1990) Development of hafnium tetrachloride electrolysis. In: Liddell KC

(ed) Refractory metals. The Minerals Metals and Materials Society
25. Serrano K, Boïko O, Chamelot P, Lafage B, Taxil P (1997) Electrochemical reduction of HfCl4 in molten salts. In: 5th symposium on molten salts chemistry and Technology, Dechema and V., Dresden (Germany)
26. Chen GZ, Fray DJ, Farthing TW, Chen GZ, Fray DJ, Farthing TW (2000) Direct electrochemical reduction of titanium dioxide to titanium in molten calcium chloride. Nature 407(6802):361–364
27. World patent WO 99/64638
28. Jeong SM et al (2007) Characteristics of an electrochemical reduction of Ta_2O_5 for the preparation of metallic tantalum in a LiCl-Li_2O molten salts. J Alloys comp 400:210–215

Regenerative Fuel Cells

Tsutomu Ioroi
AIST, Ikeda, Japan

Introduction

A regenerative fuel cell (RFC) is an electrochemical device that can store electrical energy using hydrogen as an energy medium. While in fuel cell mode, electrical power can be extracted from an RFC system by reacting stored hydrogen and oxygen (air). On the other hand, in electrolysis mode, the storage tank can be refilled with hydrogen (and oxygen) by operating the RFC as a water/steam electrolyzer using electric power and water. Therefore, RFCs are expected to be useful for electrical energy storage (EES) especially for medium- to large-scale systems. As an EES device, a secondary battery can provide a similar function to RFCs. However, one of the advantages of RFCs is that they are free from self-discharge because the active reactants are stored separately from the reactor. An RFC consists of two separate subunit: a fuel cell/electrolyzer subunit and an energy storage subunit. This separation also enables the independent design of the rated output/input power and energy capacity of the RFC system. Another advantage of RFCs over secondary batteries is their higher energy density. The theoretical energy density of the hydrogen/oxygen reaction

$$H_2 + 1/2O_2 \Rightarrow H_2O \quad (1)$$

is 237.3 kJ/mol-H_2O (25 °C, HHV basis), which is equal to 3,660 Wh/kg-H_2O. While this value is simply calculated from the weight of a stoichiometric reactant, a more realistic value is expected to be 400–1,000 Wh/kg-system [1–3]. This is still higher than the value for the current Li-ion batteries ($C_6Li/LiCoO_2$, 387 Wh/kg) [4].

Materials and Structure of an RFC

The materials and structure of an RFC depend on the operating temperature (polymer electrolyte type or solid oxide type), cell design (unitized or separate fuel cell/electrolyzer units), and reactants (H_2/O_2, H_2/Cl_2, H_2/Br_2, etc.).

High-temperature RFCs based on solid oxide electrolyte technology are operated at 700–1,000 °C with H_2/O_2. The materials used for high-temperature RFCs are basically similar to those in solid oxide fuel cells. As an electrolyte material, 8 mol% Y_2O_3 stabilized ZrO_2 (YSZ) is typically used because of its relatively high ionic conductivity and chemical/mechanical stability. A porous mixture of Ni and YSZ (Ni/YSZ cermet) and perovskite-type oxides such as strontium-doped lanthanum manganite (LSM) are used as hydrogen and oxygen electrode materials, respectively [5]. The advantage of high-temperature RFCs is higher overall (round-trip) energy conversion efficiency (electric ⇒ hydrogen ⇒ electric). This is mainly due to electrode kinetic and thermodynamic factors. Under high-temperature conditions, the kinetics of the electrode reaction are accelerated so that electrode polarization, especially for oxygen redox reactions, is significantly mitigated compared to that in low-temperature RFCs. In addition, the $\Delta G/T\Delta S$ ratio of the water-splitting reaction decreases with an increase in temperature, which means that the demand for electric energy is reduced and a significant portion of the required energy can be provided as thermal

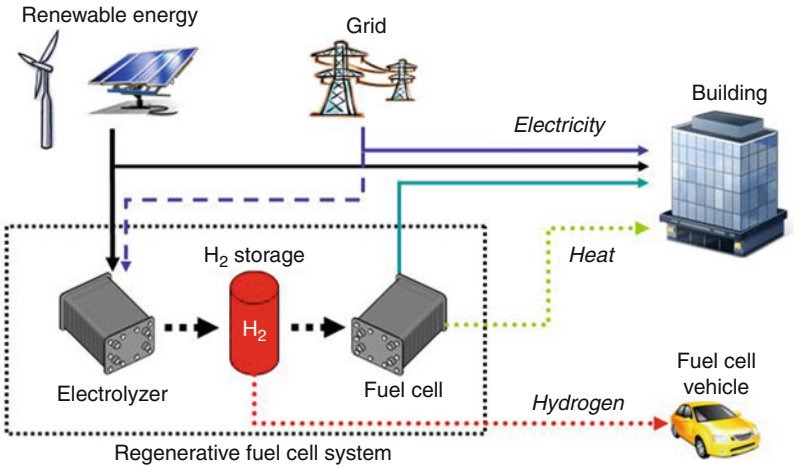

Regenerative Fuel Cells, Fig. 1 Renewable energy storage using a regenerative fuel cell system

energy [6]. The disadvantages are vulnerability to heat shock and long-term stability (lifetime), which limits the number of times the system can start-up/shutdown.

Low-temperature RFCs based on polymer electrolyte technology are operated at 60–80 °C and typically use H_2/O_2. The materials used in low-temperature RFCs are also similar to those in polymer electrolyte fuel cells and polymer electrolyte water electrolyzers. Perfluorinated membranes such as Nafion (DuPont) are typically used as an electrolyte. As catalyst materials, Pt is used for the hydrogen electrode, and Pt or a mixture of Pt/Ir/Ru metals or oxides is used for the oxygen electrode [7]. One of the advantages of low-temperature RFCs is the rapid start-up/shutdown of the system. The RFC system is operated alternately as a fuel cell and an electrolyzer, so that, in low-temperature RFCs, the restart time and standby power of the subunit that is not in operation can be reduced. The disadvantage is that low-temperature system are less efficient than high-temperature systems, which is mainly due to the higher polarization of oxygen electrode reactions and thermodynamic requirements. The overall efficiency of low-temperature RFCs can be significantly improved through the use of halogens, such as H_2/Cl_2 and H_2/Br_2, due to the greater reversibility of the redox reactions of halogens [8, 9]. However, the highly corrosive nature of halogen compounds is a major drawback. The overall efficiency can also be improved by using the waste heat from an RFC system, such as to supply hot water, by installing a cogeneration system, as shown in Fig. 1.

System Design and Potential Applications of RFC

In the basic design of an RFC, the system includes a dedicated (separate) fuel cell and electrolyzer, especially for low-temperature RFCs. Another possible design is the integration of the functions of a fuel cell and electrolyzer into a single electrochemical cell (unitized regenerative fuel cell, URFC). The advantages of a URFC are lower weight and volume, so that URFCs have been considered for space or military applications. In addition, URFCs have the potential advantage of a lower cost provided that electrochemical cells account for a significant portion of the system cost. On the other hand, the catalyst materials and electrode design must be balanced in a URFC. For example, the electrode should be flooded (hydrophilic) during electrolyzer mode but should be dry (hydrophobic) during fuel cell operation. The cathode material should be suitable for both anodic and cathodic reactions. This is an important issue especially for the oxygen electrode because redox reactions of oxygen are highly irreversible, which causes larger polarizations, as described above.

Examples of potential applications of RFCs are as follows:

- Energy storage for renewable energy sources [10]
- Energy storage for remote off-grid power sources [11]
- Energy storage for spacecraft [12]
- Stratospheric platform airship [13]
- High-altitude, long-endurance, solar-rechargeable aircraft [1].

Future Directions

RFCs may be able to offer high-density electrical energy storage. Therefore, in applications in which energy density is the first priority, advanced RFC system should be considered. However, the efficiency of energy conversion in RFCs is still inadequate compared to competing technologies such as secondary battery systems. To realize the commercialization of RFC energy storage system, low-cost, durable, and efficient materials for electrochemical cells (electrocatalysts, electrolyte, bipolar plate) and a lightweight system for hydrogen storage should be developed.

Cross-References

- ▶ Polymer Electrolyte Fuel Cells (PEFCs), Introduction
- ▶ Solid Oxide Fuel Cells, Introduction

References

1. Mitlitsky F, Myers B, Weisberg AH (1998) Regenerative fuel cell systems. Energy Fuel 12:56–71. doi:10.1021/ef970151w
2. Smith W (2000) The role of fuel cells in energy storage. J Power Sources 86:74–83. doi:10.1016/S0378-7753(99)00485-1
3. Barbir F, Molter T, Dalton L (2005) Efficiency and weight trade-off analysis of regenerative fuel cells as energy storage for aerospace applications. Int J Hydrogen Energ 30:351–357. doi:10.1016/j.ijhydene.2004.08.004
4. Bruce PG, Freunberger SA, Hardwick LJ, Tarascon JM (2012) Li-O_2 and Li-S batteries with high energy storage. Nat Mater 11:19–29. doi:10.1038/nmat3191
5. Hauch A, Ebbesen SD, Jensen SH, Mogensen M (2008) Highly efficient high temperature electrolysis. J Mater Chem 18:2331–2340. doi:10.1039/B718822F
6. Laguna-Bercero MA, Kilner JA, Skinner SJ (2011) Development of oxygen electrodes for reversible solid oxide fuel cells with scandia stabilized zirconia electrolytes. Solid State Ionics 192:501–504. doi:10.1016/j.ssi.2010.01.003
7. Ioroi T, Kitazawa N, Yasuda K, Yamamoto Y, Takenaka H (2000) Iridium oxide/platinum electrocatalysts for unitized regenerative polymer electrolyte fuel cells. J Electrochem Soc 147:2018–2022. doi:10.1149/1.1393478
8. Rugolo J, Huskinson B, Aziz MJ (2012) Model of performance of a regenerative hydrogen chlorine fuel cell for grid-scale electrical energy storage. J Electrochem Soc 159:B133–B144. doi:10.1149/2.030202jes
9. Kreutzer H, Yarlagadda V, Nguyen TV (2012) Performance evaluation of a regenerative hydrogen-bromine fuel cell. J Electrochem Soc 159:F331–F337. doi:10.1149/2.086207jes
10. Maclay JD, Brouwer J, Samuelsen GS (2006) Dynamic analysis of regenerative fuel cell power for potential use in renewable residential applications. Int J Hydrogen Energ 31:994–1009. doi:10.1016/j.ijhydene.2005.10.008
11. Agbossou K, Chahine R, Hamelin J, Laurencelle F, Anouar A, St-Arnaud JM, Bose TK (2001) Renewable energy systems based on hydrogen for remote applications. J Power Sources 96:168–172. doi:10.1016/S0378-7753(01)00495-5
12. Sone Y (2011) A 100-W class regenerative fuel cell system for lunar and planetary missions. J Power Sources 196:9076–9080. doi:10.1016/j.jpowsour.2011.01.085
13. Eguchi K, Fujihara T (2003) Research progress in solar powered technology for SPF airship. NAL Res Prog 2002–2003:6–9

Role of Separators in Batteries

Daniel Steingart
Department of Mechanical and Aerospace Engineering, Andlinger Center for Energy, the Environment Princeton University, Princeton, NJ, USA

Introduction

Within a battery the active components, that is, the electrodes, electrolytes, and current collectors, receive the majority of attention in the

literature. The inert components of a battery, that is the casing but more importantly the separator, however, play a critical role what they allow and what they do not allow. Without binder particulate electrodes would not stay together; without a case the battery would have no protection from its environment; and without a mechanical separation between anode and cathode, there would be no impetus for current to be created through an electrochemical reaction as the active material materials would simply undergo a mutually passivating redox reaction (Fig. 1).

Unsung players, these materials must prevent short circuits while maximizing the cross section for ionic transport [1–5]:

1. Provide reliable and high porosity through its bulk to transport current in the form of ions between electrodes
2. Have sufficient, unchanging surface porosity at electrodes to allow even distribution of ion and therefore reaction current at the electrode
3. Physically separate the electrodes for the lifetime of the battery
4. Be an electronic insulator
5. Be wetted by an electrolyte without swelling
6. Be as uniform as possible
7. Prevent sediment (e.g., precipitated electrolyte salts, fractured electrode materials) from migrating across the cell and/or blocking electrode reaction sites.

The separator must serve this purpose in a dynamic environment. Electrodes can change shape and/or volume as a function of age and cycle number; electrolytes can age triggering precipitation. The separator must be considered and matched to its system so that it can provide the aforementioned functionality for the design life of the system. Figure 2 indicates the workhorse design of perhaps the most ubiquitous battery and separator material, the zinc-alkaline primary system.

The separator region should be as thin as possible without risking short circuits in a practical cell. The minimum electrolyte distance is limited by the unevenness of the electrode surfaces. Because electrode surfaces will change and deform over time, the electrolyte must be engineered to properly accept such change if the cell is to be safe and maximize its cycle life.

An electrolyte can be "too thick" as well. Again, thicker electrolytes are linearly more resistive, so for high-power cells the electrolyte resistance can lead to significant heating of a cell. In older lithium ion cells, this can trigger "thermal runaway." Thus, an electrolyte should

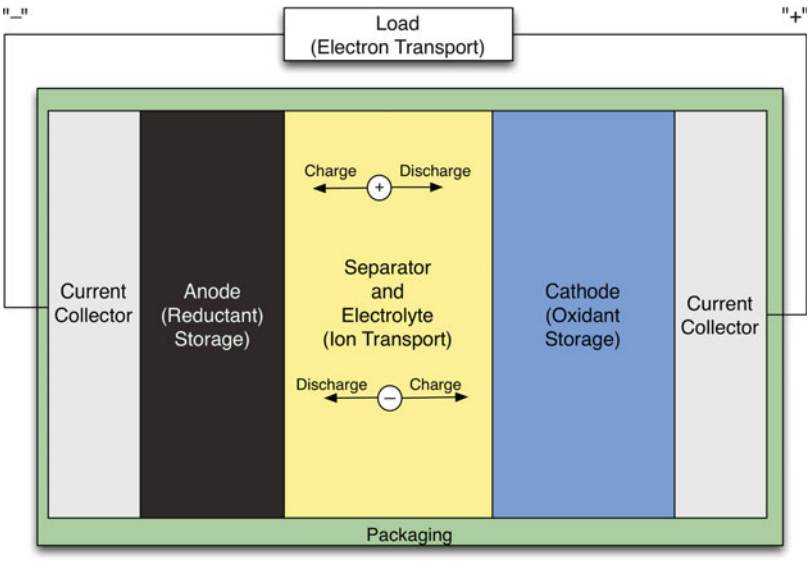

Role of Separators in Batteries, Fig. 1 Basic schematic of a closed electrochemical energy storage cell

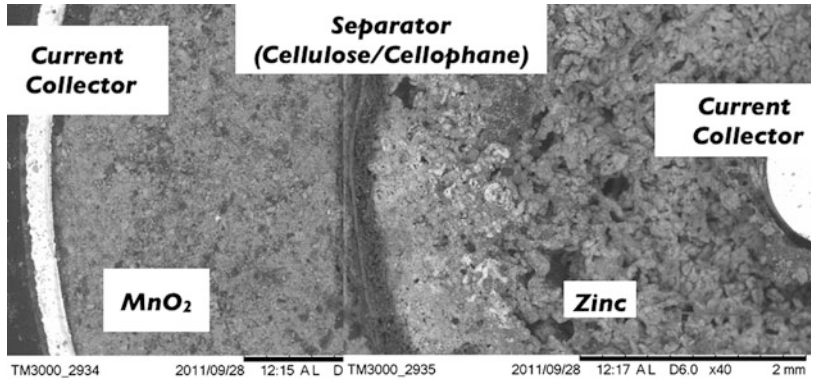

Role of Separators in Batteries, Fig. 2 Cross section of an AA Zinc-MnO_2 battery

be as thin as possible to maximize potential efficiency and minimize overheating.

This brief chapter will consider some material challenges across aqueous, aprotic, and high-temperature systems as a start for the reader's consideration of separators. This is by no means an attempt at an exhaustive approach, and so long as there are new battery electrodes and electrolytes, there will be new challenges for separator materials to meet. We will begin with a brief overview of battery separator materials and then consider design challenges for the lead acid, alkaline, lithium ion and molten metal battery systems. Not considered here are in any depth beyond this sentence are "overloaded" ion-conducting membranes such as proton exchange membranes (PEM), as well as O^{2+} conductors for high-temperature fuel cells: these systems combine the mechanical requirements of the separator with the ion transport requirements of the electrolyte. These systems typically have pore sizes on the order of 2 nm [6].

Separator Materials

Separator materials, first and foremost, need to be completely nonreactive and minimally interactive with the electrolyte they host. By minimally interactive, this is the razor's edge of not swelling significantly in the presence of an electrolyte (swelling indicates eventual mechanical degradation) while also being completely wetting within the electrolyte [4, 5, 7].

Lead acid battery separator materials have progressed significantly over the history of this workhorse chemistry and is a good indicator of the arrow of progress of the entire field. The first lead acid separators were natural rubbers that had moderate porosity (~55–65 %) with more sizes on the order of 1–10 μm. These separators were on the order of 500 μm thick. These systems suffered aging and embrittlement problems, and the separator was often the point of failure for these batteries. The next generation of separators for lead acid batteries were engineered cellulosic materials. These systems were actually worse mechanically than the original rubber systems, but had significantly better porosity and lower thicknesses, effectively halving the ohmic resistance with an equivalent electrolyte composition. This system was optimized for higher current density at lower cost; the aging disadvantage was an acceptable trade-off at the time.

The advent of engineered polymer brought a step change to the lead acid separator. With polyvinyl chloride systems, pore sizes decreased slightly compared to the cellulose-based systems, but the thickness deceased as much, and the mechanical and chemical stability of these systems improved markedly as well. As a result separators were no longer the age-limiting mechanisms for lead acid batteries, and conductivity effectively doubled again. Polyethylene systems improved the overall porosity to levels previously realized by natural rubber systems while maintaining the mechanical advantages of PVC. The next and final step change to lead acid separators was a move from engineered polymers

to engineered glasses. In these systems the porosity skyrocketed to up to 95 % and the conductivity of the electrolyte doubled again, all while maintaining the mechanical advantages of the engineered polymers. What this meant for the industry now is that a lead acid separator could be 10 times as thick as the original rubber separators (a condition which could allow for mass transport and mixing parallel to the electrode faces, while still maintaining a lower electrolyte conductivity.

In the current era lithium ion separators have gone through a similar engineering trajectory, and most systems now are either PE, PP, PvDF, polyolefin, or composites thereof with [5, 8, 9], engineered to be resistant to chemical attack by aprotic electrolytes. For alkaline systems, PP and PVA are analogous systems. Additionally, the low cost and abundance of both cellophane and cellulose make it an attractive choice of separator for low-cost zinc-alkaline primary cells.

Finally, high-temperature molten salt electrolyte batteries (NaS, Zebra) require completely inorganic separators capable of withstanding liquid metal temperature and chemical attack, effectively acidic conditions at temperatures >200 °C. Beta-Al_2O_3 has been significantly engineered to serve this role [10].

Structure of Separators

Beyond the materials development, the morphology induced by processing a given separator is a critical aspect of the separators performance. What follows is a brief summary of separators structure as enumerate by Arora [5]. Microporous separators can be manufactured from any of the above materials. Specifically, nonwoven separators (colloquially referred to as "nonwovens") are fibers of a given materials that are laid and processed in a dry method (perhaps a sintered mat) or a wet bonding process very similar to that of paper. The processing of the fibers can be exploited to provide or enhance mechanical or wetting properties [8].

Separators can also be made directly from solution-processed and/or cross-linked methods. Polyvinylidene difluoride (PVdF) is a popular choice for this approach because it can, when processed directly on an electrode containing a PVdF binder, form an excellent electrode/electrolyte interface (Fig. 2). These systems can also be cast and processed with ionic conductors "built in" in the form of gels or ion-conducting backbones. Such a system is shown in Fig. 3 [8, 11].

Given the constraints of a given materials system, the choice between cast or nonwovens, and methods of processing within these systems, is driven by the many, and often diametrically, opposed needs of a given system.

Design Considerations for Individual Systems

The devil is the in the details, and the choice of materials compatibility is insufficient to match a separator system to a battery chemistry. In this section we will briefly outline design issues and their solutions to a few different chemistries. This is intended to serve as guiding examples for the reader's own selection process of a separator material and system design.

Lead Acid Batteries

Lead acid batteries pose the following challenges to a separator. Both anode and cathode are subject to shape change and possible embrittlement, so the separator must be compliant enough to accommodate this type of change while also preventing material crossover. Electrolyte stratification is a significant issue for certain types of lead acid systems, so the pores must be big enough to accommodate natural or forced convection to "refresh" the electrolyte. In other lead acid systems, the generation and recombination of gas is critical to the operation of the cell, so the separator must allow these gases to recombine if need be.

The astute reader will note that the above constraints are at cross-purposes: flow must be maximized but particle transport must be minimized. As a result the following general practices take place. Depending on the specific lead acid system, either a PE or microglass separator will

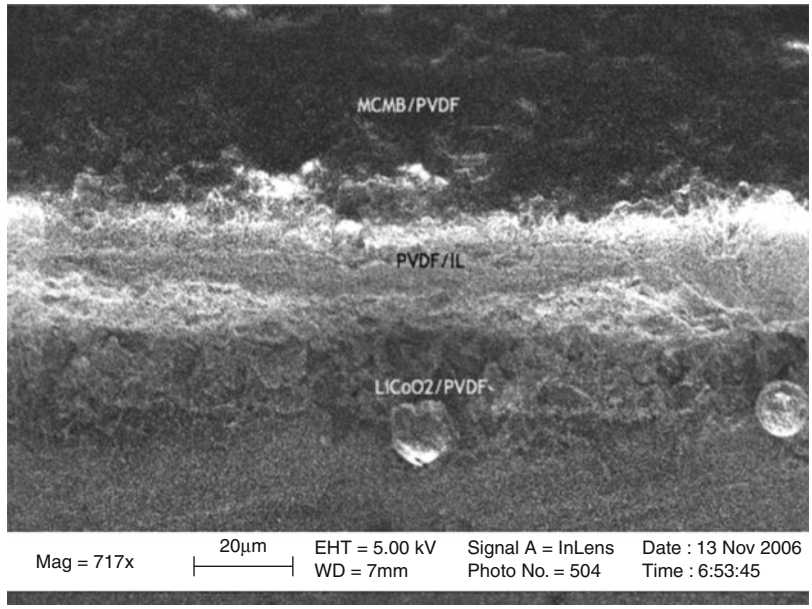

Role of Separators in Batteries, Fig. 3 A fully printed PVdF IL electrolyte gel from [11]

be used to minimize crossover or maximize flow. In certain system, composites of the two are employed where small porosity layers are used near the electrode to catch embrittled, cracked electrodes, and larger pores are used to catch allow for electrolyte convection.

Zinc-Alkaline Batteries

With zinc-alkaline batteries the separator must accommodate yet suppress the ramification of zinc upon cycling, while also preventing the formation of thick zinc oxide layers on the zinc electrode. This has led to the use of cellophane laminated to something like PE, to achieve a similar effect to the shape change prevention in the aforementioned lead acid cells.

Lithium Ion Batteries

As of this writing no commercial separator is reliable enough to prevent a lithium metal dendrite or ramification from short circuiting a cell upon charge. Due to the danger of this condition, lithium metal is never, or never in the author's knowledge, used as a secondary battery. Within lithium ion cells, however, the effect of shape change of an electrode is still an issue with graphitic carbon undergoing volume changes up to 30 % and silicon electrodes up to 400 % [3].

Beyond shape change, lithium ion cells have be designed to retard the inherent flammability of most high-performance aprotic electrolytes as well as the ignition danger of high-performance anodes and cathodes in overcharge or over-current and over-temperature conditions. Commercial separators [5] have been designed with a specific melting point (typically just above 130 °C), which when reached will cause porosity within the cell to diminish significantly. This porosity decrease has been shown to very quickly increase the resistance of a given electrolyte up to four orders of magnitude, effectively stopping any further reaction. This mechanism has been tested successfully against overcharge, over-temperature, mechanical intrusion (the "nail test"), and over-current conditions [5]. While not a guarantee against all fires, this separator shutdown design significantly reduces the threat of explosion in an off condition.

Conclusions and Further Readings

While not a formally *required* aspect of electrochemical energy storage devices or fuel cells, separators are an enabling technology that has shown above can greatly improve the power

performance, cycle lifetime, and safety aspects of a battery. The students interested in this field should know that a separator can never be "too good" and that the industry will always appreciate further improvements in porosity, stability, safety, and costs. The reader is directed to the references following this review for deeper analysis.

Cross-References

► Primary Battery Design

References

1. Peabody C, Arnold CB (2011) The role of mechanically induced separator creep in lithium-ion battery capacity fade. J Power Sources 196:8147–8153. doi:10.1016/j.jpowsour.2011.05.023
2. Brodd RJ (2012) Batteries for sustainability. Springer, New York
3. Besenhard JO (1999) Handbook of battery materials. In: Besenhard JO (ed) Handbook of battery materials. Wiley-VCH, New York, p 648. ISBN 3-527-29469-4
4. Linden D, Reddy TB (2002) Handbook of batteries. McGraw-Hill Professional, New York
5. Arora P, Zhang ZJ (2004) Battery separators. Chem Rev 104:4419–4462. doi:10.1021/cr020738u
6. Agrawal RC, Pandey GP (2008) Solid polymer electrolytes: materials designing and all-solid-state battery applications: an overview. J Phys D: Appl Phys 41:223001. doi:10.1088/0022-3727/41/22/223001
7. Leung P, Li X, de León CP et al (2012) Progress in redox flow batteries, remaining challenges and their applications in energy storage. RSC Adv 2:10125–10156
8. Mehta V, Cooper JS (2003) Review and analysis of PEM fuel cell design and manufacturing. J Power Sources 114:32–53. doi:10.1016/S0378-7753(02)00542-6
9. Huang Z-M, Zhang YZ, Kotaki M, Ramakrishna S (2003) A review on polymer nanofibers by electrospinning and their applications in nanocomposites. Compos Sci Technol 63:2223–2253. doi:10.1016/S0266-3538(03)00178-7
10. Lu X, Xia G, Lemmon JP, Yang Z (2010) Advanced materials for sodium-beta alumina batteries: status, challenges and perspectives. J Power Sources 195:2431–2442. doi:10.1016/j.jpowsour.2009.11.120
11. Steingart D, Ho CC, Salminen J et al (2007) Dispenser printing of solid polymer-ionic liquid electrolytes for lithium ion cells. IEEE Polytronics, Vol. 1, pp 1:261–264

Ruthenium Oxides as Supercapacitor Electrodes

Wataru Sugimoto
Faculty of Textile Science and Technology, Shinshu University, Nagano, Japan

Background

Since the pioneering work by Trasatti and Buzzanca [1], the first to recognize that the "rectangular"-shaped cyclic voltammogram of a RuO_2 film (Fig. 1) resembled that of the carbon-based electric a double-layer capacitor, RuO_2 has attracted interest as a model system for the fundamental understanding of pseudocapacitive behavior of oxide electrodes as well as practical application towards high rate, lightweight, and small energy harvesting devices. The difference to an ideally polarizable electrode system is that there is some surface oxidation/reduction occurring in addition to the non-Faradaic electrical double-layer charging, which, in contrast to reactions occurring in batteries, is limited to a monolayer or a few layers on the electrode surfaces. For these systems, the electrode potential varies almost linearly with surface coverage, that is, with the charge passed during the reaction (similar to an electrical double-layer capacitor). The kinetics of such surface and near surface redox reactions are extremely fast and exhibits reversible or pseudo-reversible behavior. Consequently, the device behaves like an electrochemical double-layer capacitor with redox contribution, hence the termination and concept "pseudocapacitor."

Hydrous ruthenium oxide ($RuO_2 \cdot xH_2O$) nanoparticles represent one of the best-known electrode materials for aqueous supercapacitors providing high specific capacitance ranging from a few hundred to ~1,000 F g^{-1}. The high gravimetric and volumetric capacitance of RuO_2-based electrodes is appealing, especially where size and weight is taken more seriously than cost issues such as low-voltage miniaturized devices and other high value-added devices [2–4].

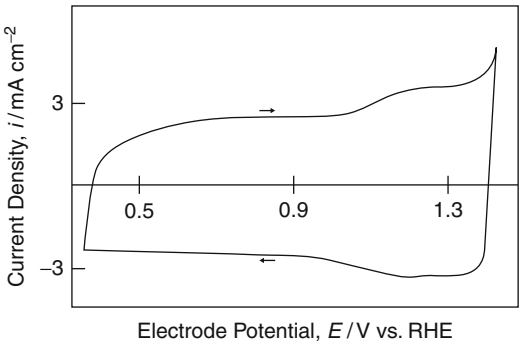

Ruthenium Oxides as Supercapacitor Electrodes, Fig. 1 A typical cyclic voltammogram of RuO_2 electrode in 1 M $HClO_4$ at 40 mV s^{-1} [1]

The weakness of RuO_2-based electrodes, besides its lack of abundance and cost, is that these electrodes perform better in aqueous compared to nonaqueous electrolytes, limiting the voltage window to about 1.0–1.2 V.

The study of hydrous RuO_2 nanoparticles prepared by a sol–gel method instituted a major progress in terms of gravimetric capacitance [5, 6], activating a worldwide surge in the study of RuO_2-based electrodes for electrochemical capacitor application. Much effort has since been devoted to research and development with particular emphasis on structure–property relations. Higher capacitance and enhanced power capability has been achieved by material design, and sophisticated characterization methods have contributed to the understanding of the Faradaic behavior of RuO_2-based electrodes. Owing to such extensive studies, the fundamental charge storage properties of RuO_2 are now much better understood.

The theoretical redox capacitance of $RuO_2 \cdot xH_2O$ is often calculated from the equation,

$$C_{\text{redox}} = \frac{nF}{m\Delta V} \quad (1)$$

where m is the molar mass of $RuO_2 \cdot xH_2O$, F is the Faraday constant 96,485 C mol^{-1}, and n is the number of electrons involved in the reaction within the potential window, ΔV [5–12]. A C_{redox} value of 1,358 F g^{-1} can be deduced for $RuO_2 \cdot 0.5H_2O$ assuming that all of the Ru atoms of the material change its oxidation state from Ru^{2+} to Ru^{4+} within a 1.0 V potential window [7, 13]. The C_{redox} is 970 F g^{-1} if the potential range is 1.4 V [5]. If a 4-electron reaction is assumed within a 1.35 V window, then the value exceeds 2,000 F g^{-1} [9, 14]. Note that in the above calculations, it is assumed that all of the Ru atoms in the crystallite are involved in the reaction (bulk reaction) and that Ru can take a number of oxidation states, which seems to be an overestimation based on various studies. It should also be kept in mind that this calculation neglects the contribution from the electric a double-layer capacitance C_{dl}.

The theoretical value of the electric a double-layer capacitance C_{dl} of RuO_2 is somewhat a controversial matter. Most of the C_{dl} values reported in literature for RuO_2-based electrodes are larger than the value for a mercury electrode in a diluted aqueous electrolyte solution, which is $C_{\text{dl}} \sim 20$ μF cm^{-2}. It is quite challenging to experimentally differentiate between the contribution from the electric a double-layer capacitance C_{dl} and redox-related Faradaic capacitance C_{redox}, as the (surface) redox-related pseudocapacitance for RuO_2 is a fast and reversible process [15]. The most widely reported value is 80 μF cm^{-2} [15–18]. Using this value as a probe, one can deduce the theoretical C_{dl} for a 1 nm RuO_2 particle as 680 F g^{-1}. In the case of hydrous RuO_2 with gravimetric capacitance ~700 F g^{-1}, area-specific capacitance as high as 1,000 μF cm^{-2} has been reported using BET surface area [5, 6]. Such unusually high area-specific capacitance may be a result of a mixture of the non-Faradaic electric a double-layer capacitance and Faradaic redox-related processes. The surface area of hydrous oxides may also be underestimated by N_2 adsorption measurements depending on the pretreatment.

Synthesis, Chemical, and Physical Properties

The specific capacitance, as well as the cycle and rate performance, is affected by the various

parameters including particle size and porosity (electrochemically accessible surface area), crystal structure, water content, etc., which will vary as a result of the different preparation procedures and measurement conditions reported by numerous groups [1, 5, 6, 19–33]. Porous RuO_2 films can be prepared by pyrolysis of ruthenium precursors coated on a conducting substrate by dip coating or spraying, which are the processes adopted for the well-known dimensionally stable electrodes used in industrial electrolysis. The films are typically heat treated at moderately high temperature (450–550 °C) to prepare well-crystalline material that can withstand tortuous gas evolution with crystallite size in the range of 20–50 nm in diameter. Smaller, high-surface area RuO_2 nanoparticles can be obtained by soft-solution processing methods including chemical reduction of RuO_4 [34], precipitation from various precursors [35], sol–gel reactions [5, 6, 36], etc. Electrochemical methods such as electrooxidation of Ru metal [23, 24, 37–48] and electrodeposition [49–57] have also been applied. Heat treatment at relatively low temperatures (150 ~ 200 °C) is often necessary to convert all Ru ions to the electrochemically stable Ru^{4+} state while maintaining small particle size. Mesoporous RuO_2 via soft and hard template synthesis has also been conducted [58].

Synthesis of RuO_2-MO_x composites and A_xRuO_y complex oxides is a classical approach to increase the utilization of RuO_2. Binary rutile-type $(Ru,M)O_2$ (M = Sn^{4+}, Ti^{4+}, V^{4+}, Mo^{4+} etc.), pyrochlore-type $A_2Ru_2O_7$, and perovskite-type $ARuO_3$ are typical examples [59–67]. Many studies have focused on preparing composites with carbonaceous materials, including activated carbon [7–9], carbon black [10, 11, 68, 69], carbon nanotubes [11, 70–81], and more recently reduced graphite oxide [82–87]. Carbon-supported RuO_2 materials can be prepared by impregnation or colloidal methods [10, 88, 89]. Even a simple physical mixture of acetylene black and sol–gel-derived hydrous RuO_2 can drastically improve the rate performance, where the carbon black helps to increase porosity to supply extra pores for electrolyte permeation [19].

High capacitance can also be achieved by using a water-swellable layered structure or by exfoliation of the layered structure into elemental nanosheets. Specific capacitance of ~400 F g^{-1} has been accomplished by using layered RuO_2 as the electrode material [90, 91]. The capacitance is exceptionally large considering the large micrometer size of the particles, which has been attributed to the ability of the interlayer to swell thereby allowing electrolyte permeation into the two-dimensional structure. RuO_2 nanosheet electrodes provide even higher capacitance, reaching ~700 F g^{-1}. These two-dimensional materials exhibit unique electrochemical properties with remarkably large contribution from pseudocapacitance (as much as 50 %) [90, 91].

Charge Storage Mechanism

The cyclic voltammograms of hydrous RuO_2 heat treated at suitable temperatures are featureless and principally rectangular in shape in comparison to as-prepared or well-annealed material (Fig. 2). At heat-treatment temperatures below 150 °C, poor *i-E* response is observed particularly in the low potential region, which has been associated to the presence of Ru^{3+}. Considerable capacitance fading occurs for such non-optimized conditions, most likely due to the presence of soluble Ru species [35].

The fast and slow charges in thermally prepared RuO_2/Ti DSA-type electrodes have been attributed to the utilization of more accessible, mesoporous surfaces and less accessible, microporous inner surfaces, respectively [92]. Based on ellipsometry and ac impedance measurements on anodically and thermally prepared RuO_2, the fast- and slow-charging modes have been ascribed to the charging of the grain surfaces and incorporation of protons into the oxide grains, respectively [93]. Similar conclusions were derived by CV and CA measurements of anhydrous RuO_2 nanoparticles [15].

Various models have been proposed to explain the reasoning behind the observed maximum capacitance and power capability of sol–gel-derived hydrous RuO_2 as a function of

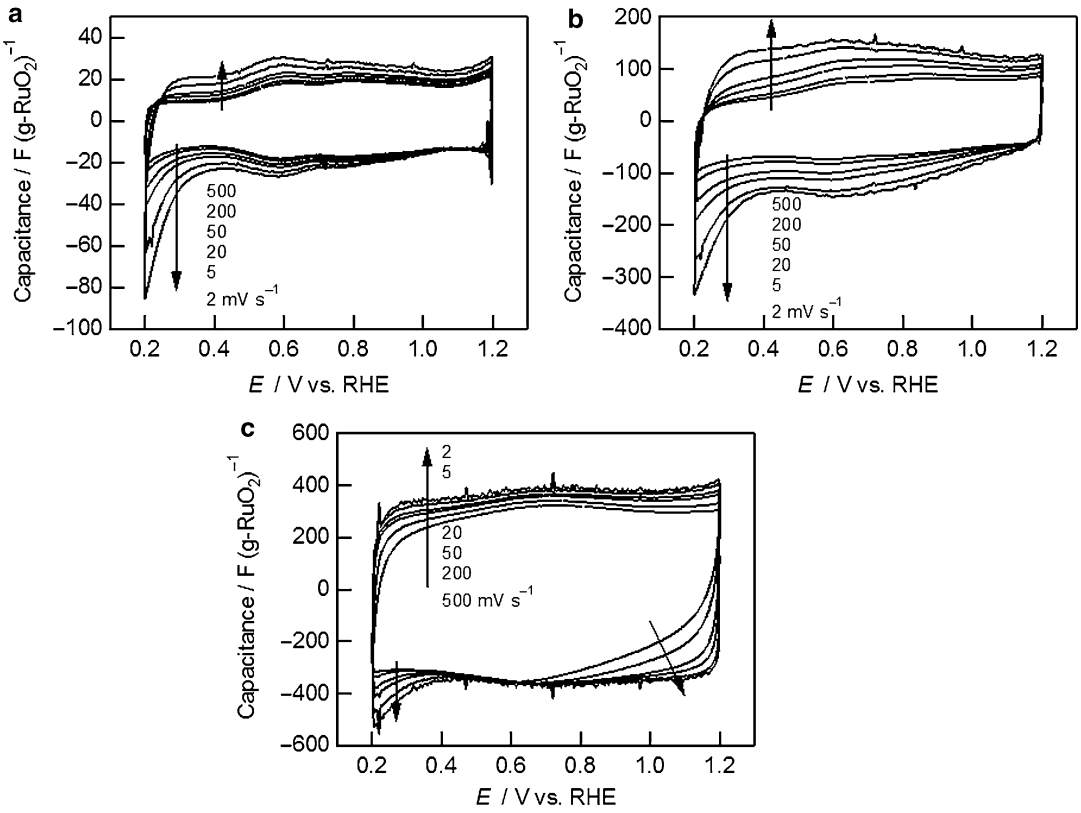

Ruthenium Oxides as Supercapacitor Electrodes, Fig. 2 Typical cyclic voltammograms of $RuO_2 \cdot nH_2O$ in 0.5 M H_2SO_4 with $n =$ (**a**) 0, (**b**) 0.3, and (**c**) 0.5 [33]

the heat-treatment temperature. The cluster-sized particles for low-temperature annealed hydrous RuO_2 afford high capacitance due to large surface area at the expense of power performance. Zheng et al. studied the interaction between the structural water and the rutile crystals by measuring the proton dynamics of hydrous RuO_2 using solid-state proton nuclear magnetic resonance (H-NMR) spectroscopy [28]. A maximum in proton activation energy was observed when the hydrous RuO_2 exhibited the maximum capacitance revealing the correlation between the proton mobility and the charge storage (Fig. 3) [28]. An optimum mixed percolation conduction mechanism has also been proposed to explain the volcano-plot behavior [31]. In addition to the relation between the maximum capacitance and water content in hydrous RuO_2, Sugimoto et al. derived a similar model based on electrochemical impedance spectroscopy to explain the frequency response [33]. It was suggested that the frequency response (power capability) was dominated by proton conduction within the hydrated micropores between the RuO_2 nanocrystallites. Kötz et al. reached similar conclusions based on X-ray photoelectron spectroscopy (XPS) studies [94] revealing two types of water in hydrous RuO_2: weakly bound physically adsorbed water and strongly bound chemically bound water. The chemically bound water was correlated to the heat-treatment temperature and increase in particle size. It has also been shown that the initial hydrous nature is not a prerequisite for the high capacitance [27]. X-ray absorption near-edge structure (XANES) and atomic pair-density function (PDF) analysis of synchrotron X-ray scattering measurements on a series of hydrous RuO_2 treated at different temperatures have revealed that hydrous RuO_2 is composed of disordered rutile-like RuO_2 nanocrystals

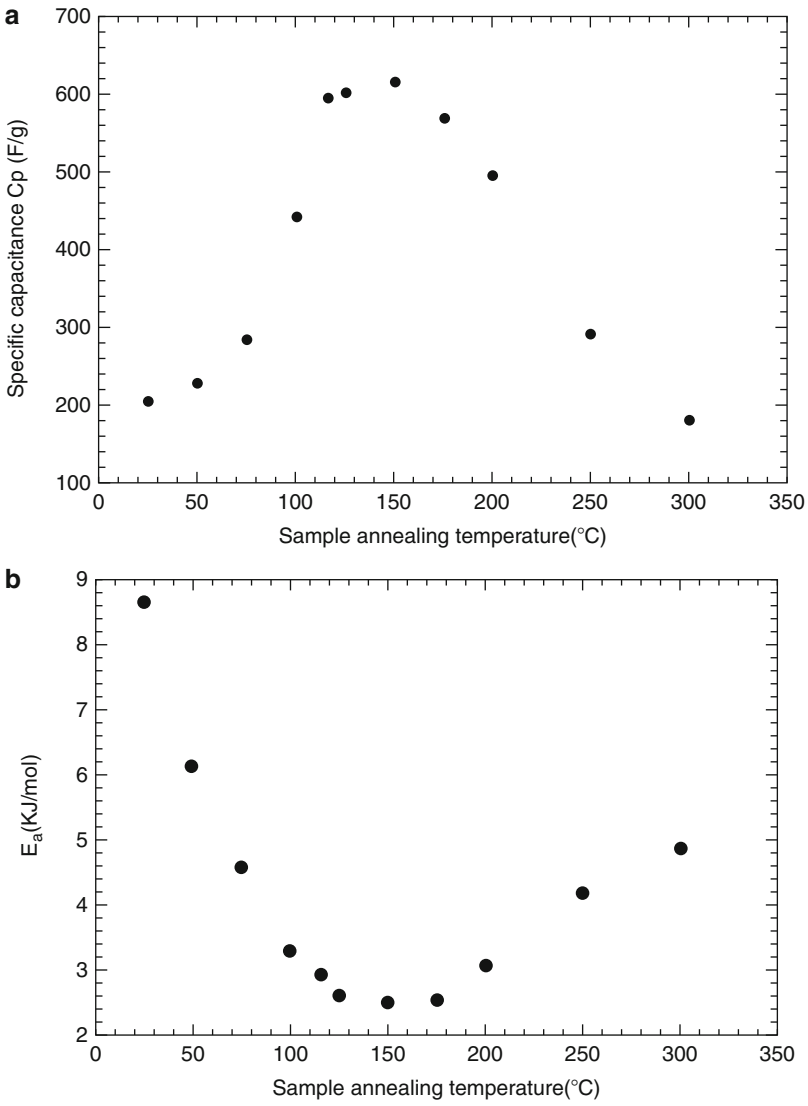

Ruthenium Oxides as Supercapacitor Electrodes, Fig. 3 (**a**) Specific capacitance and (**b**) apparent proton activation energy determined from H-NMR of the $RuO_2 \cdot H_2O$ as a function of the sample annealing temperature [28]

dispersed by boundaries of structural water, in contrast to the apparent amorphousness measured with conventional XRD [22, 31]. A parallel electron-proton conduction model, where the rutile-like RuO_2 nanocrystals support electronic conduction and structural water as the boundaries transport protons, was proposed to account for the maximum capacitance of $RuO_2 \cdot xH_2O$ at $x \sim 0.5$ (Fig. 4) [31].

In situ techniques have also been exploited to realize the effect of the heat-treatment temperature on the charge storage capability of ruthenium oxide. In situ XPS and XRD data gives evidence that no bulk reduction of anhydrous RuO_2 occurs until the electrode is polarized at potentials where hydrogen evolution occurs [95–97]. In situ resistivity measurements of anhydrous RuO_2 have shown that the resistivity is independent of potential within the hydrogen and oxygen evolution region, complementing the in situ XPS and XRD data showing that bulk reduction of Ru^{4+} does not take place in the potential region relevant to electrochemical capacitor applications [98]. Ru^{4+} reduction to Ru^{3+} has been shown to occur only below $E < 0.4$ V by in situ EXAFS and XANES [46, 99–101]. The reduction of Ru^{4+}

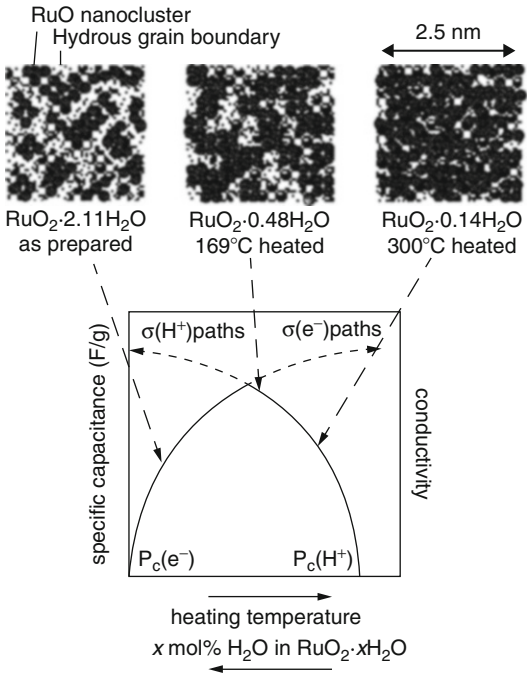

Ruthenium Oxides as Supercapacitor Electrodes, Fig. 4 Schematic illustration of the variation of the percolation volumes of the RuO_2 nanocrystals and the hydrous grain boundaries with changes in water content [31]

for the case of hydrous RuO_2 leads to a prominent change in resistivity as a function of the potential, in contrast to the case of anhydrous RuO_2 [98].

Cross-References

► Electrical Double-Layer Capacitors (EDLC)

References

1. Trasatti S, Buzzanca G (1971) Ruthenium dioxide: a new interesting electrode material. Solid state structure and electrochemical behaviour. J Electroanal Chem Interfacial Electrochem 29:A1–A5
2. Arnold CB, Wartena RC, Swider-Lyons KE, Pique A (2003) Direct-write planar microultracapacitors by laser engineering. J Electrochem Soc 150:A571
3. Sugimoto W, Yokoshima K, Ohuchi K, Murakami Y, Takasu Y (2006) Fabrication of thin-film, flexible, and transparent electrodes composed of ruthenic acid nanosheets by electrophoretic deposition and application to electrochemical capacitors. J Electrochem Soc 153:A255
4. Liu C-C, Tsai D-S, Susanti D, Yeh W-C, Huang Y-S, Liu F-J (2010) Planar ultracapacitors of miniature interdigital electrode loaded with hydrous RuO_2 and RuO_2 nanorods. Electrochim Acta 55:5768–5774
5. Zheng JP, Cygan PJ, Jow TR (1995) Hydrous ruthenium oxide as an electrode material for electrochemical capacitors. J Electrochem Soc 142:2699–2703
6. Zheng JP, Jow TR (1995) A new charge storage mechanism for electrochemical capacitors. J Electrochem Soc 142:L6–L8
7. Zhang J, Jiang D, Chen B, Zhu J, Jiang L, Fang H (2001) Preparation and electrochemistry of hydrous ruthenium oxide/active carbon electrode materials for supercapacitor. J Electrochem Soc 148:A1362
8. Ramani M, Haran BS, White RE, Popov BN, Arsov L (2001) Studies on activated carbon capacitor materials loaded with different amounts of ruthenium oxide. J Power Sources 93:209–214
9. Hu C-C, Chen W-C, Chang K-H (2004) How to achieve maximum utilization of hydrous ruthenium oxide for supercapacitors. J Electrochem Soc 151: A281
10. Kim H, Popov BN (2002) Characterization of hydrous ruthenium oxide/carbon nanocomposite supercapacitors prepared by a colloidal method. J Power Sources 104:52–61
11. Park JH, Ko JM, Park O (2003) Carbon nanotube/RuO_2 nanocomposite electrodes for supercapacitors. J Electrochem Soc 150:864
12. Min M, Machida K, Jang JH, Naoi K (2006) Hydrous RuO_2/carbon black nanocomposites with 3D porous structure by novel incipient wetness method for supercapacitors. J Electrochem Soc 153:A334
13. Lin C, Ritter JA, Popov BN (1999) Development of carbon-metal oxide supercapacitors from Sol-Gel derived carbon-ruthenium xerogels. J Electrochem Soc 146:3155
14. Hu C, Chen W (2004) Effects of substrates on the capacitive performance of RuOxanH_2O and activated carbon-RuOx electrodes for supercapacitors. Electrochim Acta 49:3469–3477
15. Sugimoto W, Kizaki T, Yokoshima K, Murakami Y, Takasu Y (2004) Evaluation of the pseudocapacitance in RuO_2 with a RuO_2/GC thin film electrode. Electrochim Acta 49:313–320
16. Siviglia P, Daghetti A, Trasatti S (1983) Influence of the preparation temperature of Ruthenium dioxide on its point of zero charge. Colloids Surf 7:15–27
17. Burke LD, Murphy OJ (1979) Cyclic voltammetry as a technique for determining the surface area of RuO_2 electrodes. J Electroanal Chem Interfacial Electrochem 96:19–27
18. Burke LD, Murphy OJ (1980) Surface area—Voltammetric charge correlation for RuO_2/TiO_2-based anodes. J Electroanal Chem Interfacial Electrochem 112:39–50

19. Zheng, J. P. Ruthenium Oxide-Carbon Composite Electrodes for Electrochemical Capacitors. Electrochem. Solid-State Lett. 1999, 2, 359.
20. Zheng JP, Jow TR (1996) High energy and high power density electrochemical capacitors. J Power Sources 62:155–159
21. Jow TR, Zheng JP (1998) Electrochemical capacitors using hydrous ruthenium oxide and hydrogen inserted ruthenium oxide. J Electrochem Soc 145:49
22. McKeown DA, Hagans PL, Carette LPL, Russell AE, Swider KE, Rolison DR (1999) Structure of hydrous ruthenium oxides: implications for charge storage. J Phys Chem B 103:4825–4832
23. Vukovic M, Cukman D (1999) Electrochemical quartz crystal microbalance study of electrodeposited ruthenium. J Electroanal Chem 474:167–173
24. Hu C-C, Huang Y-H (1999) Cyclic voltammetric deposition of hydrous ruthenium oxide for electrochemical capacitors. J Electrochem Soc 146:2465
25. Long JW, Swider KE, Merzbacher CI, Rolison DR (1999) Voltammetric characterization of ruthenium oxide-based aerogels and other RuO_2 solids: the nature of capacitance in nanostructured materials. Langmuir 15:780–785
26. Fang QL, Evans DA, Roberson SL, Zheng JP (2001) Ruthenium oxide film electrodes prepared at Low temperatures for electrochemical capacitors. J Electrochem Soc 148:A833
27. Kim I-H, Kim K-B (2001) Ruthenium oxide thin film electrodes for supercapacitors. Electrochem Solid-State Lett 4:A62
28. Fu R, Ma Z, Zheng JP (2002) Proton NMR and dynamic studies of hydrous ruthenium oxide. J Phys Chem B 106:3592–3596
29. Zheng JP, Xin Y (2002) Characterization of RuO_2•H_2O with various water contents. J Power Sources 110:86–90
30. Long JW, Ayers KE, Rolison DR (2002) Electrochemical characterization of high-surface-area catalysts and other nanoscale electroactive materials at sticky-carbon electrodes. J Electroanal Chem 522:58–65
31. Dmowski W, Egami T, Swider-Lyons KE, Love CT, Rolison DR (2002) Local atomic structure and conduction mechanism of nanocrystalline hydrous RuO_2 from X-ray scattering. J Phys Chem B 106:12677–12683
32. Sugimoto W, Iwata H, Murakami Y, Takasu Y (2004) Electrochemical capacitor behavior of layered ruthenic acid hydrate. J Electrochem Soc 151: A1181
33. Sugimoto W, Iwata H, Yokoshima K, Murakami Y, Takasu Y (2005) Proton and electron conductivity in hydrous ruthenium oxides evaluated by electrochemical impedance spectroscopy: the origin of large capacitance. J Phys Chem B 109:7330–7338
34. Swider-Lyons KE, Love CT, Rolison DR (2005) Selective Vapor Deposition of Hydrous RuO2 Thin Films. J Electrochem Soc 152:C158
35. Chang K-H, Hu C-C (2004) Oxidative Synthesis of RuOx·nH2O with Ideal Capacitive Characteristics for Supercapacitors. J Electrochem Soc 151:A958
36. Murakami Y, Tsuchiya S, Yahikozawa K, Takasu Y (1994) Preparation of ultrafine RuO2 and IrO2 particles by a sol-gel process. J Mater Sci Lett 13:1773–1774
37. Hadži-Jordanov S, Angerstein-Kozlowska H, Conway BE (1975) Surface oxidation and H deposition at ruthenium electrodes: Resolution of component processes in potential-sweep experiments. J Electroanal Chem Interfacial Electrochem 60:359–362
38. Hadži-Jordanov, S.; Angerstein-Kozlowska, H.; Vukovic, M.; Conway, B. E. Reversibility and Growth Behavior of Surface Oxide Films at Ruthenium Electrodes. J. Electrochem. Soc. 1978, 125, 1471.
39. Birss V, Myers R, Angerstein-Kozlowska H, Conway BE (1984) Electron microscopy study of formation of thick oxide films on Ir and Ru electrodes. J Electrochem Soc 131:1502
40. Hadzi-Jordanov S, Angerstein-Kozlowska H, Vukovic M, Conway BE (1977) The state of electrodeposited hydrogen at ruthenium electrodes. J Phys Chem 81:2271–2279
41. Vuković M, Angerstein-Kozlowska H, Conway BE (1982) Electrocatalytic activation of ruthenium electrodes for the Cl_2 and O_2 evolution reactions by anodic/cathodic cycling. J Appl Electrochem 12:193–204
42. Vuković M, Valla T, Milun M (1993) Electron spectroscopy characterization of an activated ruthenium electrode. J Electroanal Chem 356:81–91
43. Marijan D, Čukman D, Vuković M, Milun M (1995) Anodic stability of electrodeposited ruthenium: galvanostatic, thermogravimetric and X-ray photoelectron spectroscopy studies. J Mater Sci 30:3045–3049
44. Liu T, Pell WG, Conway BE (1997) Self-discharge and potential recovery phenomena at thermally and electrochemically prepared RuO_2 supercapacitor electrodes. Electrochim Acta 42:3541–3552
45. Blouin M, Guay D (1997) Activation of ruthenium oxide, iridium oxide, and mixed Ru[sub x]Ir[sub 1−x] oxide electrodes during cathodic polarization and hydrogen evolution. J Electrochem Soc 144:573
46. Mo Y, Antonio MR, Scherson DA (2000) In situ Ru K-edge X-Ray absorption fine structure studies of electroprecipitated ruthenium dioxide films with relevance to supercapacitor applications. J Phys Chem B 104:9777–9779
47. Horvat-Radosevic V, Kvastek K, Vukovic M, Cukman D (2000) Electrochemical properties of ruthenised electrodes in the oxide layer region. J Electroanal Chem 482:188–201

48. Hu C-C, Wang C-C (2002) Improving the utilization of ruthenium oxide within thick carbon–ruthenium oxide composites by annealing and anodizing for electrochemical supercapacitors. Electrochem Commun 4:554–559
49. Hu C-C, Chiang H-R, Wang C-C (2003) Electrochemical and structural investigations of oxide films anodically formed on ruthenium-plated titanium electrodes in sulfuric acid. J Solid State Electrochem 7:477–484
50. Hu C, Liu M, Chang K (2008) Anodic deposition of hydrous ruthenium oxide for supercapaciors: effects of the AcO^- concentration, plating temperature, and oxide loading. Electrochim Acta 53:2679–2687
51. Hu C, Liu M, Chang K (2007) Anodic deposition of hydrous ruthenium oxide for supercapacitors. J Power Sources 163:1126–1131
52. Park B, Lokhande CD, Park H, Jung K, Joo O (2004) Cathodic electrodeposition of RuO_2 thin films from $Ru(III)Cl_3$ solution. Mater Chem Phys 87:59–66
53. Wu H-M, Hsu P-F, Hung W-T (2009) Investigation of redox reaction of Ru on carbon nanotubes by pulse potential electrochemical deposition. Diam Relat Mater 18:337–340
54. Patake V, Lokhande C, Joo O (2009) Electrodeposited ruthenium oxide thin films for supercapacitor: effect of surface treatments. Appl Surf Sci 255:4192–4196
55. Zheng Y, Ding H, Zhang M (2008) Hydrous–ruthenium–oxide thin film electrodes prepared by cathodic electrodeposition for supercapacitors. Thin Solid Films 516:7381–7385
56. Ahn YR, Song MY, Jo SM, Park CR, Kim DY (2006) Electrochemical capacitors based on electrodeposited ruthenium oxide on nanofibre substrates. Nanotechnology 17:2865–2869
57. Zhitomirsky I, Gal-Or L (1997) Ruthenium oxide deposits prepared by cathodic electrosynthesis. Mater Lett 31:155–159
58. Sugimoto, W.; Makino, S.; Mukai, R.; Tatsumi, Y.; Katsutoshi; Fukuda; Takasu, Y.; Yamauchi, Y. Synthesis of Ordered Mesoporous Ruthenium by Lyotropic Liquid Crystals and Its Electrochemical Conversion to Mesoporous Ruthenium Oxide with High Surface Area. J. Power Sources 2012, in press.
59. Takasu Y, Murakami Y (2000) Design of oxide electrodes with large surface area. Electrochim Acta 45:4135–4141
60. Sugimoto W, Shibutani T, Murakami Y, Takasu Y (2002) Charge storage capabilities of rutile-type RuO[sub 2]-VO[sub 2] solid solution for electrochemical supercapacitors. Electrochem Solid-State Lett 5:A170
61. Yokoshima K, Shibutani T, Hirota M, Sugimoto W, Murakami Y, Takasu Y (2006) Electrochemical supercapacitor behavior of nanoparticulate rutile-type Ru1−xVxO2. J Power Sources 160:1480–1486
62. Jeong Y, Manthiram A (2000) Amorphous ruthenium-chromium oxides for electrochemical capacitors. Electrochem Solid-State Lett 3:205
63. Jeong YU, Manthiram A (2001) Amorphous tungsten oxide/ruthenium oxide composites for electrochemical capacitors. J Electrochem Soc 148:A189
64. Wang C-C, Hu C-C (2005) Electrochemical and textural characteristics of $(Ru\text{-}Sn)Ox \cdot nH_2O$ for supercapacitors. J Electrochem Soc 152:A370
65. Cao F, Prakash J (2001) Performance investigations of $Pb_2Ru_2O6.5$ oxide based pseudocapacitors. J Power Sources 92:40–44
66. Schenk J, Wilde PM, Abdelmula E, Axmann P, Garche J (2002) New materials for supercapacitors. J Power Sources 105:182–188
67. Park B, Lokhande CD, Park H, Jung K, Joo O (2004) Preparation of lead ruthenium oxide and its use in electrochemical capacitor. Mater Chem Phys 86:239–242
68. Lee Y, Oh J, Oh H, Kim H (2008) Novel method for the preparation of carbon supported nano-sized amorphous ruthenium oxides for supercapacitors. Electrochem Commun 10:1035–1037
69. Naoi K, Ishimoto S, Ogihara N, Nakagawa Y, Hatta S (2009) Encapsulation of nanodot ruthenium oxide into KB for electrochemical capacitors. J Electrochem Soc 156:A52–A59
70. Fang W, Cyyan O, Sun C, Wu C, Chen C, Chen K, Chen L, Huang J (2007) Arrayed CNx NT–RuO2 nanocomposites directly grown on Ti-buffered Si substrate for supercapacitor applications. Electrochem Commun 9:239–244
71. Kim I-H, Kim J-H, Kim K-B (2005) Electrochemical characterization of electrochemically prepared ruthenium oxide/carbon nanotube electrode for supercapacitor application. Electrochem Solid-State Lett 8:A369
72. Qin X, Durbach S, Wu GT (2004) Electrochemical characterization on $RuO_2 \bullet xH_2O$/carbon nanotubes composite electrodes for high energy density supercapacitors. Carbon 42:451–453
73. Fang W-C, Leu M-S, Chen K-H, Chen L-C (2008) Ultrafast charging-discharging capacitive property of RuO[sub 2] nanoparticles on carbon nanotubes using nitrogen incorporation. J Electrochem Soc 155:K15
74. Deng GH, Xiao X, Chen JH, Zeng XB, He DL, Kuang YF (2005) A new method to prepare RuO2•xH2O/carbon nanotube composite for electrochemical capacitors. Carbon 43:1566–1569
75. Arabale G, Wagh D, Kulkarni M, Mulla IS, Vernekar SP, Vijayamohanan K, Rao AM (2003) Enhanced supercapacitance of multiwalled carbon nanotubes functionalized with ruthenium oxide. Chem Phys Lett 376:207–213
76. Kim Y-T, Tadai K, Mitani T (2005) Highly dispersed ruthenium oxide nanoparticles on carboxylated carbon nanotubes for supercapacitor electrode materials. J Mater Chem 15:4914

77. Lee J-K, Pathan HM, Jung K-D, Joo O-S (2006) Electrochemical capacitance of nanocomposite films formed by loading carbon nanotubes with ruthenium oxide. J Power Sources 159:1527–1531
78. Yuan C, Chen L, Gao B, Su L, Zhang X (2009) Synthesis and utilization of RuO2•xH2O nanodots well dispersed on poly(sodium 4-styrene sulfonate functionalized multi-walled carbon nanotubes for supercapacitors. J Mater Chem 19:246
79. Kim I-H, Kim J-H, Lee Y-H, Kim K-B (2005) Synthesis and characterization of electrochemically prepared ruthenium oxide on carbon nanotube film substrate for supercapacitor applications. J Electrochem Soc 152:A2170
80. Reddy ALM, Ramaprabhu S (2007) Nanocrystalline metal oxides dispersed multiwalled carbon nanotubes as supercapacitor electrodes. J Phys Chem C 111:7727–7734
81. Kim JD, Kang BS, Noh TW, Yoon J-G, Baik SI, Kim Y-W (2005) Controlling the nanostructure of RuO_2/carbon nanotube composites by Gas annealing. J Electrochem Soc 152:D23
82. Wu Z-S, Wang D-W, Ren W, Zhao J, Zhou G, Li F, Cheng H-M (2010) Anchoring hydrous RuO_2 on graphene sheets for high-performance electrochemical capacitors. Adv Funct Mater 20:3595–3602
83. Wang, H.; Liang, Y.; Mirfakhrai, T.; Chen, Z.; Casalongue, H. S.; Dai, H. Advanced asymmetrical supercapacitors based on graphene hybrid materials. Nano Research 2011, 3.
84. Mishra AK, Ramaprabhu S (2011) Functionalized graphene-based nanocomposites for supercapacitor application. J Phys Chem C 115:14006–14013
85. Zhang J, Jiang J, Li H, Zhao XS (2011) A high-performance asymmetric supercapacitor fabricated with graphene-based electrodes. Energy Environ Sci 4:4009
86. Chen Y, Zhang X, Zhang D, Ma Y (2012) One-pot hydrothermal synthesis of ruthenium oxide nanodots on reduced graphene oxide sheets for supercapacitors. J Alloys Comp 511:251–256
87. Rakhi RB, Chen W, Cha D, Alshareef HN (2011) High performance supercapacitors using metal oxide anchored graphene nanosheet electrodes. J Mater Chem 21:16197
88. Sato Y, Yomogida K, Nanaumi T, Kobayakawa K, Ohsawa Y, Kawai M (1999) Electrochemical behavior of activated-carbon capacitor materials loaded with ruthenium oxide. Electrochem Solid-State Lett 3:113
89. Nanaumi T, Ohsawa Y, Kobayakawa K, Sato Y (2002) High energy electrochemical capacitor materials prepared by loading ruthenium oxide on activated carbon. Electrochemistry 70:681
90. Sugimoto W, Iwata H, Yasunaga Y, Murakami Y, Takasu Y (2003) Preparation of ruthenic acid nanosheets and utilization of its interlayer surface for electrochemical energy storage. Angew Chem Int Ed Engl 42:4092–4096
91. Fukuda K, Saida T, Sato J, Yonezawa M, Takasu Y, Sugimoto W (2010) Synthesis of nanosheet crystallites of ruthenate with an alpha-$NaFeO_2$-related structure and its electrochemical supercapacitor property. Inorg Chem 49:4391–4393
92. Ardizzone S, Fregonara G, Trasatti S (1990) "Inner" and "outer" active surface of RuO_2 electrodes. Electrochim Acta 35:263–267
93. Rishpon J, Gottesfeld S (1960) Resolution of fast and slow charging processes in ruthenium oxide films: an AC impedance and optical investigation. J Electrochem Soc 1984:131
94. Foelske A, Barbieri O, Hahn M, Kötz R (2006) An X-Ray photoelectron spectroscopy study of hydrous ruthenium oxide powders with various water contents for supercapacitors. Electrochem Solid-State Lett 9: A268
95. Rochefort D, Dabo P, Guay D, Sherwood P (2003) XPS investigations of thermally prepared RuO_2 electrodes in reductive conditions. Electrochim Acta 48:4245–4252
96. Chabanier C, Irissou E, Guay D, Pelletier JF, Sutton M, Lurio LB (2002) Hydrogen absorption in thermally prepared RuO_2 electrode. Electrochem Solid-State Lett 5:E40
97. Chabanier C, Guay D (2004) Activation and hydrogen absorption in thermally prepared RuO_2 and IrO_2. J Electroanal Chem 570:13–27
98. Barbieri O, Hahn M, Foelske A, Kotz R (2006) Effect of electronic resistance and water content on the performance of RuO_2 for supercapacitors. J Electrochem Soc 153:A2049
99. Stefan IC, Mo Y, Antonio MR, Scherson DA (2002) In situ Ru L II and L III edge X-ray absorption near edge structure of electrodeposited ruthenium dioxide films. J Phys Chem B 106:12373–12375
100. Mo Y, Bae IT, Sarangapani S, Scherson DA (2003) In situ Ru K-edge X-ray absorption spectroscopy of a high-area ruthenium dioxide electrode in a Nafion-based supercapacitor environment. J Solid State Electrochem 7:572–575
101. Mo Y, Cai W-B, Dong J, Carey PR, Scherson DA (2001) In situ surface enhanced Raman scattering of ruthenium dioxide films in acid electrolytes. Electrochem Solid-State Lett 4:E37